DAQ Software Contributions, Absolute Scale Energy Calibration and Background Evaluation for the NOvA Experiment at Fermilab

A Dissertation Presented for the

Doctor of Philosophy

Degree

The University of Tennessee, Knoxville

Eric Flumerfelt

August 2015

Abstract

The NOvA (NuMI Off-axis ν_e [nu_e] Appearance) Experiment is a long-baseline accelerator neutrino experiment currently in its second year of operations. NOvA uses the Neutrinos from the Main Injector (NuMI) beam at Fermilab, and there are two main off-axis detectors: a Near Detector at Fermilab and a Far Detector 810 km away at Ash River, MN. The work reported herein is in support of the NOvA Experiment, through contributions to the development of data acquisition software, providing an accurate, absolute-scale energy calibration for electromagnetic showers in NOvA detector elements, crucial to the primary electron neutrino search, and through an initial evaluation of the cosmic background rate in the NOvA Far Detector, which is situated on the surface without significant overburden. Additional support work for the NOvA Experiment is also detailed, including DAQ Server Administration duties and a study of NOvA's sensitivity to neutrino oscillations into a "sterile" state.

Table of Contents

1 Introduction **1**

2 Theory **5**

2.1 Neutrino History 5

2.2 Neutrino Interactions with Matter 6

2.2.1 Charged Current Quasi-Elastic Events 6

2.2.2 Neutral Current Elastic Events 7

2.2.3 Single Pion Production 7

2.2.4 Deep Inelastic Scattering 8

2.3 Important Neutrino Experiments 9

2.3.1 Discovery of the Neutrino 9

2.3.2 The Solar Anomaly 11

2.3.3 Resolution of the Solar Anomaly: Super-K and SNO 11

2.3.4 Measuring the Oscillation Parameters 14

2.4 Oscillation Parameters 17

2.5 CP Violation 18

2.6 Mass Hierarchy 20

2.7 Current Knowledge of Neutrino Mixing Parameters 20

3 NOνA Experiment Overview **23**

3.1 Introduction 23

3.2 NOνA Physics Goals 24

3.2.1 Theta 13 Measurement . . . 25
3.2.2 Mass Hierarchy and CP Violation . . . 29
3.3 NOνA Detector Construction . . . 29
3.3.1 Near Detector On Surface . . . 31
3.3.2 Far Detector . . . 32
3.3.3 Near Detector . . . 32
3.4 The NuMI Beamline . . . 33
3.4.1 Horn Current . . . 35
3.4.2 Energy Spectra . . . 36
3.5 Data-Driven Triggers . . . 36
3.5.1 Supernovae . . . 38
3.5.2 Monopoles . . . 38
3.5.3 Other Physics . . . 38
3.6 NOνASoft: Data and Monte Carlo Analysis . . . 39
3.6.1 Production . . . 40
3.6.2 Reconstruction . . . 41
3.6.3 Particle Identification . . . 41
3.6.4 Common Analysis Framework (CAF) . . . 42

4 NOνA DAQ software 43

4.1 Introduction . . . 43
4.2 DAQ Software Overview . . . 44
4.2.1 Data Handling . . . 44
4.2.2 Triggering and Timing . . . 45
4.2.3 Run Control and Configuration . . . 47
4.2.4 Message Passing, Logging and Analysis . . . 47
4.2.5 Monitoring . . . 50
4.3 Pedestal Data Runner . . . 50
4.4 NOνA DAQ software Computing Clusters . . . 55

4.4.1 Near Detector On Surface Computing Cluster 55
4.4.2 Far Detector Computing Cluster 56
4.4.3 Near Detector Computing Cluster 58
4.5 Load Shedding and Temperature Monitoring 59
4.5.1 Overview 59
4.5.2 Temperature Monitoring 59
4.5.3 Load Shed Procedure 60
4.6 Other DAQ Expert Experience 61
4.6.1 DAQ Software Management 61

5 Compton Spectrometer Experiment **63**
5.1 Introduction 63
5.2 Theory 64
5.3 Compton Measurement 65
5.3.1 Overview 65
5.3.2 Upgrades 67
5.3.3 Compton DAQ Hardware Logic 67
5.3.4 LabVIEW DAQ 68
5.3.5 Data Files and Analysis 70
5.4 Geant4 Model 71
5.4.1 Implementation Details for Cherenkov Simulation in the Compton Spectrometer Geant4 Model 72
5.4.2 Determining Ge Crystal Dimensions for Geant4 Model 73
5.5 Results and Analysis 73

6 Background Evaluation **81**
6.1 Introduction 81
6.2 Analysis Methodology 82
6.3 Results 83
6.4 Other Backgrounds 85

7 Sterile Neutrinos in the NOνA Near Detector (Study) 92

7.1 Introduction and Sterile Neutrino Hypothesis 92

7.2 NOνA Sensitivity: Disappearance Channel 94

7.3 NOνA Sensitivity: Spectral Distortion Channel 94

7.4 Combined Measurements 97

7.5 NOνA versus Reactor Experiments 97

7.6 NOνA versus Accelerator Experiments 98

7.7 Conclusion 100

8 Summary and Conclusion 101

8.1 DAQ Service Work 101

8.2 Scintillator Absolute Calibration 101

8.3 Background Evaluation 102

8.4 Conclusion 102

Bibliography 103

Vita 104

List of Tables

2.1 Measured central values for oscillation parameters [24] 21

6.1 Overburdens of various neutrino detectors 82
6.2 Summay Results of Background Analysis 84
6.3 Background Analysis Results: Daily Event Prediction 84

List of Figures

1.1 Diagram of NOνA baseline relative to MINOS 2
1.2 The NOνA Detectors 3

2.1 Feynman Diagrams for Single Pion Production 8
2.2 Muon Neutrino Cross Sections 9
2.3 The Cowan-Reines "Project Poltergeist" Detector at Savannah River 10
2.4 The Homestake Detector Vessel 12
2.5 Interior of the Super Kamiokande Detector [17] 13
2.6 The SNO Detector [3] 13
2.7 The KamLAND Detector [1] 15
2.8 The MINOS Far Detector [23] 16
2.9 Second-Generation Reactor Experiments 17
2.10 ν_μ Oscillation Probability over NOνA L/E Space 19
2.11 Graphical representation of neutrino hierarchy 21

3.1 NOνA Collaboration at Argonne National Laboratory, July 2013 . . . 24
3.2 NOνA Bi-probability Sensitivity Plot 26
3.3 NOνA Bi-Probability Sensitivity Plot – Effect of Energy Binning . . . 27
3.4 NOνA Bi-Probability Sensitivity Plot – Effect of ϑ_{13} 28
3.5 NOνA Bi-Probability Plot – Measurement Example 30
3.6 NOνA Construction and Assembly Process 31
3.7 View of the top of the Far Detector 33

3.8 View of the top of the Near Detector 34
3.9 The NuMI Beamline 35
3.10 NuMI neutrino energy distributions versus off-axis location 37
3.11 Flow diagram of the NOνA Production and Reconstruction chain . . 40

4.1 Diagram of the DAQ Software System 44
4.2 The Trigger Scalars 46
4.3 The TDU Control GUI 46
4.4 The Run Control Client 48
4.5 The DAQ Application Manager 49
4.6 The Message Viewer 51
4.7 The Message Analyzer 52
4.8 NOνA Event Displays 52
4.9 Online Monitor 53
4.10 The DCS GUI 53
4.11 The Pedestal Data Runner GUI 54
4.12 Ganglia view of Far Detector Managers 55
4.13 Photograph of the NDOS DAQ Cluster 57
4.14 Temperature Sensor Data at the Far Detector Computing Cluster . . 60
4.15 Flowchart of the Loadshed Script 61

5.1 Effect of quenching in KamLAND scintillator 66
5.2 Schematic diagram of the Compton Spectrometer experiment 66
5.3 The Compton Spectrometer's hardware DAQ logic 67
5.4 Oscilloscope traces showing the relative timing of the Compton DAQ system 69
5.5 Compton LabVIEW DAQ Software Front Panel 69
5.6 Geant4 Model of Compton Spectrometer Experiment 72
5.7 Compton Coincidence Detector Maps 74
5.8 Results from the integration run of the Compton Spectrometer 75

5.9 QDC Spectrum, untriggered calibration run 76
5.10 PADC Spectrum, untriggered calibration run, 0 degree angle 77
5.11 Compton spectrometer at 40 Degrees 78
5.12 Compton spectrometer at 100 degrees 79
5.13 Result of the analysis of the Compton spectrometer 80

6.1 Event Display, Run 16937, Event 85742 85
6.2 Event Display, Run 16925, Event 20032 86
6.3 Event Display, Run 16500, Event 153920 86
6.4 Event Display, Run 16928, Event 127864 87
6.5 Event Display, Run 16940, Event 1433 87
6.6 Event Display, Run 16677, Event 254622 88
6.7 Event Display, Run 16682, Event 254529 88
6.8 Event Display, Run 16497, Event 792 89
6.9 Event Display, Run 16695, Event 207694 89
6.10 Resulting ν_τ Contamination in the NOνA FD 91

7.1 Sterile Neutrino Oscillation Example 93
7.2 Near detector spectrum prediction with sterile neutrino oscillation . . 95
7.3 NDOS Spectrum Prediction with Sterile Neutrino Oscillation 96
7.4 Sterile Neutrino Study Result 98
7.5 Sterile Neutrino Study Result 99

Abbreviations Used

ν_μ muon neutrino. 6, 14, 16, 19, 23–25, 35, 39–41, 82–84, 88–91, 98, 100

ϑ_{13} theta 13. 1, 17, 18, 21, 22, 24, 25, 27, 29

ϑ_{23} theta 23. 14, 25–28, 30

δ_{CP} the Dirac CP-Violating Phase. 1, 18, 21, 24, 25, 27, 29

ν_e electron neutrino. 1, 4, 11, 14, 20, 23–25, 39–42, 82–88, 90, 98, 102

ADC Analog-to-Digital Converter. 41, 44, 47, 52, 67–70

APD Avalanche Photodiode. 31, 32, 44, 50, 64

ARCC Ash River Computing Center. 43, 55, 60

BNB Booster Neutrino Beam. 98

BNEVB Buffer Node Event Builder. 45, 47, 49

CAF Common Analysis Framework. 39, 40, 42, 82

CCQE Charged-Current Quasi-Elastic. 6, 7

CPU Central Processing Unit. 59

DAQ Data Acquisition. 4, 29, 32, 33, 38, 43–45, 47, 49, 50, 53, 56–58, 60, 61, 67, 68, 70, 100–102

DCM Data Concentrator Module. 29, 31, 32, 34, 44, 45, 47, 49, 50, 53, 54, 56, 62, 88

DCS Detector Control System. 50, 53, 56

DDS Data Distribution Service. 47, 49

DDT Data-Driven Triggers. 24, 38, 39, 43, 45, 46, 60, 101

DHCP Dynamic Host Configuration Protocol, used to assign IP Addresses to hosts based on their network hardware. 56

DIS Deep Inelastic Scattering. 8, 9

DSO Digital Scanning Oscilloscope. 47, 50

EM electromagnetic. 4–7

FD Far Detector. 1–4, 23, 32, 33, 40, 41, 50, 55–59, 61, 81, 82, 90, 91, 102

FDCC Far Detector Computing Cluster. 56, 58–60

FEB Front-End Board. 31, 32, 44, 45, 47, 50, 53

FEF/SSS Fermilab Experiment Facilities, Scientific Server Support. 56, 58

Fermilab Fermi National Accelerator Laboratory. 1, 16, 23, 36, 55, 58, 100–102

FHC Forward Horn Current. 35, 36

GPS Global Positioning System. 45

GUI Graphical User Interface. 4, 69

HPGe High-Purity Germanium. 67

IPMI Intelligent Platform Management Interface. 58, 60

LEM Library Event Matcher. 40–42

LS Liquid Scintillator. 2, 4, 63, 65, 100, 101

MC Monte Carlo Simulation. 39, 40, 84

MIP Minimum Ionizing Particle. 63

ND Near Detector. 1, 3, 4, 23, 31–34, 39, 43, 55, 57, 58, 61, 85, 90, 94, 97, 101

NDOS Near Detector On Surface. 2, 3, 31–33, 55–58, 61, 85, 94, 96, 100

NFS Network File System. 49, 56

NIS Network Information Service, used to distribute information about users, groups, and hostname/IP mappings. 56

NOνA NuMI Off-Axis ν_e Appearance. 1–4, 6–8, 18, 19, 21, 23–33, 36–40, 43, 44, 46, 52, 56, 58, 59, 63–65, 71, 74, 80–85, 91, 94, 95, 97–102

NOνADAQ NOνA DAQ software. 43, 47, 50, 55, 56, 58, 101

NOνASoft NOνA Offline software. 39–42, 50, 82

NuMI Neutrinos from the Main Injector. 1, 16, 23, 24, 33, 35, 37, 83–85, 94

OnMon Online Monitor. 50, 53

OSG Open Science Grid. 40

overburden The shielding material placed on top of a particle physics detector to reduce the flux of cosmic-ray particles through the detector. 2, 11, 82

PADC Peak-Sensing ADC. 67, 68, 70, 75, 78

PDG Particle Data Group. 21

PDR Pedestal Data Runner. 50, 54

PID Particle Identification. 2, 39–41, 83, 85

PMNS Pontecorvo-Maki-Nakagawa-Sakata. 18–20

PMT Photo-Multiplier Tube. 9, 11, 14, 16, 64, 70

POT Protons On Target. 35

QDC Charge-sensitive ADC. 68, 70, 74, 75, 78, 79

RHC Reverse Horn Current. 36

SBN Short Baseline Neutrino. 98, 100, 102

SNEWS Supernova Early Warning System. 32, 38, 43

SNMP Simple Network Management Protocol. 59

SNO Sudbury Neutrino Observatory. 13, 14, 82

SNR signal to noise ratio. 83, 84

SOL Serial Over LAN. 58

SSH Secure Shell. 60

Super-K Super Kamiokande. 11, 13, 14, 16

TDR Technical Design Report, [26]. 38

TDU Timing Distribution Unit. 56, 62

TFTP Trivial File Transfer Protocol. 56

UT University of Tennessee. 39, 67, 71, 90, 101

VNC Virtual Network Computing. 56

WLS wavelength-shifting. 63, 64, 71

Chapter 1

Introduction

The NuMI Off-Axis ν_e Appearance (NOνA) Experiment at Fermi National Accelerator Laboratory (Fermilab) is the second-generation of accelerator neutrino experiments at the Neutrinos from the Main Injector (NuMI) beam. The NuMI beam provides a neutrino spectrum centered about 2 GeV at NOνA's 14 mrad off-axis angle. NOνA aims to explore the intensity frontier in neutrino interactions and make a highly-accurate measurement of several neutrino oscillation parameters. It is uniquely sensitive to the mass hierarchy of neutrinos, and the Dirac CP-Violating Phase (δ_{CP}), though the measurement of these two quantities share the same phase space and may not be unambiguously resolved by NOνA. What makes the NOνA Experiment unique is its long baseline of 810 km and the well-formed neutrino spectrum from the NuMI beam caused by NOνA's off-axis location (Figures 1.1, 3.10). This allows for a detailed search for electron neutrino (ν_e) appearance in both the "neutrino" and "anti-neutrino" modes of the NuMI beam. NOνA will also be able to make a reactor-independent, high-precision measurement of the mixing angle theta 13 (ϑ_{13}) (See Section 2.4). The full NOνA run will consist of three years in "neutrino" mode followed by three years in "anti-neutrino" mode, with the 14 kT Far Detector (FD) (Figure 1.2b) and the approximately 300 T Near Detector (ND) (Figure 1.2a). In addition to these

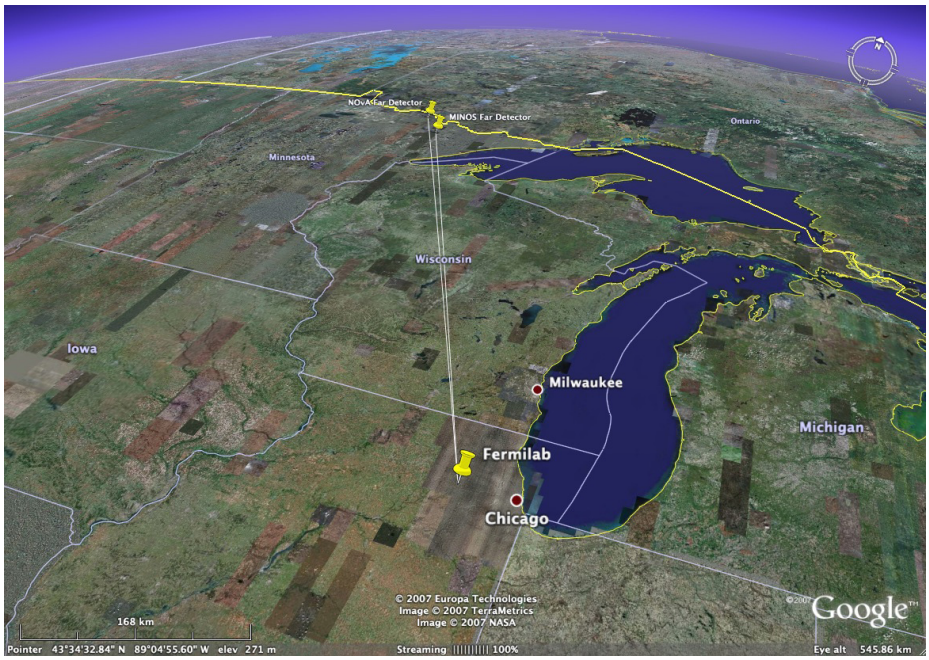

Figure 1.1: Google Earth view of the NOνA baseline, including the on-axis MINOS Far Detector location at Soudan, MN.

two detectors is the full-scale integration prototype, the Near Detector On Surface (NDOS) (Figure 1.2c).

For my thesis, I have chosen two topics which I believe to be crucial to the success of the NOνA Experiment: the background neutrino signal observed in the FD, and an absolute-scale energy calibration for the NOνA Liquid Scintillator (LS). The background signal was measured by running the same Particle Identification (PID) algorithms used in NOνA's neutrino search over the random "cosmic" trigger files. The FD sits under one of the smallest overburdens ever attempted for a neutrino experiment, raising the chance for cosmic-induced "accidental" background signals. NOνA uses the beam spill timestamps to define neutrino triggers that are only 50 μs wide, reducing this cosmic background. However, it is still possible that a cosmic event could occur during this time which passes automatic reconstruction cuts. The background evaluation I performed produced an expected rate for such events by finding the number of events that pass selection criteria in the cosmic random trigger

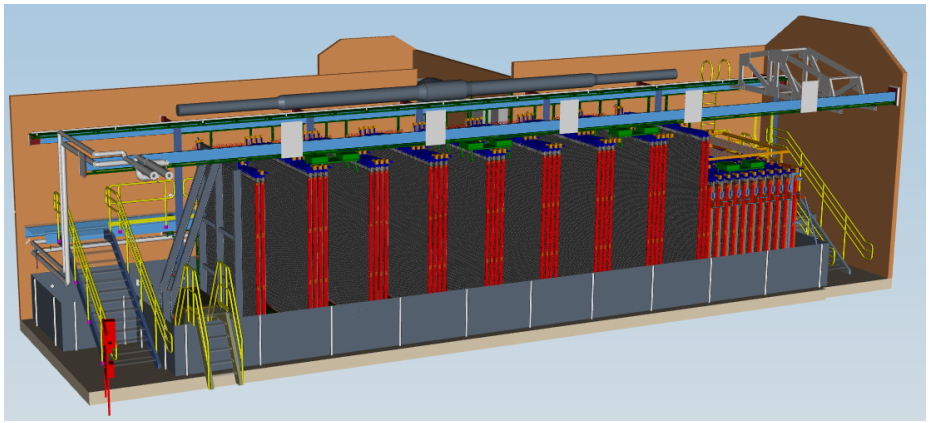

(a) The Near Detector

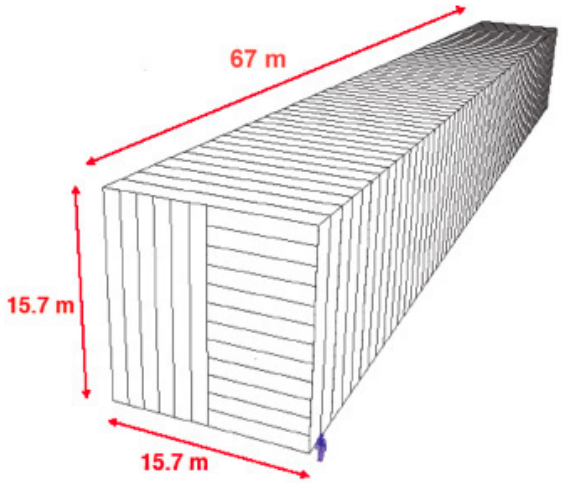

(b) The Far Detector

(c) The NDOS

Figure 1.2: The NOνA Detectors. Schematic diagrams are used for the Far Detector and the Near Detector because they are installed in confined areas where photographs of the entire detector are impossible. (See Figure 3.7)

files from the first analysis runs, then scaling this result to the actual live-time of the detector.

In addition to this physics analysis, I have completed a Compton Spectrometer experiment to measure the nonlinear response of the NOνA LS. The NOνA detectors are calibrated in-situ using the cosmic muon signal collected through the use of the random, "cosmic" triggers. The nonlinearity of the scintillator's response, however, causes an over-estimation of the energy of electromagnetic (EM) showers which is impossible to completely account for using only detector data. This effect is most notable at high values of $\frac{dE}{dx}$, as encountered in the tail of an EM shower. As NOνA's primary goal is the measurement and reconstruction of ν_e signal, the energy estimation of the EM shower is of paramount importance to the experiment, and the size and location of the detectors, especially the FD, make more direct calibration measurements impossible or impractical.

I have also carried out several supporting tasks for the NOνA Experiment, including software development for both "offline" physics analysis and for "online" data acquisition. I was heavily involved in the Data Acquisition (DAQ) group for NOνA, serving as a DAQ expert to address issues with the DAQ that cropped up, making contributions to the DAQ Graphical User Interfaces (GUIs), and developing patches for several major components of the DAQ system. Additionally, I was responsible for setting up the DAQ for the ND, enabling it to be read-out during its commissioning phase. I also carried out a sterile neutrino sensitivity study for the ND. As a member of the Production group, I was responsible for submitting NOνA Monte Carlo simulations to the Open Science Grid for faster processing.

Chapter 2

Theory

2.1 Neutrino History

The neutrino was first theorized in 1930 by Pauli as a way for beta decays to conserve energy, linear momentum and angular momentum [11]. He called his particle the "neutron", and believed it to be a constituent of the nucleus, but possessing very little mass. (The other leading theory of the time was that these quantities were only conserved on a statistical basis.) With Chadwick's discovery of the heavy neutron in 1932, the name "neutrino" was proposed by Fermi for the particle that participates in beta decay. Neutrinos were first experimentally measured in 1956 by Cowan and Reines (Section 2.3.1) using the inverse beta decay process and reactor anti-neutrinos. Neutrinos have very low mass (less than 2 eV ([24])), the exact value of which is still unknown, and is the subject of ongoing high-precision experiments. Due to this extremely low mass and their lack of electromagnetic (EM) or strong-force interactions, neutrinos are extremely penetrating particles with very low cross-sections for any given detection process.

2.2 Neutrino Interactions with Matter

Neutrino interactions are broadly categorized as "Charged Current" (where a charged lepton is present in the final state), or "Neutral Current" (where a neutrino is present in the final state) [16]. Neutral current events, including neutrino forward scattering, do not produce a lepton and therefore do not provide any leptonic flavor identification (and are consequently ignored in neutrino flavor-oscillation experiments). Neutral current events may, however, create secondary leptons, mesons, or other particles, and therefore become a significant background in accelerator experiments like NuMI Off-Axis ν_e Appearance (NOνA), because they occur in-time with expected signal events. Vertex reconstruction is necessary to determine if a lepton is a part of the primary event. This is more important for muon neutrino (ν_μ) events, as muons are commonly the product of the decay of the mesons produced in neutral current events.

2.2.1 Charged Current Quasi-Elastic Events

Charged current events at NOνA's energy usually take the form of a quasi-elastic reaction, equation (2.1).

$$\nu_l + \mathrm{n} \rightarrow \mathrm{p} + l^- \qquad\qquad \bar{\nu}_l + \mathrm{p} \rightarrow \mathrm{n} + l^+ \tag{2.1}$$

NOνA can reconstruct both the hadronic fragment and the lepton from a Charged-Current Quasi-Elastic (CCQE) interaction. (Unlike lower-energy reverse-beta processes, quasi-elastic reactions can result in multiple hadrons in the final state. [16]) Because of the high segmentation of the detector and the low-Z materials used in its construction, NOνA has very good separation between electrons and muons, and between EM showers caused by a recoil electron and those caused by neutral-current events such as π^0 photon pair production (See 2.2.3).

2.2.2 Neutral Current Elastic Events

As in the CCQE events described in Section 2.2.1, Neutral Current events may take an elastic form, sometimes called "neutrino forward scattering", due to the typical momentum profile of the event (equation (2.2)). These events are characterized by the neutrino scattering off of an entire nucleon, and are more common at lower energies where the neutrino cannot resolve the components of the nucleon.

$$\nu_l + \mathrm{N} \rightarrow \nu_l + \mathrm{N} \qquad\qquad \bar{\nu}_l + \mathrm{N} \rightarrow \bar{\nu}_l + \mathrm{N} \tag{2.2}$$

2.2.3 Single Pion Production

In single pion production, the neutrino excites the nucleon with which it interacts, causing it to decay back to a ground state and produce a π^0 or $\pi^{\pm}$. These interactions may be either charged-current or neutral-current, following equations (2.1) or (2.2), with the addition of a pion in the final state. (Charged-current events where the nucleon does not change its identity and neutral current events where it does are additionally possible through the extra degree of freedom granted by the charge of the resultant pion.) Probably the most significant potential background to NOνA is π^0 neutral current events, as the decay photons may appear to be the hadron-and-EM shower from a CCQE event.

In addition to these "resonant" processes, "coherent" pion production may occur. In these cases, the neutrino scatters off of the entire nucleus, and the energy to create a pion comes from the neutrino (very little energy is transferred to the nucleus). These reactions take the forms given in equation (2.3) for charged current and equation (2.4) for neutral current.

$$\nu_l + \mathrm{A} \rightarrow l^- + \mathrm{A} + \pi^+ \qquad\qquad \bar{\nu}_l + \mathrm{A} \rightarrow l^+ + \mathrm{A} + \pi^- \tag{2.3}$$

$$\nu_l + \mathrm{A} \rightarrow \nu_l + \mathrm{A} + \pi^0 \qquad\qquad \bar{\nu}_l + \mathrm{A} \rightarrow \bar{\nu}_l + A + \pi^0 \tag{2.4}$$

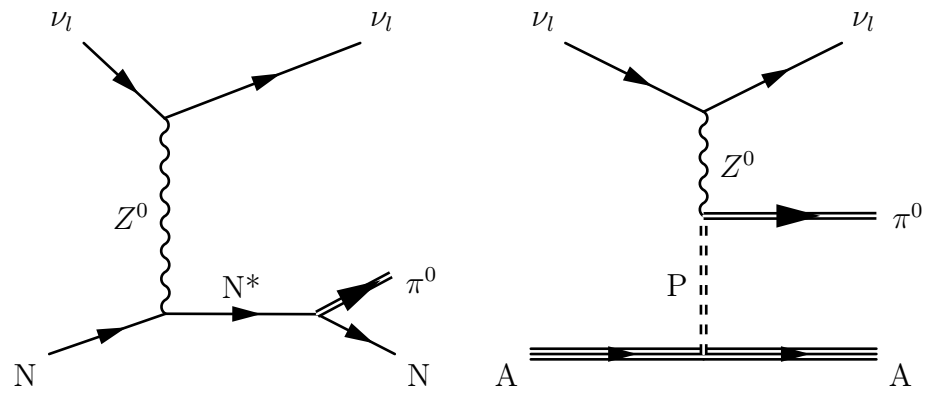

(a) Feynman diagram of a resonant single-pion event

(b) Feynman diagram of a coherent single-pion event

Figure 2.1: Feynman Diagrams for Single Pion Production

The difference between "resonant" pion production and "coherent" pion production is best expressed through Feynman diagrams. Figure 2.1a shows a resonant event, while Figure 2.1b shows a coherent event. The difference is clearly visible: in a resonant event, the pion is created while the nucleon returns to its ground state, while in a coherent event, a pion is created during the nucleus-neutrino interaction. What this means for a particle detector is that "resonant" events are momentum-independent from the neutrino, while "coherent" pions will be forward-scattered in the neutrino's direction.

2.2.4 Deep Inelastic Scattering

In Deep Inelastic Scattering (DIS), the neutrino has sufficient energy to resolve the components of a nucleon and scatter off of a quark. These reactions are both charged current and neutral current, leaving hadronic fragments and a lepton. DIS events are highly suppressed at NOνA's energy level of 2 GeV (Figure 2.2), and when they do occur, their topology is similar to the single-pion production cases already discussed.

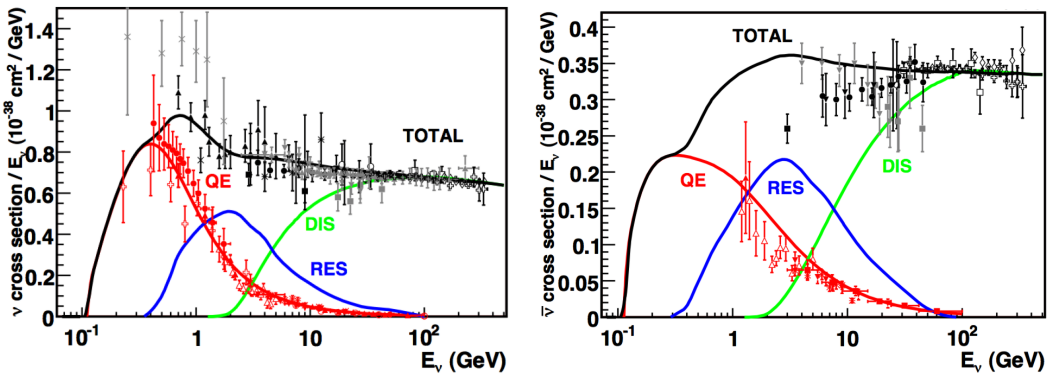

(a) Muon Neutrinos on Target **(b)** Muon Antineutrinos on Target

Figure 2.2: Existing muon neutrino charged-current cross section measurements [16] as a function of neutrino energy. The contributing processes in this energy region include quasi-elastic (QE) scattering, resonance production (RES), and DIS. The error bars in the intermediate energy range reflect the uncertainties in these cross sections (typically 10-40%, depending on the channel). Figure from [18].

2.3 Important Neutrino Experiments

Beginning with the experimental observation of the neutrino by Cowan and Reines (Section 2.3.1), neutrino experiments have been among the largest and most technologically-advanced detectors in the world. The following experiments have been instrumental in developing not only the theory of neutrino oscillations, but the technology and analysis techniques used by neutrino experiments today.

2.3.1 Discovery of the Neutrino

Cowan and Reines built a large liquid-scintillator counter at the Savannah River nuclear power plant in South Carolina [7]. Their design used two Gd-doped water tanks sandwiched between three 1400 L tanks of liquid scintillator, each with 110 Photo-Multiplier Tubes (PMTs) (Figure 2.3). They then required a prompt/ delayed coincidence signal in two adjacent detectors in order to discriminate against cosmic background events. They measured an excess of approximately one event per hour while the reactor was operating, with respect to reactor-off data. This result

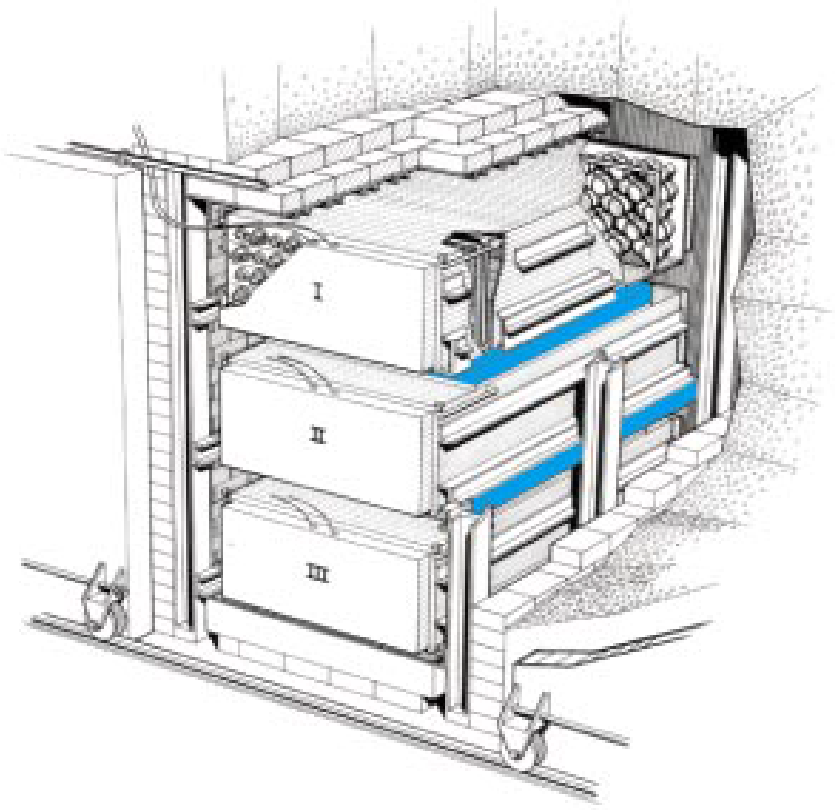

Figure 2.3: The Cowan-Reines "Project Poltergeist" Detector at Savannah River [7]

also provided the first experimental measurement of the inverse beta decay (electron neutrino (ν_e) charged-current) cross-section.

2.3.2 The Solar Anomaly

The Homestake solar neutrino detector [13] was designed to measure the flux of neutrinos from the Sun [12]. The motivation for this experiment was to confirm the solar nuclear fusion hypothesis by creating the first "telescope" which could probe the interior of the Sun. Their detector was buried 1478 m underground (compared to Cowan and Reines who only had a 10 m overburden). The Homestake experiment measured electron neutrinos through the reaction given in Equation 2.5.

$$\nu_e \ + \ {}^{37}\mathrm{Cl} \ \rightarrow \ {}^{37}\mathrm{Ar} \ + \ e^- \tag{2.5}$$

Their detector consisted of a single large vessel filled with 615 T of C_2Cl_4 and 1.5 atm pressurized helium gas (Figure 2.4). The argon produced in the inverse beta decay reaction (Equation 2.5) is removed by purging the liquid with helium and then removing the argon from the helium gas stream. The recovered argon gas was then placed in a proportional counter in order to measure the mass fraction of ^{37}Ar atoms present in the sample. The first results from this experiment were published in 1976; they only observed roughly $\frac{1}{3}$ the expected neutrino flux (The so-called "solar neutrino anomaly"). The solar anomaly called into question the methodology of Homestake, and then when independent confirmation was achieved, the Solar Model itself.

2.3.3 Resolution of the Solar Anomaly: Super-K and SNO

The Homestake experiment presented a puzzle to theorists that would take over 20 years to resolve. Super Kamiokande (Super-K) is a 50 kT water Cherenkov detector (Figure 2.5), with (at the time of their initial oscillation results) 11,146 PMTs in a 22.5 kT fiducial volume [17]. The large PMT coverage of Super-K allows for particle

Figure 2.4: The Homestake Detector Vessel [13]

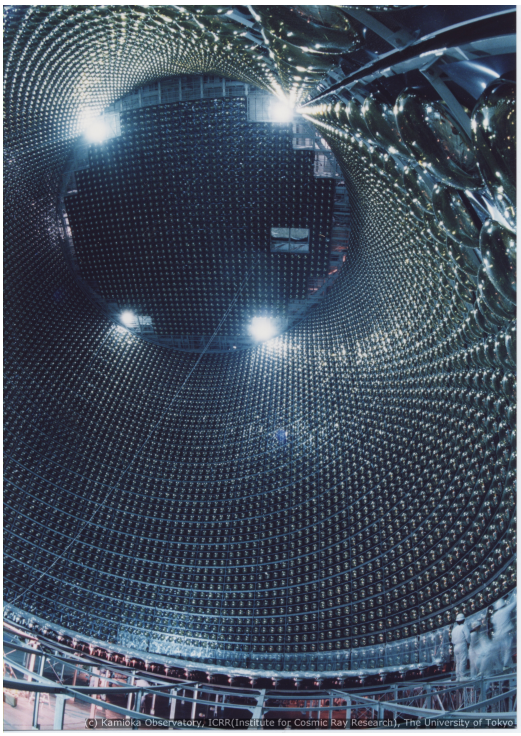

Figure 2.5: Interior of the Super Kamiokande Detector [17]

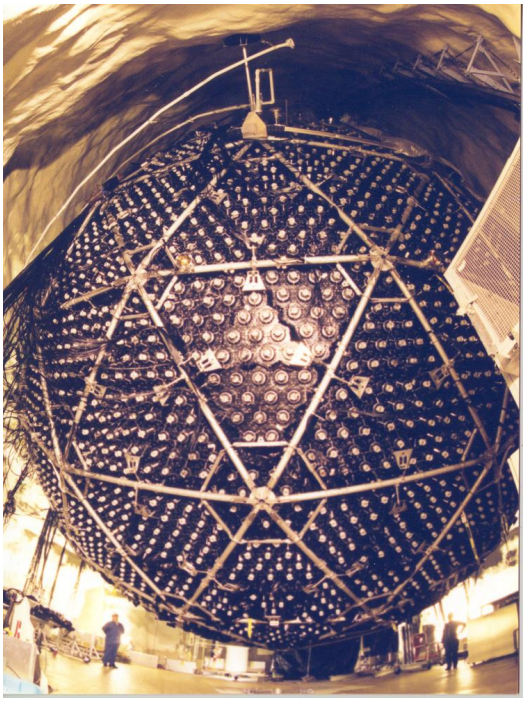

Figure 2.6: The SNO Detector [3]

identification by characterizing the outline of a Cherenkov ring on the detector's PMT surface as "fuzzy" or not. A "fuzzy" ring is an electron event, as the electromagnetic shower from an electron-type event produces many rings stacked on top of each other, each slightly offset from the track center by a random amount. On the other hand, a muon-type event produces only a single sharply-defined ring, as there are no secondary particles. Super-K observed a large variation on μ-type events based on zenith angle, with no such dependence observed in e-type events. This led to the conclusion that atmospheric neutrinos oscillate from ν_μ to tau neutrino (ν_τ) (ν_μ disappearance), with maximal mixing angle theta 23 (ϑ_{23}). This was the first direct observation of neutrino oscillation, opening the way for an oscillation solution to the Solar Anomaly, 22 years after it was first observed.

The Sudbury Neutrino Observatory (SNO) set out to measure the integrated solar neutrino flux (though neutral-current events), with identification of ν_e events, and therefore prove that neutrino oscillation caused the solar neutrino anomaly [3]. Their detector consisted of a large spherical vessel filled with 1000 T of heavy water (D_2O) and read out by 9456 PMTs (Figure 2.6). SNO observed a total solar neutrino flux that was in very good agreement with solar models, but they also measured a ν_e flux consistent with previous experiments. They concluded that solar neutrinos oscillate as they travel to Earth, causing this drop in expected ν_e flux (ν_e disappearance).

2.3.4 Measuring the Oscillation Parameters

The Super-K and SNO experiments opened the path to the first generation of reactor and accelerator neutrino oscillation experiments. KamLAND, combined with Super-K, SNO, and other solar neutrino experiments provided the best measurements of the mixing parameters Δm^2_{12} and θ_{12} (the so-called "solar" mixing parameters). KamLAND is a large spherical detector containing a nylon balloon filled with 1 kT of liquid scintillator [1]. This active area is observed by 1879 PMTs (Figure 2.7).

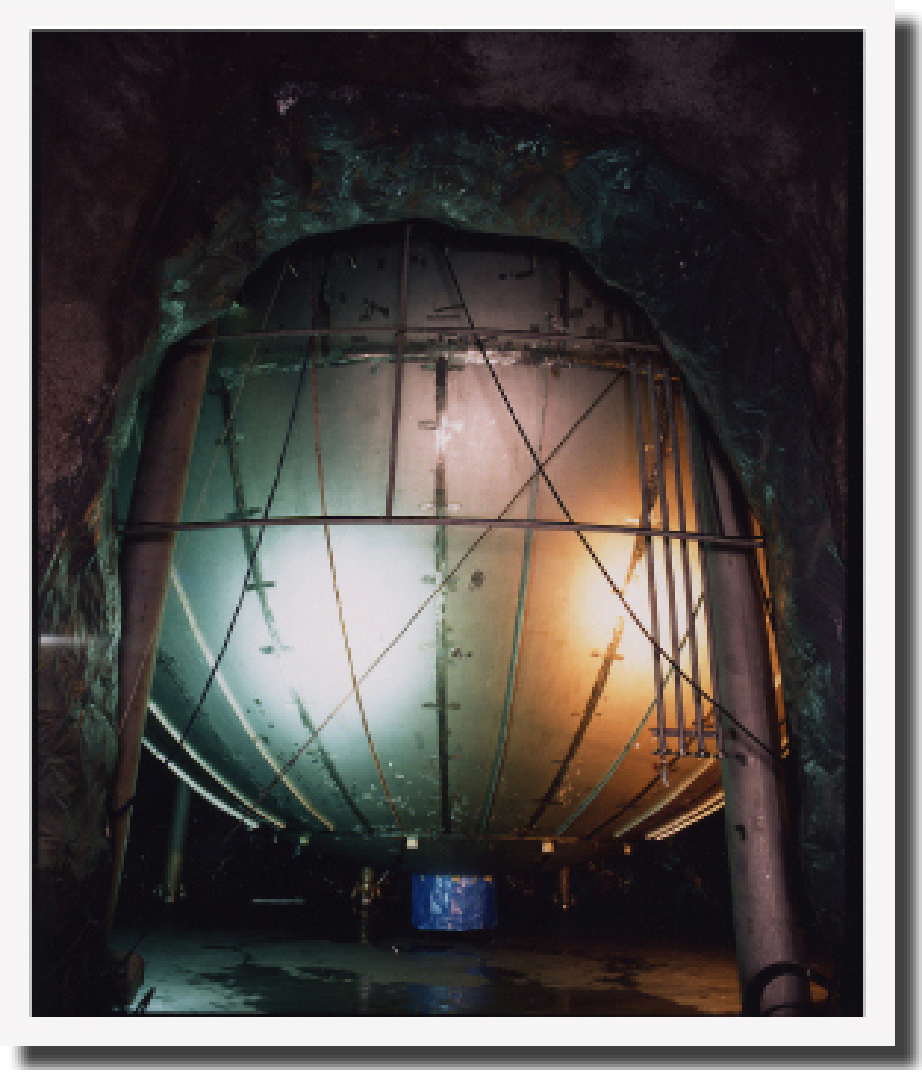

Figure 2.7: The KamLAND Detector [1]

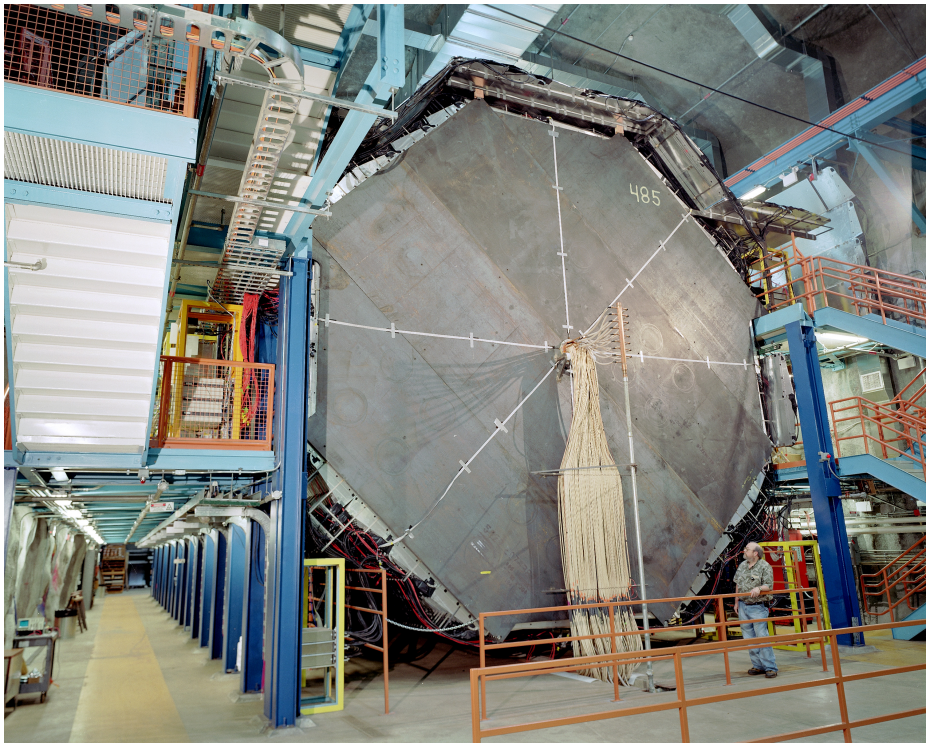

Figure 2.8: The MINOS Far Detector [23]

KamLAND records data from 55 nuclear power stations in the surrounding area (average distance of ∼180 km).

The "atmospheric" mixing parameters Δm^2_{23} and θ_{23} were measured by Super-K and the accelerator experiments MINOS and K2K. K2K used the KEK accelerator complex to send a beam of ν_μ to be detected in the Super-K detector [4]. MINOS used a Near Detector at Fermi National Accelerator Laboratory (Fermilab) and a Far Detector at the Soudan mine in Minnesota to look at ν_μ disappearance in the Neutrinos from the Main Injector (NuMI) beam [23]. The MINOS detectors were constructed from bidirectional planes of scintillating strips alternating with steel plates (Figure 2.8). The detector was placed in a magnetic field for energy reconstruction of muonic tracks, and the scintillating strips gave position information; because the planes were stacked in two different directions, complete three-dimensional hit information could be reconstructed.

(a) Daya Bay (Schematic) [6]

(b) Double Chooz [9]

(c) RENO (Schematic) [21]

Figure 2.9: Second-Generation Reactor Experiments

The final mixing angle theta 13 (ϑ_{13}) was much more difficult to measure, because of its small value relative to the other two angles. The CHOOZ experiment in France placed the first upper limit on ϑ_{13}, but it was not until the second-generation reactor experiments Daya Bay, Double Chooz and RENO came on-line that ϑ_{13} was conclusively shown to be non-zero; and in fact ϑ_{13} is "large" in terms of the allowed parameter space from previous experiments.

2.4 Oscillation Parameters

The Homestake experiment found that only a third of the expected flux from solar models was actually recorded in their detector. Neutrino oscillations were eventually proven to be the cause of this (See Section 2.3.2). In the theory of neutrino oscillations, neutrinos propagate in their mass states (labeled ν_1, ν_2 and ν_3), but charged-current interactions expose their weak flavor states and produce an associated lepton (e, μ or τ). The mass states are admixtures of the flavor states, so that after neutrinos have been allowed to propagate some distance through matter, there is a nonzero probability of measuring a different flavor state than what was initially produced.

$$\begin{bmatrix} \nu_e \\ \nu_\mu \\ \nu_\tau \end{bmatrix} = \begin{bmatrix} c_{12}c_{13} & s_{12}c_{13} & s_{13}e^{-i\delta} \\ -s_{12}c_{23} - c_{12}s_{23}s_{13}e^{i\delta} & c_{12}c_{23} - s_{12}s_{23}s_{13}e^{i\delta} & s_{23}c_{13} \\ s_{12}s_{23} - c_{12}c_{23}s_{13}e^{i\delta} & -c_{12}s_{23} - s_{12}c_{23}s_{13}e^{i\delta} & c_{23}c_{13} \end{bmatrix} \begin{bmatrix} \nu_1 \\ \nu_2 \\ \nu_3 \end{bmatrix} \tag{2.6}$$

Equation 2.6, called the Pontecorvo-Maki-Nakagawa-Sakata (PMNS) matricies, describes this transformation from the neutrino mass states to their flavor states (which are eigenstates of the free-propagation Hamiltonian and the flavor interaction operators). In the matrices shown, c_{ij} stands for $cos(\theta_{ij})$ and s_{ij} stands for $sin(\theta_{ij})$. Neutrino mass states propagate as plane waves, and this can be approximated using the ultra-relativistic limit and noting that t is approximately L as neutrinos travel at close to the speed of light (Equation 2.7).

$$|\nu_i(L)\rangle = e^{-im_i^2 L/2E} \; |\nu_i(0)\rangle \tag{2.7}$$

Using these two equations, we can find the three-flavor survival and appearance probabilities for any given transformation. For example, using the best measured values for θ_{12}, ϑ_{13}, θ_{23}, Δm_{12}, Δm_{23}, and assuming $\delta_{CP} = 0$ and normal hierarchy gives appearance probabilities over the entire NOνA L/E range (Figure 2.10)

2.5 CP Violation

The main effect of CP-violating processes is an observable difference in the behavior of neutrinos versus anti-neutrinos. In the PMNS framework, a single Dirac CP phase (δ_{CP}) is responsible for all neutrino/anti-neutrino asymmetry. If neutrinos happen

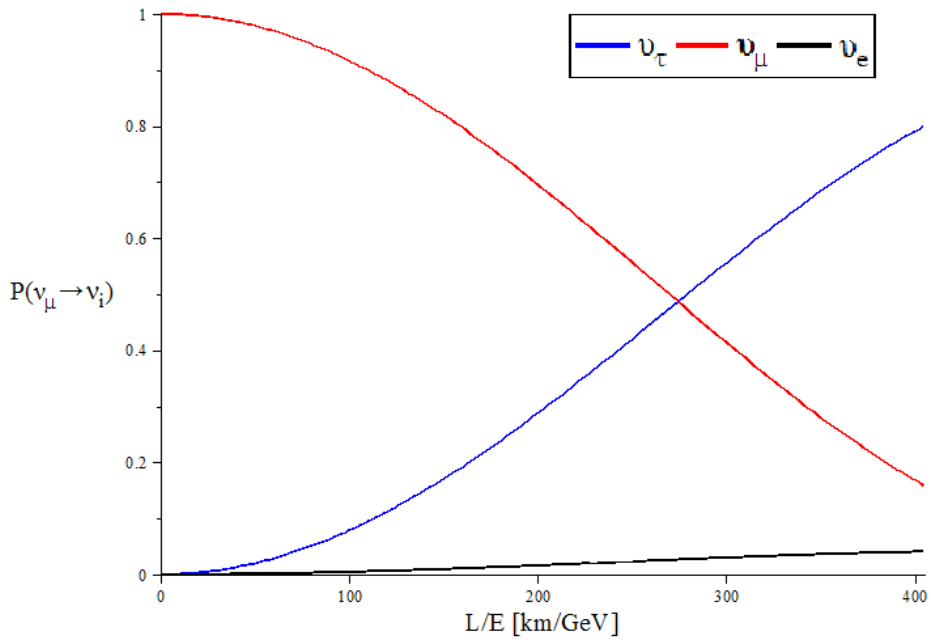

Figure 2.10: ν_μ Oscillation Probability over NOνA L/E Space

to be Majorana particles (the neutrino is its own antiparticle), two additional CP-violating phases appear, appended to the PMNS matrix (equation 2.8).

$$\begin{bmatrix} \nu_e \\ \nu_\mu \\ \nu_\tau \end{bmatrix} = \Big[PMNS\Big] \begin{bmatrix} 1 & 0 & 0 \\ 0 & e^{i\frac{\alpha_{21}}{2}} & 0 \\ 0 & 0 & e^{i\frac{\alpha_{31}}{2}} \end{bmatrix} \begin{bmatrix} \nu_1 \\ \nu_2 \\ \nu_3 \end{bmatrix} \tag{2.8}$$

Strong and electromagnetic force interactions conserve both C and P symmetry, but weak force interactions maximally violate both. All observed (anti)neutrinos have left(right) chirality. If either C or P were conserved in weak interactions, we would observe interactions with both left- and right-handed neutrinos and anti-neutrinos.

CP violation was first measured in the decay of neutral kaons. E.g., the process $K_L \rightarrow \pi^- e^+ \bar{\nu_e}$ occurs more often than $K_L \rightarrow \pi^+ e^- \nu_e$, allowing for a distinction between electrons and positrons [24]. It has yet to be observed in the lepton sector, though neutrinos may violate CP in a manner analogous to the original CP violator, K_L^0.

2.6 Mass Hierarchy

For oscillations to happen, neutrinos must have a non-zero mass. Direct measurements of the neutrino mass are extremely difficult; several experiments are looking at the high end of the beta decay spectrum in an attempt to determine the absolute scale mass (i.e. the KATRIN Experiment [31]). Oscillation experiments have determined the mass differences between the three mass states and these are relatively well-known. The mass splittings are measured in their quadratic forms, so their signs are not known, leading to the "mass hierarchy" problem: it is not known if the masses are in a "normal" order (i.e. 1,2,3) or "inverted" (3,1,2) (Figure 2.11). The mass difference between state 1 and state 2 is orders of magnitude smaller than the difference between 2 and 3.

SNO has measured the "normal" hierarchy for states 1 and 2 from solar neutrinos in the sun (the "matter effect"), meaning that ν_1 is lighter than ν_2 [2]. This result comes from forward scattering of neutrinos in the Sun's core, which causes the neutrinos to adiabatically change state from their initial flavor state (ν_e) to a pure mass state (ν_2). This matter effect is more pronounced in higher-energy neutrinos, and low-energy neutrinos oscillations are governed essentially by the vacuum PMNS matrix. In an "inverted" hierarchy for these states, we would expect to see 70% of the high-energy neutrinos as ν_e, but SNO instead measured 30%, or "normal" hierarchy.

2.7 Current Knowledge of Neutrino Mixing Parameters

As outlined above (Equation 2.6), there are six parameters for three-neutrino oscillation theory; three mixing angles, two mass splittings (the sign is measured seperately from the squared value), and a Dirac CP-violating phase (If neutrinos are instead Majorana particles, there are three separate CP phases). The mixing angle θ_{12} was measured using solar neutrinos, and θ_{23} was measured using atmospheric

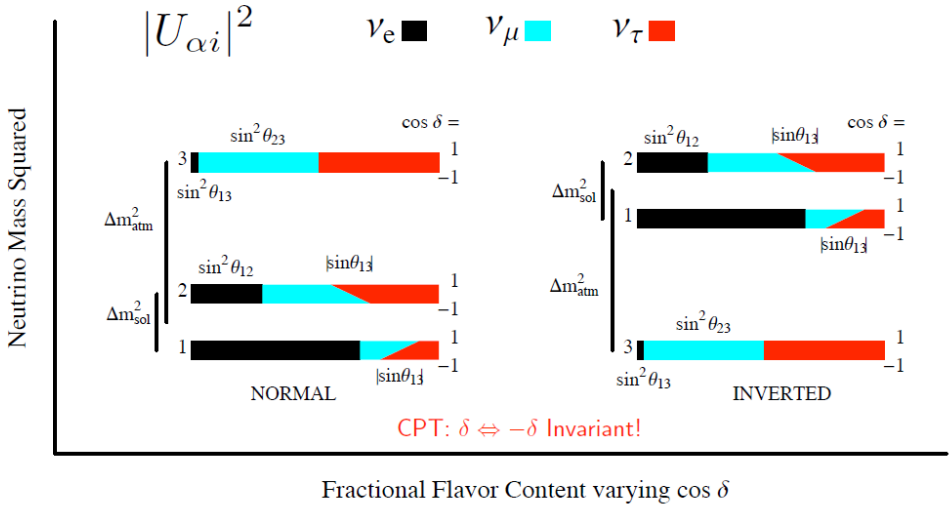

Figure 2.11: Flavor contents of the three neutrino mass states for the two possible mass hierarchies with various values of δ_{CP} Figure from [27]

neutrinos from cosmic rays. The two mass splittings have been measured by several different experiments, with the most recent being a result published by MINOS in 2011. The third mixing angle, ϑ_{13} is the subject of several current experiments such as Double Chooz, Daya Bay, and RENO. These experiments all use electron anti-neutrinos from nuclear power reactors as their source, and a long-baseline accelerator neutrino experiment using muon neutrinos provides a complementary result. NOνA has been optimized in favor of mass hierarchy resolution and measurement of δ_{CP} at the expense of ϑ_{13} sensitivity, however, the experiment will still offer a complementary measurement of ϑ_{13} to confirm the reactor experiments' results.

Table 2.1: Measured central values for oscillation parameters [24]

Parameter	Particle Data Group (PDG) Best-Fit Value
$sin^2(2\theta_{12})$	0.857 ± 0.024
$sin^2(2\theta_{23})$	> 0.95
$sin^2(2\theta_{13})$	0.095 ± 0.010
Δm^2_{21}	$(7.5 \pm 0.20) \times 10^{-5} eV^2$
Δm^2_{32}	$(2.32^{+0.12}_{-0.08}) \times 10^{-3} eV^2$
the Dirac CP-Violating Phase (δ_{CP})	Not yet measured

Table 2.7 outlines the current values of the neutrino mixing parameters. The large value of ϑ_{13} has raised questions about some of the other parameters in the full three-neutrino mixing model, namely whether θ_{23} is in the higher or lower octant (greater or less than 45 degrees). Previous to 2012, oscillation experiments assumed a two-neutrino model, discounting ϑ_{13} as very small (as measurements at the time suggested), and this greatly simplified their analyses. Since the new generation of reactor experiments has measured ϑ_{13} to be just below the sensitivity of the older experiments (in essence, the largest value allowed by them), the old results must be re-analyzed with a full three-neutrino model in mind. This re-analysis did slightly affect the measured values for the oscillation parameters.

Chapter 3

NOνA Experiment Overview

3.1 Introduction

The NuMI Off-Axis ν_e Appearance (NOνA) Experiment is designed to search for electron neutrino (ν_e) appearance from the muon neutrino (ν_μ) Neutrinos from the Main Injector (NuMI) beam at a long baseline of 810 km (Figure 1.1) at an off-axis angle of 14 milliradians.. The experiment is a large collaboration, with more than 200 scientists, engineers, and students from 38 institutions in 7 countries (Figure 3.1). NOνA uses PVC plastic cells filled with liquid scintillator, allowing for a very high "active" volume while preserving good spatial resolution at comparable cost to other large liquid-scintillator detectors (i.e. KamLAND). The full data run is scheduled to last for 6 years, three in NuMI's "neutrino" mode and three in "anti-neutrino" mode. As a part of the NOνA design criteria, the power of the NuMI beam will be upgraded to 700 kW; this upgrade ties into Fermi National Accelerator Laboratory (Fermilab)'s Proton Improvement Plan. The Far Detector (FD) was completed in July 2014, and the Near Detector (ND) was on-line shortly thereafter. NOνA's design allows for very good electromagnetic shower reconstruction, and a narrow gate around the beam "spill" will significantly reduce any backgrounds, allowing for precision counting of beam neutrinos. Due to the totally-active nature of NOνA's readout, NOνA also can

Figure 3.1: NOνA Collaboration at Argonne National Laboratory, July 2013

use Data-Driven Triggers (DDT), running on-the-spot analysis of the data stream and saving events that may be of interest for other physics analyses.

3.2 NOνA Physics Goals

NOνA's goal is to make a high-precision measurement of $\nu_\mu \rightarrow \nu_e$ oscillations (and the anti-neutrino counterpart) by the appearance of ν_e in the primarily ν_μ NuMI beam (See Section 3.4). The experiment uses two detectors to reduce beam-line systematics (since the neutrinos are secondary particles from the decay of pions and kaons, it is very difficult to predict the exact flux or energy of beam neutrinos). This measurement will allow for a resolution of the neutrino mass hierarchy as well as making a determination of the Dirac CP-Violating Phase (δ_{CP}), as well as providing a reactor-independent, high-precision measurement of theta 13 (ϑ_{13}). For some combinations of mass hierarchy and δ_{CP}, NOνA will be unable to make an

exact determination of their values (Figure 3.2, Note the overlapping regions of the contours). In that case, there are several possible solutions, including an energy-binning scheme (Figure 3.3) or longer runtime, that may yet allow NOνA to resolve these two parameters.

NOνA will also take advantage of its constant-readout design to allow for the study of additional physics beyond its primary mission. Of special interest is using NOνA as a supernova telescope, as it would be able to observe the neutrino burst that accompanies these events. NOνA could possibly shed more light on the neutrino flux from Core-Collapse (Type IIa) supernovae, assisting in the development of astrophysical models. NOνA may also be sensitive to so-called "exotic" particles, such as axions, magnetic monopoles, sterile neutrinos, and other "Beyond Standard Model" signals.

3.2.1 Theta 13 Measurement

The $\nu_\mu \rightarrow \nu_e$ neutrino appearance channel is sensitive to the value of ϑ_{13} (Equation 3.1). NOνA's measurement will not have the same precision as contemporary reactor-based experiments, but it should serve to confirm the result and also prove NOνA's effectiveness in measuring neutrino oscillations. Since ϑ_{13} is "large", NOνA has a better chance of observing δ_{CP} and the mass hierarchy (Figure 3.4).

$$P_{\nu_\mu \rightarrow \nu_e} = |\sum_i U^*_{\mu i} U_{ei} e^{-i m_i^2 L/2E}|^2, \text{ U}_{\alpha\text{i}} \text{ are elements of the matrix 2.6} \qquad (3.1)$$

NOνA will also be able to make a measurement of theta 23 (ϑ_{23}), and if it is non-maximal, NOνA is sensitive to the "octant" (whether $sin(2 * \theta_{23})$ is positive or negative).

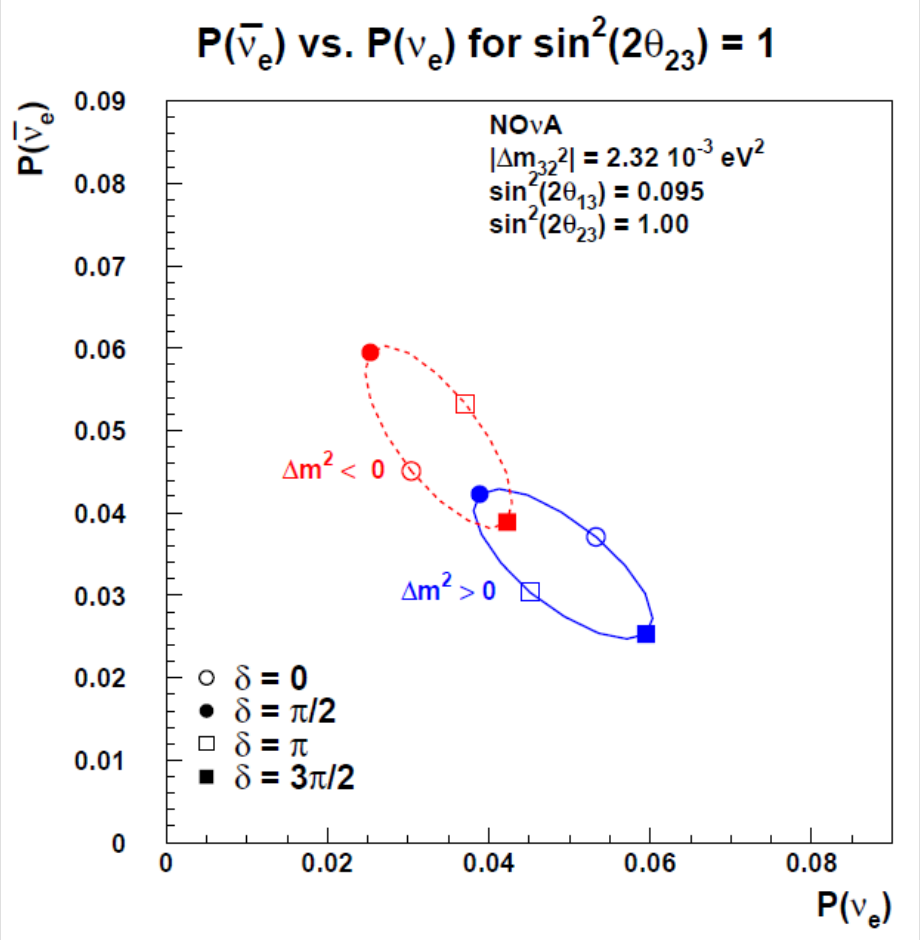

Figure 3.2: This plot demonstrates the principle by which NOνA determines the mass hierarchy and measures the CP phase. NOνA essentially measures two oscillation probablities, one in neutrino mode (a point on the x-axis) and one in anti-neutrino mode (a point on the y-axis). The ellipses show the δ_{cp} values and choice of hierarchy that could yield from the oscillation probability measurements given a $sin^2(2 * \theta_{13})$ value. The blue curves are for the normal hierarchy and the red curves are for the inverted hierarchy. On each ellipse, the choice of the CP phase δ varies as one moves around the ellipse as indicated by the symbols. This assumes maximal mixing in the ϑ_{23} octant. [25]

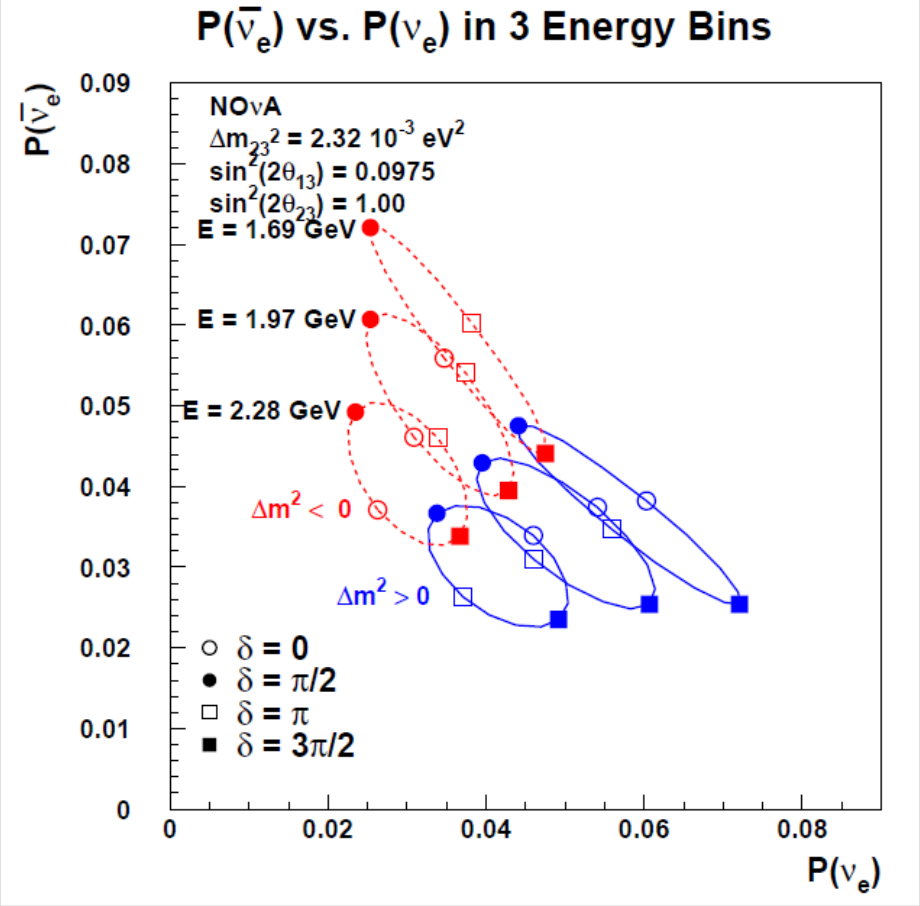

Figure 3.3: This plot demonstrates the principle by which NOνA determines the mass hierarchy and measures the CP phase. NOνA essentially measures two oscillation probablities, one in neutrino mode (a point on the x-axis) and one in anti-neutrino mode (a point on the y-axis). The ellipses show the δ_{CP} values and choice of hierarchy that could yield from the oscillation probability measurements given a $\sin^2(2*\vartheta_{13})$ value. The blue curves are for the normal hierarchy and the red curves are for the inverted hierarchy. On each ellipse, the choice of the CP phase delta varies as one moves around the ellipse as indicated by the symbols. This assumes maximal mixing in the ϑ_{23} octant. [25]

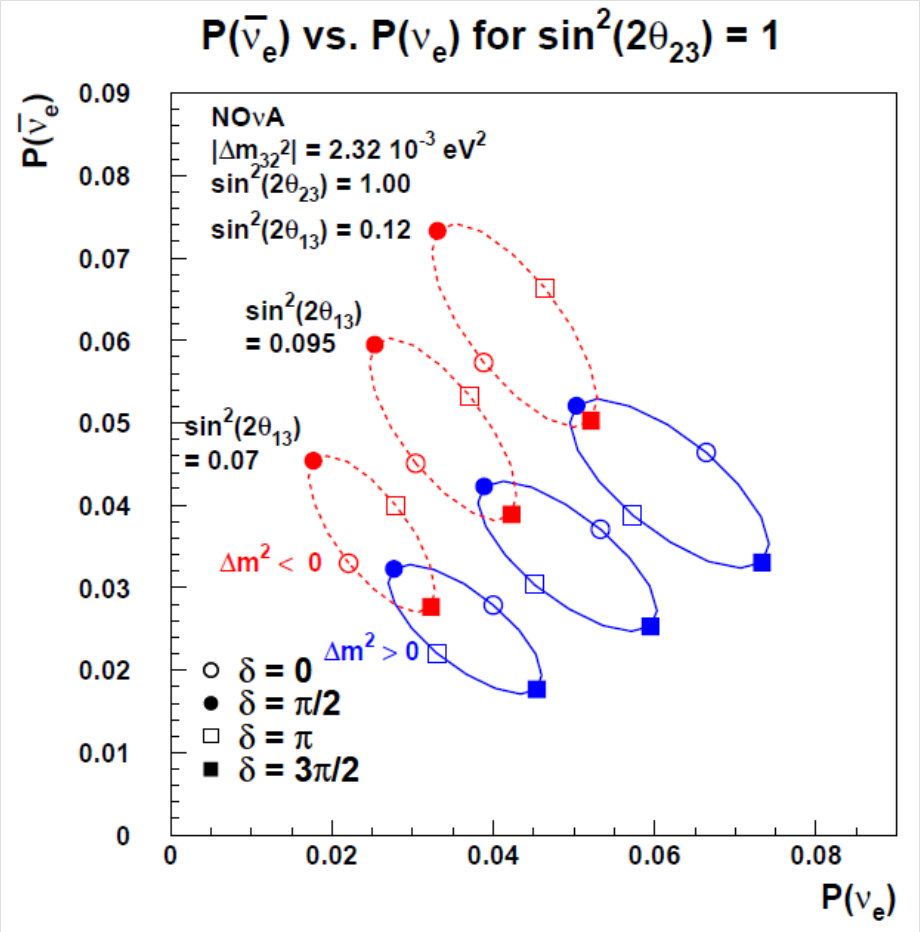

Figure 3.4: This plot demonstrates the principle by which NOνA determines the mass hierarchy and measures the CP phase. NOνA essentially measures two oscillation probabilities, one in neutrino mode (a point on the x-axis) and one in anti-neutrino mode (a point on the y-axis). The ellipses show the δ values and choice of hierarchy that could yield from the oscillation probability measurements given a $sin^2(2 * \theta_{13})$ value. The blue curves are for the normal hierarchy and the red curves are for the inverted hierarchy. On each ellipse, the choice of the CP phase δ varies as one moves around the ellipse as indicated by the symbols. This assumes maximal mixing in the ϑ_{23} octant. [25]

3.2.2 Mass Hierarchy and CP Violation

One of the remaining parameters in the neutrino oscillation model is the sign of the mass differences between the three neutrino mass states. This "hierarchy" problem is physically interesting because in the case of "inverted" hierarchy, neutrinos would act differently than other leptons and quarks, with the 3rd neutrino mass state (which mixes primarily to ν_τ) being the lightest mass state. NOνA has been optimized in favor of this measurement, at the expense of ϑ_{13} sensitivity.

The final parameter in the PMNS matrix is δ_{CP}. Depending on the value of δ_{CP}, neutrinos may participate in the mechanism by which the observed matter/antimatter asymmetry of the universe was created.

NOνA will make a measurement of $\mathrm{P}(\nu_\mu \rightarrow \nu_e)$ and of $\mathrm{P}(\bar{\nu_\mu} \rightarrow \bar{\nu_e})$ in order to achieve these physics goals. These measurements together will help to constrain the possible values of the mass hierarchy and of δ_{CP} (Figure 3.5).

3.3 NOνA Detector Construction

NOνA's three detectors are made using a cellular structure. Each cell is 4.5 cm by 6.6 cm in cross-section and the PVC extrusions are the full length of the detector in either the horizontal or vertical direction. Cells are arranged into 32-cell modules (Figure 3.6a), and these modules are stacked to form a "plane" (Figure 3.6b). 32 planes form a "block" (Figure 3.6c), and two blocks together are called a "diblock" (DB). The diblock is the basic depth unit of the Data Acquisition (DAQ) coordinate system, as each Data Concentrator Module (DCM) reads out 1 module position from each of the 64 planes in a diblock. All of the cells in a single plane are oriented in the same direction, and the planes alternate between horizontally-oriented cells and vertically-oriented cells. Regardless of orientation, the 6.6 cm width of the cell is perpendicular to the beamline direction (i.e. the width of a single plane as seen by the beam is 6.6 cm). The cellular nature of the detector allows for at least two

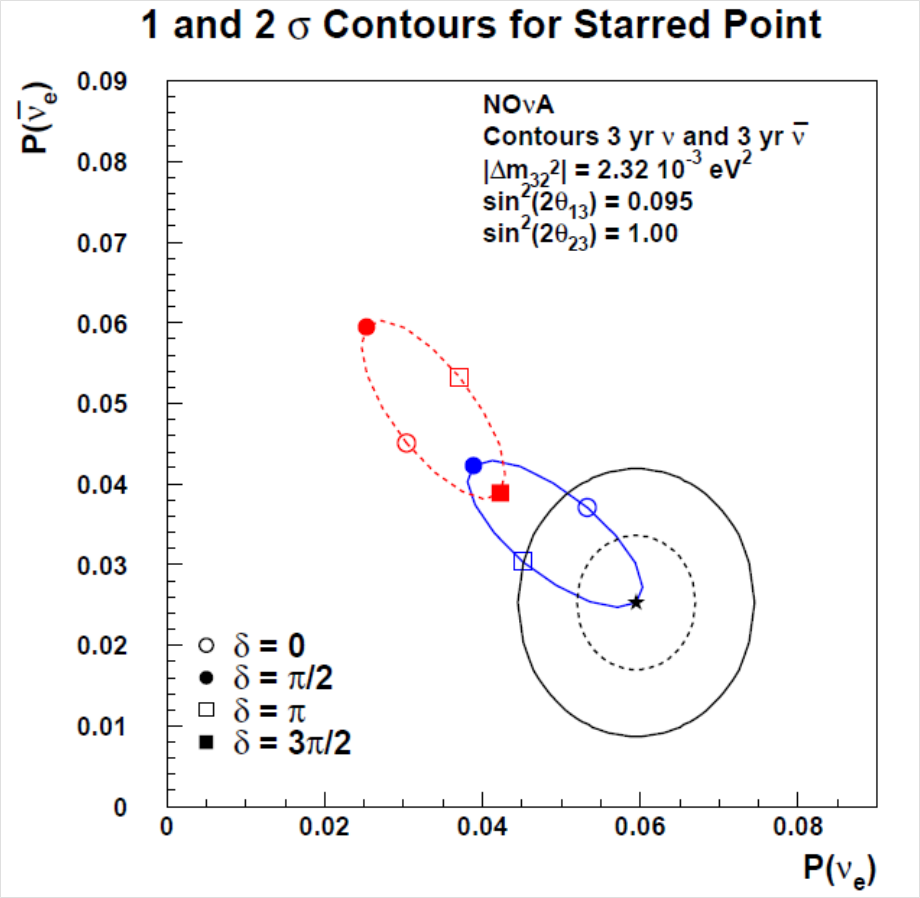

Figure 3.5: This plot demonstrates the principle by which NOνA determines the mass hierarchy and measures the CP phase. NOνA essentially measures two oscillation probablities, one in neutrino mode (a point on the x-axis) and one in anti-neutrino mode (a point on the y-axis). The ellipses show the δ_{cp} values and choice of hierarchy that could yield from the oscillation probability measurements given a $sin^2(2 * \theta_{13})$ value of 0.095. One can imagine that NOνA makes a measurement of oscillation probability in each neutrino mode (after 3 years of running in each mode) that yields the starred point. The contours are the 1- and 2-σ measurements assuming oscillations with the parameters chosen at the starred point. The hierarchy is resolved and CP phase is constrained for particular values of δ at the 2-σ level. This assumes maximal mixing in the ϑ_{23} octant.[25]

(a) A NOνA Module at the NOνA Module Factory at the University of Minnesota

(b) The final NOνA Module being stacked on Block 27

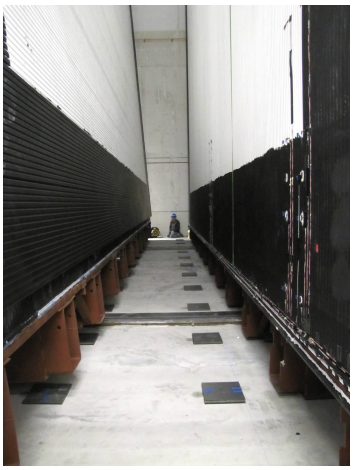

(c) Block 27 being placed next to Block 26

Figure 3.6: NOνA Construction and Assembly Process (Far Detector shown, Near Detector procedure was similar, but on a smaller scale).

Cartesian coordinates to be known for every cell hit (X and Z for vertical planes, Y and Z for horizontals), and the third can be inferred by looking at nearby hits along the path of the particle through the detector. The NOνA liquid scintillator is made of mineral oil with 4% by volume pseudocumene, 0.09% PPO and 0.0013% bis-MSB (PPO and bis-MSB are the scintillating fluorescent compounds). Each cell is filled with this liquid scintillator and strung with a loop of wavelength-shifting fiber. Each module of cells is linked to a 32-channel Avalanche Photodiode (APD) (2 ends of the fiber from each cell to each channel), which is read-out by an attached Front-End Board (FEB). These FEBs report to a DCM) which organizes the data and sends it to a farm of buffer nodes.

3.3.1 Near Detector On Surface

The Near Detector On Surface (Figure 1.2c) was the first NOνA detector completed. It served as a full-scale prototype detector, demonstrating the effectiveness of the NOνA design. Near Detector On Surface (NDOS) was originally intended to become the ND, but it was shown that the 2 module by 3 module design used in NDOS would

be insufficient to contain energetic electron neutrino-like events. NDOS was originally comprised of three diblocks plus a muon catcher made of alternating NOνA planes and steel plates. The muon catcher has since been removed for re-use on the ND. The NDOS detector has shown its utility in diagnosing multiple hardware issues that would have caused significant costs and delays if NDOS had not been built. In the FD/ND era, NDOS continues to serve as a hardware test-bed, and will continue to produce data as long as there are FEBs and APDs present on the detector, and DAQ computers available.

3.3.2 Far Detector

The Far Detector (Figure 3.7) at Ash River, MN, 810 km from the NuMI target, is comprised of 14 diblocks; its total size is 51 feet tall by 51 feet wide by 240 feet. Each diblock is read-out by 12 DCMs, 6 on the horizontal modules, and 6 on the verticals. The data from the detector are fed into a large computer farm, where initial on-the-spot analysis is performed, and beam and other triggers are applied to save selected data. The buffer farm has been upgraded from the original specifications and is capable of holding a buffer of sufficient length for NOνA to participate in the Supernova Early Warning System (SNEWS) project to detect supernova neutrinos. The FD was built block-by-block, and as each block was put into place, the previously-completed blocks were filled with liquid scintillator and electronics were installed. This meant that the FD started producing data well before completion, allowing for early analyses and hardware checkouts to be performed.

3.3.3 Near Detector

The 330 ton Near Detector (Figure 3.8) is centered at the same 14 mrad off-axis angle as the FD, but is only 1 km from the beam target. From observations made with the NDOS detector, it was decided that the ND should be wider than the NDOS; it is 3 modules by 3 modules. The ND, like NDOS, is three diblocks of fully-instrumented

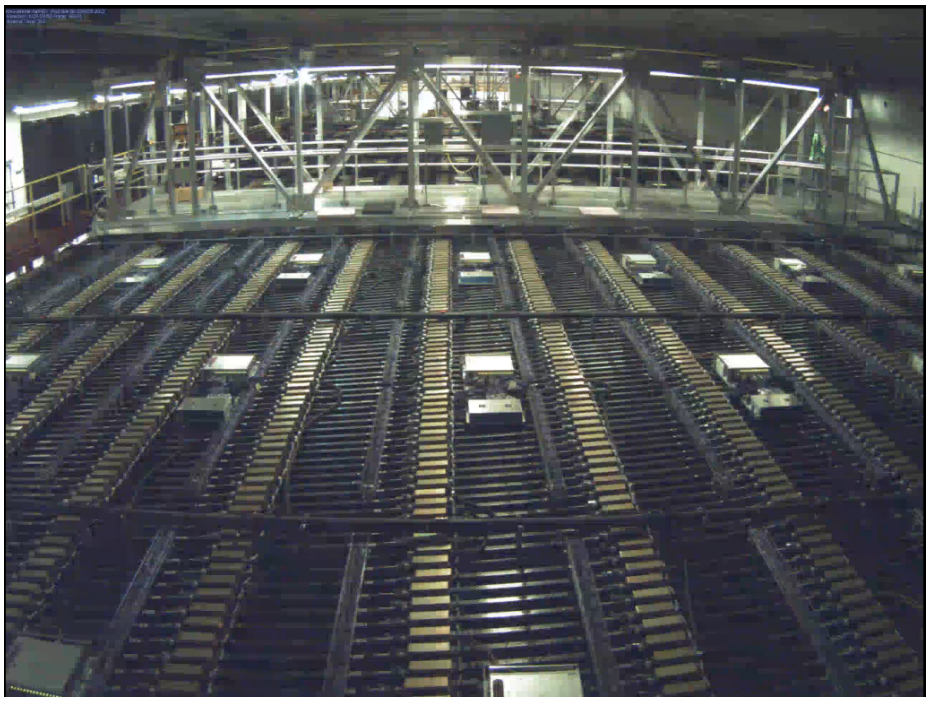

Figure 3.7: View of the top of the FD, the electronics boxes for the first three diblocks can be seen

detector, and the NDOS muon catcher was moved underground to serve as the ND muon catcher (denoted as DB4 in the DAQ systems). Initially, NDOS and the ND shared computing resources, but computing resources were allocated from the FD cluster expansion to serve as the new ND computing cluster.

3.4 The NuMI Beamline

The NuMI beam uses 120 GeV protons from the Main Injector at Fermilab and a Carbon (during the NOνA era, the Carbon will be replaced with Beryllium) target to produce pions and kaons (Figure 3.9). These are focused through magnetic "horns" which focus particles with a certain charge and defocus particles with the opposite charge. The pions and kaons then enter a 200 m long decay pipe where they decay into muons and muon neutrinos. Equations 3.2 and 3.3 detail this process for pions, and equations 3.4, 3.5 and 3.6 detail the most common decays for kaons (decay

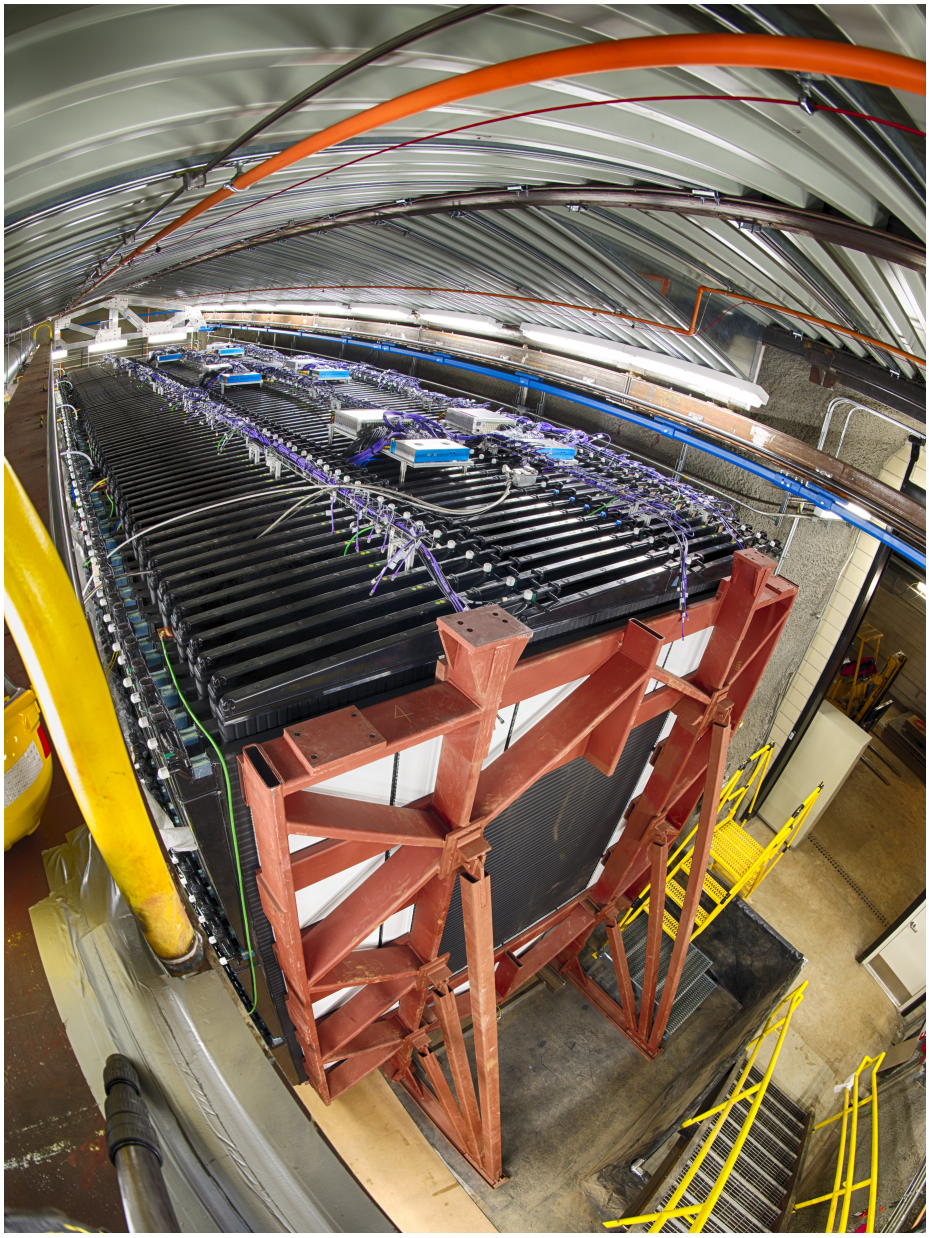

Figure 3.8: View of the top of the ND, showing the DCMs on the top of the detector and the "bookend" support.

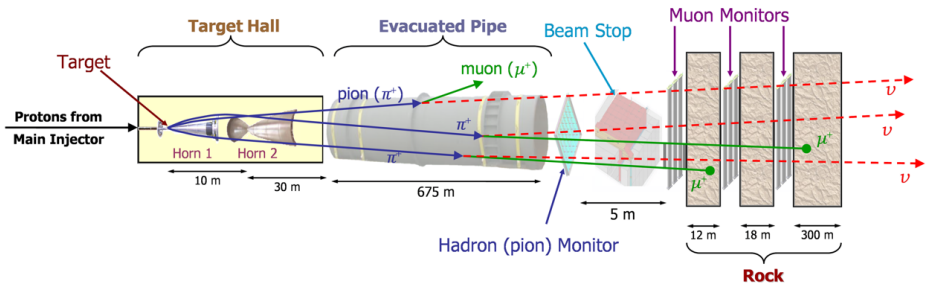

Figure 3.9: Schematic diagram of the NuMI beam. Protons create pions and kaons at the target, which are focused through the magnetic horns. These hadrons decay into muons and ν_μs in the decay pipe, and then the remaining hadrons and muons are absorbed, leaving a ν_μ beam. Adapted from [15]

probabilities from [24]). The muons are stopped in rock shielding to produce a nearly-pure ν_μ beam. Since this is an indirect particle production process, the neutrinos are actually produced in a relativistic cone, with strong energy dependence on the angle relative to the beamline center. Also, because of the multiple decays, the beam is not mono-energetic; modeling the number and energy of neutrinos from the beam for a given Protons On Target (POT) value is an evolving science, informed by the observations of previous NuMI experiments.

$$\pi^+ \to \mu^+ + \nu_\mu \qquad \pi^- \to \mu^- + \bar{\nu_\mu} \qquad (99.98\%) \qquad (3.2)$$

$$\pi^+ \to e^+ + \nu_e \qquad \pi^- \to e^- + \bar{\nu_e} \qquad (0.01\%) \qquad (3.3)$$

$$K^+ \to \mu^+ + \nu_\mu \qquad K^- \to \mu^- + \bar{\nu_\mu} \qquad (63.55\%) \qquad (3.4)$$

$$K^+ \to e^+ + \nu_e \qquad K^- \to \pi^0 + e^- + \bar{\nu_e} \qquad (5.07\%) \qquad (3.5)$$

$$K^+ \to \pi^+ + \pi^0 \qquad K^- \to \pi^- + \pi^0 \qquad (20.66\%) \qquad (3.6)$$

3.4.1 Horn Current

NuMI's magnetic focusing horns can be run in either "neutrino" mode or "anti-neutrino" mode, depending on the current direction. In Forward Horn Current

(FHC), positively-charged kaons and pions are focused and negatively-charged ones are defocused, producing a mainly neutrino beam; while in Reverse Horn Current (RHC) the opposite is true, producing a higher flux of anti-neutrinos. Production of anti-neutrinos in the RHC, or "anti-neutrino" mode is lower relative to neutrinos in FHC, or "neutrino" mode, however, due to the positive charge of the incident protons from the Main Injector. Therefore, in "anti-neutrino" mode, the anti-neutrino rate is enhanced relative to "neutrino" mode, but the beam still contains a significant fraction of neutrinos. Also, anti-neutrino interactions have lower cross-sections by a factor of two relative to neutrino cross-sections (Figure 2.2), leading to lower event rates.

3.4.2 Energy Spectra

The primary motivation for NOνA's off-axis location is that as you go off-axis, the beam's wide energy spectrum in the central position narrows significantly to a well-peaked spectrum centered about 2 GeV (Figure 3.10), due to momentum conservation during the in-flight decays of the pions and kaons producing the beeam. This allows NOνA to do precise oscillation physics without energy reconstruction of neutrino events (though energy reconstruction does assist in this process, figure 3.3). Beam models such as FLUKA are used to generate these spectra, and they are, in turn, informed by what we know of the physics occurring in the beamline, weighted to match the observed spectrum at MINOS. However, systematic errors will be significantly reduced through accurate energy reconstruction as it frees the experiment from dependence on models and statistical analyses of spectra; this is why the absolute-scale energy reconstruction (See Chapter 5) is so important.

3.5 Data-Driven Triggers

The NOνA Far Detector is designed to deliver its data stream to a farm of buffer nodes, so that the trigger signal has time to make its way from Fermilab to Ash River. The

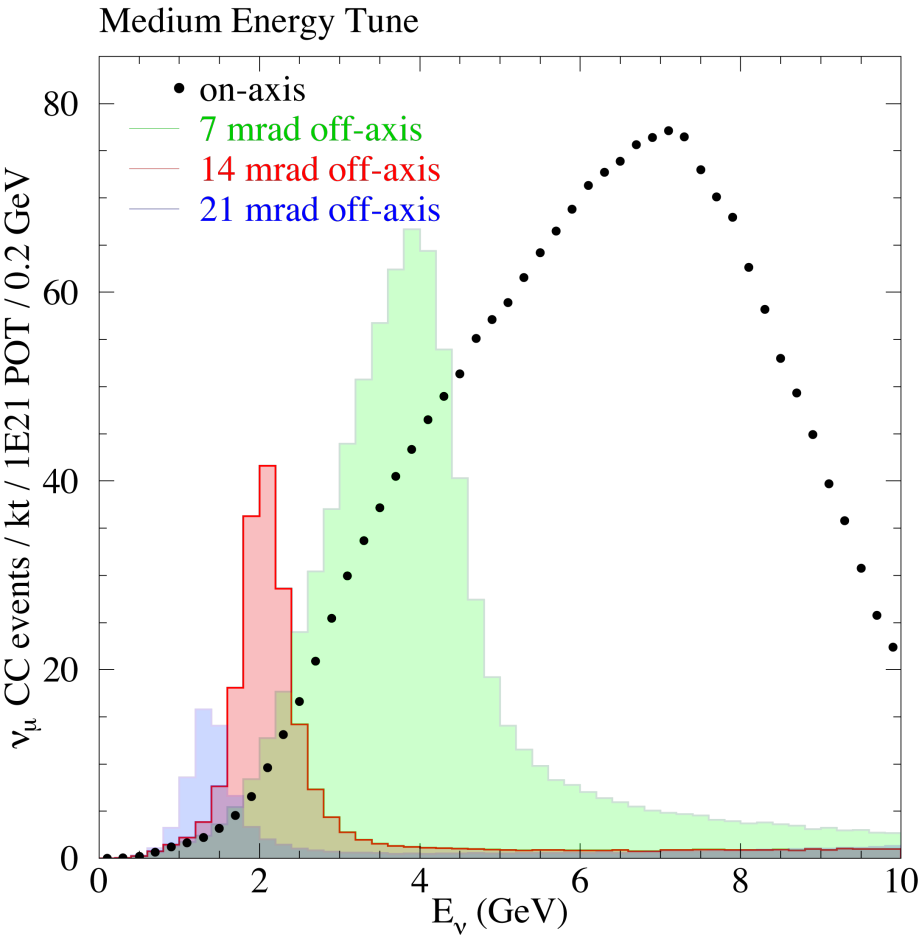

Figure 3.10: NuMI neutrino energy distribution predictions for on-axis and several off-axis locations. NOνA is at the 14 mrad location.[26]

nominal depth of this buffer was 20 seconds of full-detector data (See [26], Section 15.2). Advancements in computing technology since the Technical Design Report, [26] (TDR) was published, however, have increased the capabilities of the DAQ system to the point where the system is capable of buffering the entire data stream for up to 30 minutes. While the data reside in this buffer, DDT algorithms may be run on "microslices" (roughly ∼50 μs of whole-detector live-time) that reside in each buffer node. Each DDT algorithm searches for a particular event type, and any events satisfying a DDT are written to a special data stream.

3.5.1 Supernovae

NOνA is a large, surface-level neutrino detector. It has the unique ability to observe any other particle flux that may accompany the neutrinos released in a nearby supernova. In addition to the standard DDT process that searches for neutrino events in the detector, the extreme depth of the data buffer allows NOνA to receive and act on SNEWS triggers, saving several seconds of live-time directly to disk.

3.5.2 Monopoles

Magnetic monopoles, if they exist, would have highly ionizing behavior and a characteristic speed through the detector. NOνA is sensitive to both "fast" and "slow" monopoles, and a DDT trigger has been written to search for the tell-tale, large ionization trail of such an event.

3.5.3 Other Physics

The DDT are designed around a "plug-in" trigger system so that new triggers can be defined without having to re-code parts of the Global Trigger, the DAQ process which issues all triggers, whether beam, random, or DDT. The first DDT trigger implemented is the so-called "Tri-Cell" trigger, which saves any microslice containing a cluster of at least three adjacent hits (useful for constraining the path length

through the center cell). Other DDT triggers include an energy-based trigger and a ν_μ trigger. This system allows for NOνA collaborators to define their own custom physics searches without affecting the primary data-taking mission of the experiment. The main limitation is the "decision time" for a trigger, or the amount of time that a trigger may spend reconstructing a single event before it is no longer available. This also affects the live-time of the trigger as it will skip data to "catch up" if it gets behind. For this reason, there is no DDT ν_e trigger as the reconstruction of a long muon track is much simpler than than reconstructing an electromagnetic shower. One such trigger-definition effort is the "hidden sector" searches being performed at the ND by Athanasios Hatzikoutelis of the University of Tennessee (UT) HEP group. (for more information, see [5])

3.6 NOνASoft: Data and Monte Carlo Analysis

At the completion of a run, the File Transfer System copies the raw data file to the Enstore file archival system at Fermilab for offline reconstruction and analysis. The first step in reconstruction is to convert the raw data file into a ROOT-format file. The full NOνA Offline software (NOνASoft) analysis chain is run on each file, producing the Common Analysis Framework (CAF) file, which contains ntuple data that are the basis for any collaborator's physics analysis. NOνASoft data or Monte Carlo Simulation (MC) analysis can be broken into three steps: "reco", or data reconstruction, consisting of calibration followed by track and vertex identification, Particle Identification (PID) (mostly concerned with ν_μ and ν_e), and CAF file production (Figure 3.11).

NOνA used a "blind analysis" paradigm for the development of all reconstruction and PID algorithms. Once the detector integration was completed and the first neutrinos were observed in the detector, certain parts of the parameter space were "black boxed" and analysis developers were not allowed use data from "inside the box". The advantage of this method is that it prevents biasing the data by developing

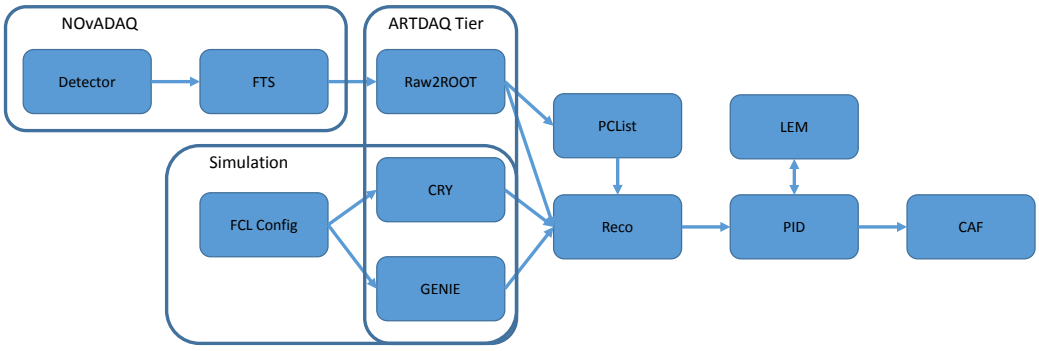

Figure 3.11: Flow diagram of the NOνA Production and Reconstruction chain. Data from the detector is converted into the NOνASoft ROOT format, and then "PCList" calibration reconstruction is run. Simulations use FhiCL configuration language and are run both on-site and off-site on the OSG. Reconstruction and PID passes are run, then the LEM PID is run separately. Once the results from LEM are re-integrated into the data file, CAF files are produced.

analysis code tuned to a sample of observed events, but it also has led to a very great reliance on Monte Carlo models within the collaboration (instead developing code tuned to a sample of simulated events with unknown real-world accuracy). My background study (Chapter 6) gets around the blindness requirement by applying the PID reconstruction to a signal sample where no events are expected to pass (the random, "cosmic" trigger).

3.6.1 Production

NOνASoft includes a MC simulation suite to generate both cosmic and beam-like events. MC files are created in the same format as data files, allowing for reconstruction tools to be developed using MC and then tuned using detector data. For each detector, MC is generated using CRY for cosmics and GENIE for beam neutrinos. GENIE simulations are broken down by NuMI horn current direction and, for the FD, whether or not the ν_μ has been swapped for ν_e.

As a member of the Production group, I was responsible for submitting both data analysis and simulation jobs to the Open Science Grid (OSG). Using the OSG, we

were able to achieve unprecedented speed for our simulations, running the entire FD cosmic simulation set in 20 hours (previously, this same generation had taken on the order of 2 weeks).

3.6.2 Reconstruction

The first step in data reconstruction is running the Calibrator module to convert the Analog-to-Digital Converter (ADC) units coming from the detector into "PECorr" or photo-electron signal. This is then in turn converted into energy units. After the data is calibrated, it is sorted into time-space "slices" by the "Slicer4D" package. The goal of Slicer4D is to reduce the number of noise hits which the two tracking algorithms have to try and reconstruct. It also guarantees that all of the hits in a slice are causally linked. The outputs from the two tracking algorithms, the Kalman tracker and the Cosmic tracker (which uses a Hough transform algorithm), are used as the inputs to the PID algorithms.

3.6.3 Particle Identification

NOνASoft has several event-identification algorithms it uses to determine the probability that a given event is a neutrino event. These use different heuristics to assign a probability value to an event based on trained artificial neural networks.

There are separate analysis groups for ν_e and ν_μ. Each has developed a set of PID packages for performing their analysis. The analysis scheme for ν_μ is to identify muonic tracks (package ReMId), reject cosmics (CosRej), and then find the energy of the ν_μ (NumuEnergy and QePId). The ν_e PID first "preselects" events based on the reconstructed energy and vertex location. Two ν_e PID algorithms use reconstructed showers, while a third tries to identify events based on reconstruction variables. The final ν_e PID, Library Event Matcher (LEM), uses a library of simulated events and compares these events to each event in the preselected sample, assigning a similarity

score to each. These are used as the inputs to the LEM neural network, which then reports how ν_e-like the event was.

3.6.4 Common Analysis Framework (CAF)

NOνASoft uses the ROOT-based ART framework for processing and storing data. ART has many useful data-handling features that are not present in basic ROOT. ART is, however, geared towards running analysis algorithms, and does not provide for visualization of variables across events. CAF files are standard ROOT files containing many of the final products from the data reconstruction in easy-to-use ROOT TTree format. This allows for analysis to be done using standard techniques and does not require the user to be intimately familiar with the analysis code in question. Even for the developers of analysis code, CAF files are a useful end-point as they allow for the creation of histograms with a few simple commands, allowing for algorithmic verification and parameter tuning based on the aggregate results from an entire sub-run.

Chapter 4

NOνA DAQ software

4.1 Introduction

NOνA DAQ software (NOνADAQ) refers to the online, or readout software which acquires data from the detectors. It is not concerned with event reconstruction (offline) or the Data-Driven Triggers (DDT), which are handled by separate code repositories. The Data Acquisition (DAQ) software ensures that the correct data are read out and saved when triggered, and that any exceptions that happen during this process are sent to Run Control for display on Control Room monitors. NOνADAQ interfaces to the DDT system for the generation of non-beam triggers, and sends event data to special versions of the offline Event Display module for monitoring of data quality.

My contributions to the NOνADAQ include thermal monitoring software designed to protect the computing hardware at the Ash River Computing Center (ARCC), overall expertise in the DAQ software for diagnosing and fixing bugs that may span several subsystems, and system-level expertise which I used to set up the DAQ for the Near Detector (ND). Without my contributions, NuMI Off-Axis ν_e Appearance (NOνA) would be without a working ND DAQ, would not be able to take Supernova

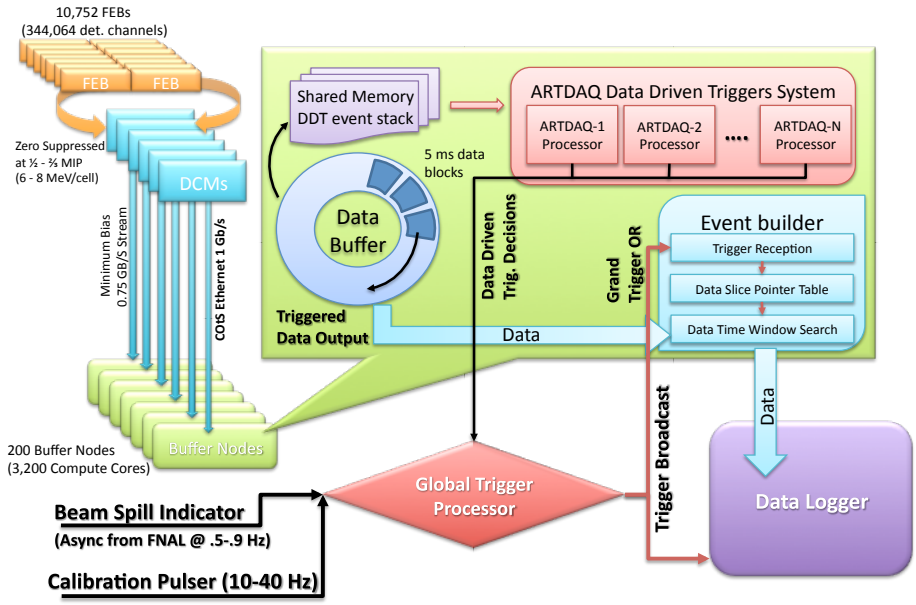

Figure 4.1: Diagram of the DAQ Software System, with data flow and control channels labeled.

Early Warning System (SNEWS) triggers longer than ∼1 s, and would have frequent unexplained crashes due to cooling failures at Ash River.

4.2 DAQ Software Overview

4.2.1 Data Handling

At the core of the DAQ software is the process of recording, buffering, triggering and storing the data from the NOνA detectors. This process is managed by several different applications within the DAQ software. First, the Front-End Board (FEB) firmware, a low-level software driver for the FEBs on the detector, detects a charge deposition above a pre-set threshold in a channel of the Avalanche Photodiode (APD) connected to it. It digitizes this signal and packages the result into a nanoslice, containing only the timestamp and Analog-to-Digital Converter (ADC) value of the event. This nanoslice is then sent to the Data Concentrator Module (DCM), where the "DCMApplication" sorts all of the data from up to 64 FEBs into microslices.

These microslices are sent to the Buffer Farm, where an application called the "BufferNodeEVB", or Event Builder stores the microslices until either it needs the space for new microslices, the microslice passes a time-out value, or it receives a trigger message from the Global Trigger. When a trigger is issued, each Buffer Node Event Builder (BNEVB) sends any microslices it has in the trigger's time window to the DataLogger, which writes it to the appropriate data stream based on the trigger type. Several streams may be combined into a single data file, or each may have its own file, or any combination of these may be configured, at the experiment's behest.

I have written code to greatly improve the microslice time-out processing in the BNEVB, which was causing unacceptable delays sending data to the DataLogger. I have also implemented multi-threading in the DataLogger, allowing it to continue to receive and build events while it is waiting on the system disk to finish writing previous events. Disk I/O is usually considered to be the slowest part of any computing system.

4.2.2 Triggering and Timing

One of the key support processes in the DAQ system is the Global Trigger. The Global Trigger accepts triggers from several different sources, such as beam triggers from Fermilab, DDT triggers from the processes analyzing sets of microslices, called milliblocks on the buffer nodes themselves, or from built-in timers. The Global Trigger provides a trigger message with a start time, a duration and the trigger ID code. The Trigger Scalars DAQ application keeps track of the number of triggers that the Global Trigger has issued (Figure 4.2).

The timing system keeps all of the DCMs synchronized to a Global Positioning System (GPS) clock (Figure 4.3), accurate to less than one 64-MHz tick across the entire system. The DCMs distribute their timing information in turn to their FEBs. This timing system has been verified using an independent atomic clock. Detector syncs may be sent manually through the TDUControl interface, which also displays any error codes present in the timing system.

Figure 4.2: The Trigger Scalars, showing the total number of triggers issued, broken down by type, with a DDT subtotal and an overall total.

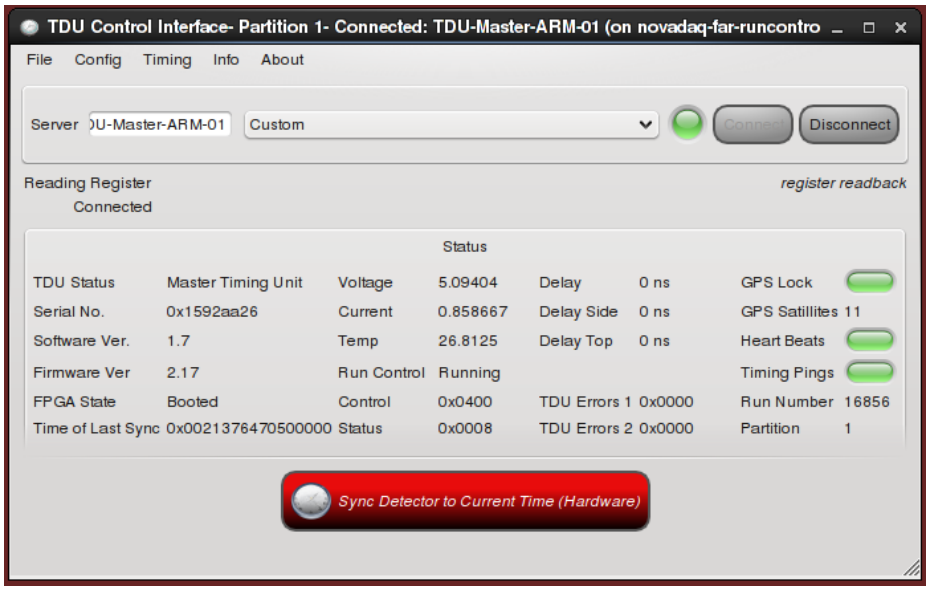

Figure 4.3: The TDU Control GUI, which interfaces with the NOνA timing system and issues GPS-based time syncs.

4.2.3 Run Control and Configuration

Runs are started, stopped, and paused by a Run Control server/client pair that keep track of the current state of the detector "partition" to which they are assigned (Figure 4.4). There can be up to four such "partitions" running on a given detector at the same time, using different parts of the detector. The DAQ Application Manager (Figure 4.5) tracks the current state of all of the DAQ applications, such as the DCMApplications, BNEVBs, Run Control itself, and all of the messaging infrastructure, and it reports this state information to Run Control. I have contributed code to the Run Control client and server to fix specific bugs, and am also responsible for several performance improvements to the DAQ Application Manager that were critical for running large partitions encompassing the entire detector and significant numbers of buffer nodes.

NOνADAQ uses a database to store configuration parameters, such as the defined streams for the DataLogger, settings for the ADCs on the FEB, and the threshold value for every channel in the detector. These thresholds are calculated by another program called the Pedestal Data Runner, which collects Digital Scanning Oscilloscope (DSO) data for each channel and uses this to calculate an appropriate threshold. DSO mode reads the current value of a given channel, a configurable number of times, typically several thousand times per channel.

4.2.4 Message Passing, Logging and Analysis

NOνADAQ uses a system called OpenSplice Data Distribution Service (DDS) to share messaging traffic between all of the components of the DAQ system. All DDS messages are seen by the Message Logger, as well as the source and destination groups. This segmentation is used to reduce the traffic seen by parts of the system that do not need to receive them (for instance, a DCM on diblock 02 does not need to see a message from a DCM on diblock 04). Run Control messages, exception messages from DAQ applications, and status notifications are all passed through this system. I

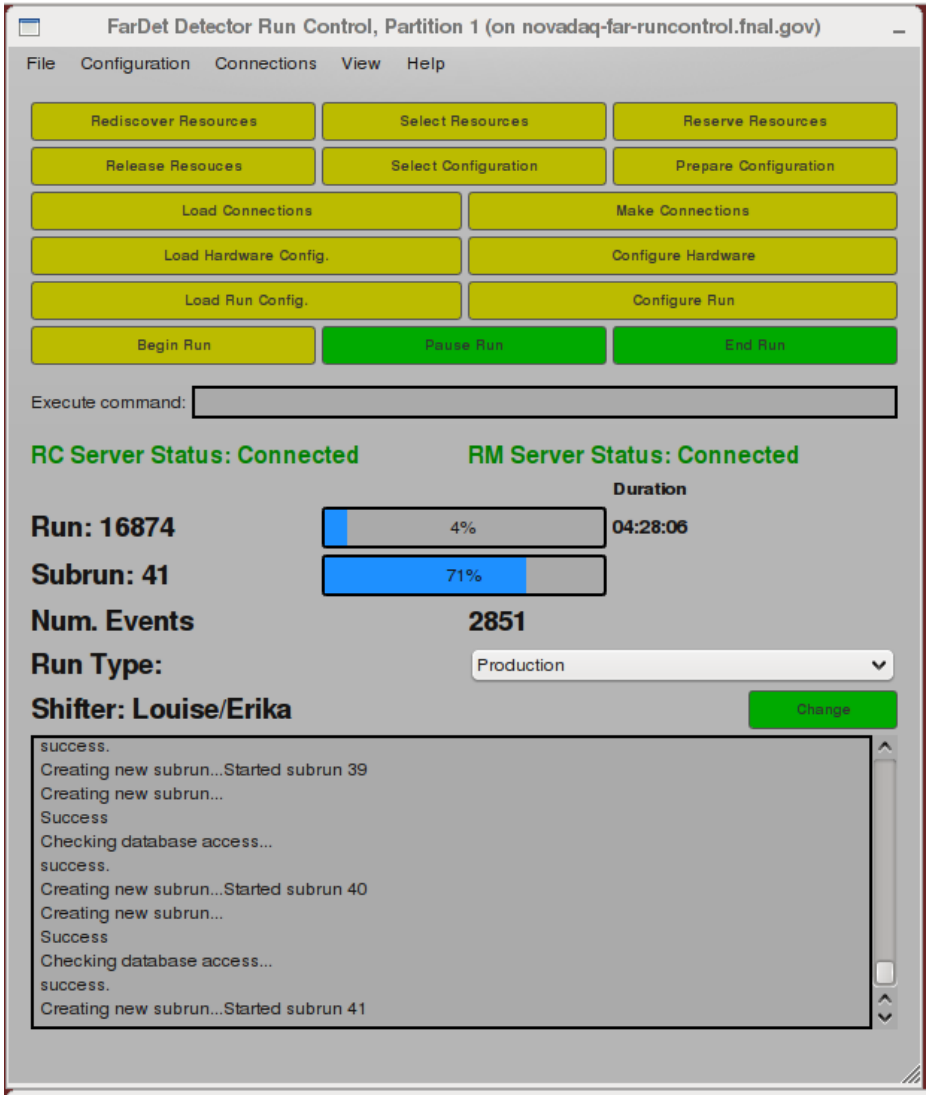

Figure 4.4: View of the Run Control client, from the Far Detector Partition 1, Run 16874

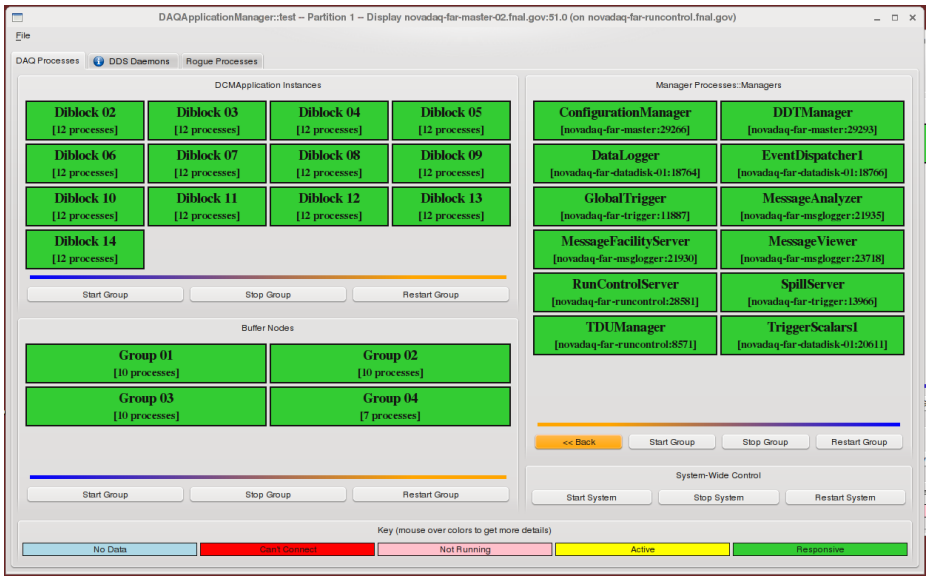

Figure 4.5: The DAQ Application Manager is responsible for keeping track of the state of all of the DAQ processes. Applications are broken down into diblock groups for the DCMs, and groups of 10 for the BNEVBs.

am also one of the only experts of note for the DDS configuration files, which control the segmentation, so when new message types were implemented, I ensured that they were properly directed to the appropriate receivers.

In addition to the message facility, which is monitored in real-time by a Message Viewer (Figure 4.6) and analyzed for easily-recoverable errors by the Message Analyzer (Figure 4.7), the output of each DAQ application is directed to log files located on an Network File System (NFS) mount from the Message Logger host. These log files are collected in a logical hierarchy and timestamped with the start time of the application, allowing for quick access if more in-depth troubleshooting is necessary.

The Message Analyzer runs on the Message Logger host, and it looks at each passing warning or error message to see if it matches a defined "rule" that would then define an associated corrective action. This is primarily useful for "out of sync" errors, where the Message Analyzer can direct the TDUControl (Figure 4.3) module to issue a detector time-sync. Run Control itself is also cognizant of a set of fatal errors, on

which it will display an error message on the control room desktops and end the run so the condition can be corrected.

4.2.5 Monitoring

The DAQ application "Event Dispatcher" sends information about each event over network sockets to the Online Monitor (OnMon) and the Event Display. These two packages are actually from NOνA Offline software (NOνASoft), but have been adapted for use in the DAQ system. The Event Display (Figure 4.8) is useful for verifying by eye that the detector is recording data correctly. It has also shown great utility in helping to detect synchronization issues between different DCMs. OnMon (Figure 4.9) collects statistics from each event, and provides for more long-term monitoring of the health of the system.

In addition to these monitoring packages, the Detector Control System (DCS) status is reported through the CSS GUI (CSS is a component of the EPICS DCS data collection system, Figure 4.10). This reports the status of each APD, whether it is cold, not being cooled, or in an alarm state.

4.3 Pedestal Data Runner

The Pedestal Data Runner (PDR) application is responsible for putting all of the FEBs into their DSO mode, taking data, and analyzing the result to determine the correct thresholds for each channel in the detector. One of the first tasks I carried out for the NOνADAQ group was to re-design the interface for the PDR (Figure 4.11). Later, I was asked to help improve the data collection methodology, and was able to improve the performance of the PDR from taking over an hour to complete a scan of the 14 diblocks of the Far Detector (FD) to just over 10 minutes.

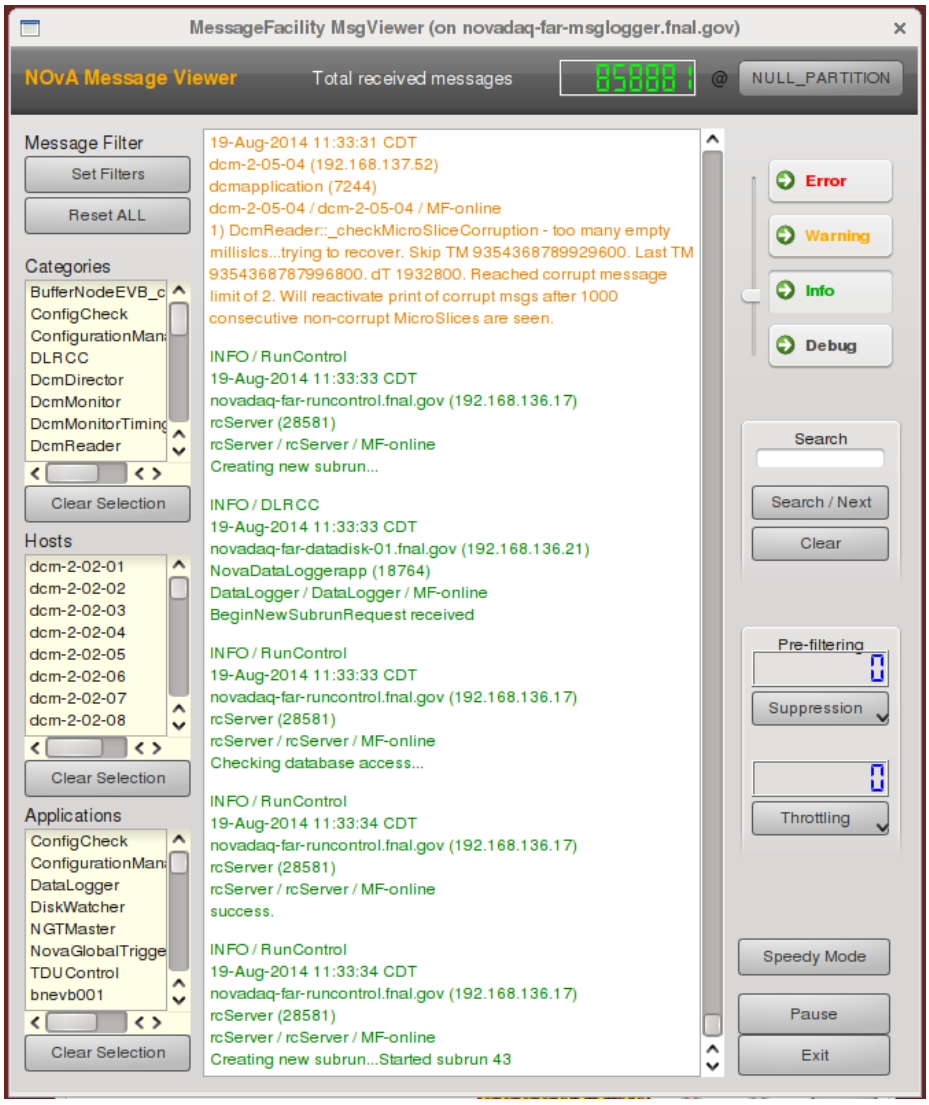

Figure 4.6: The Message Viewer allows for users to read the DDS messages which have been sent since the run began.

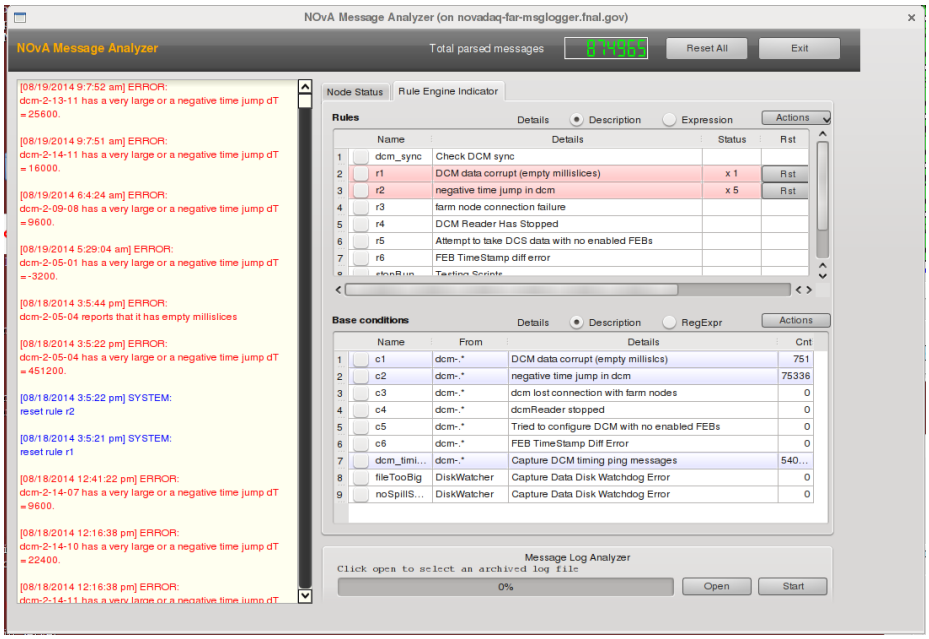

Figure 4.7: The Message Analyzer GUI, which reports error conditions seen and actions taken.

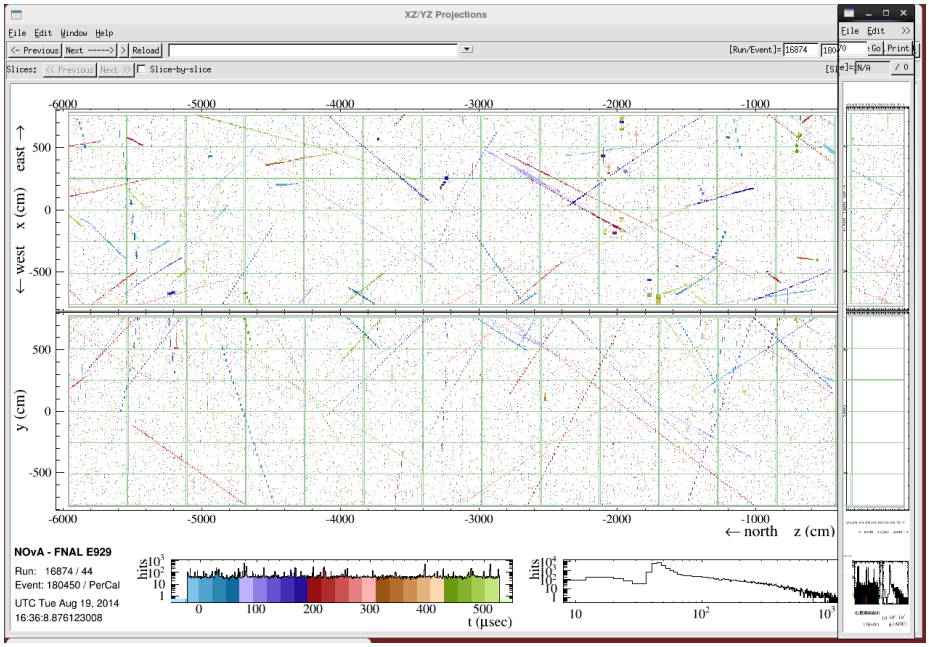

Figure 4.8: The NOνA Event Displays show two views of the detector, the XZ view is on the top (looking down from the top of the detector), and the YZ view is on the bottom (looking at the side of the detector). Hits are colored by the time within the event window and scaled slightly with repect to their ADC charge.

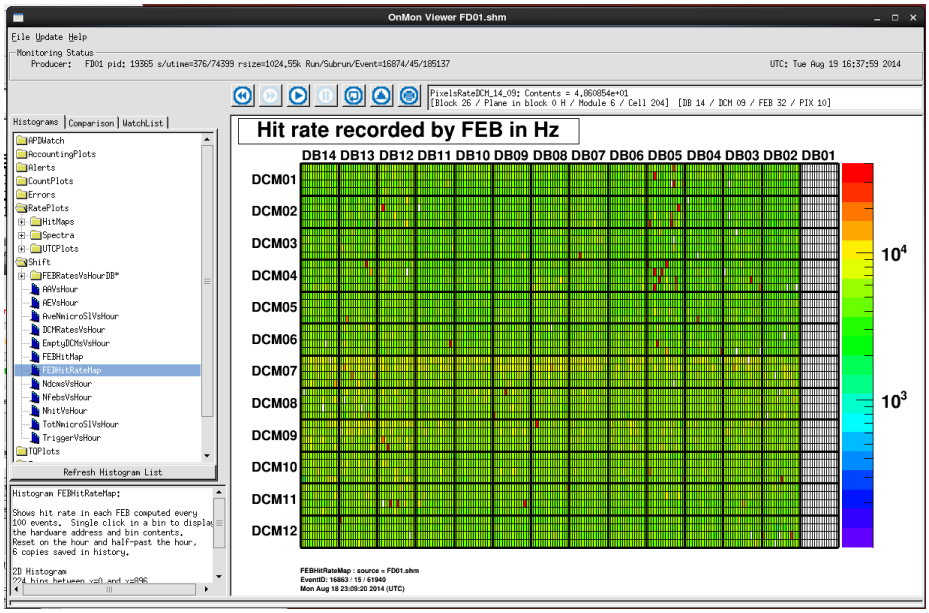

Figure 4.9: Online Monitor, which is used to show the performance of the DAQ systems over time. This OnMon is displaying hit rates in each channel, and it is apparent that the upper edge of the detector (DCM 7) is slightly more active than the rest, due to the lights above the detector.

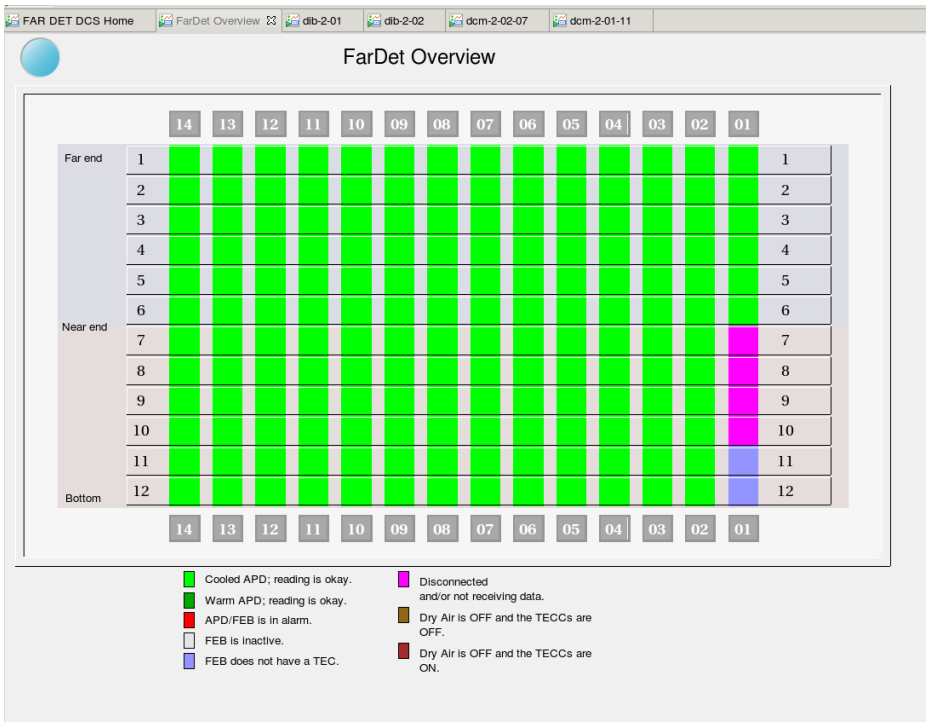

Figure 4.10: The DCS GUI displays summary data about the state of the FEBs in the detector, whether they are cooled, not cooled, or in alarm state.

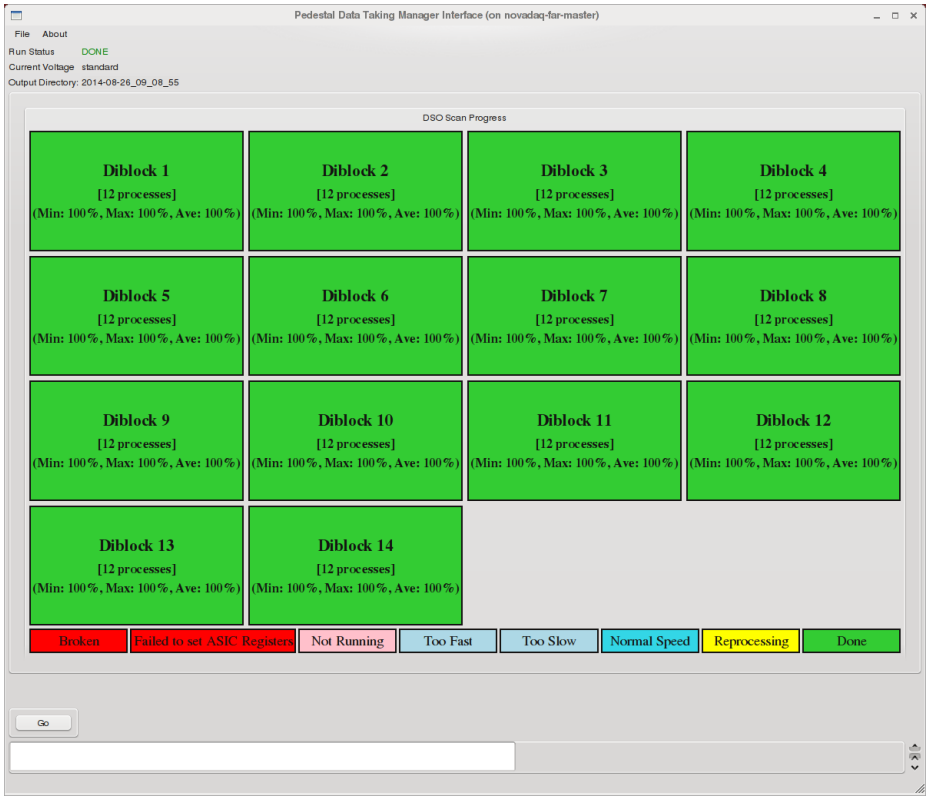

Figure 4.11: The redesigned PDR GUI, which shows the state of the pedestal run in a clear, easy-to-understand way. Each of the 14 diblocks can be clicked on to show detailed status for each of the 12 DCMs in that diblock.

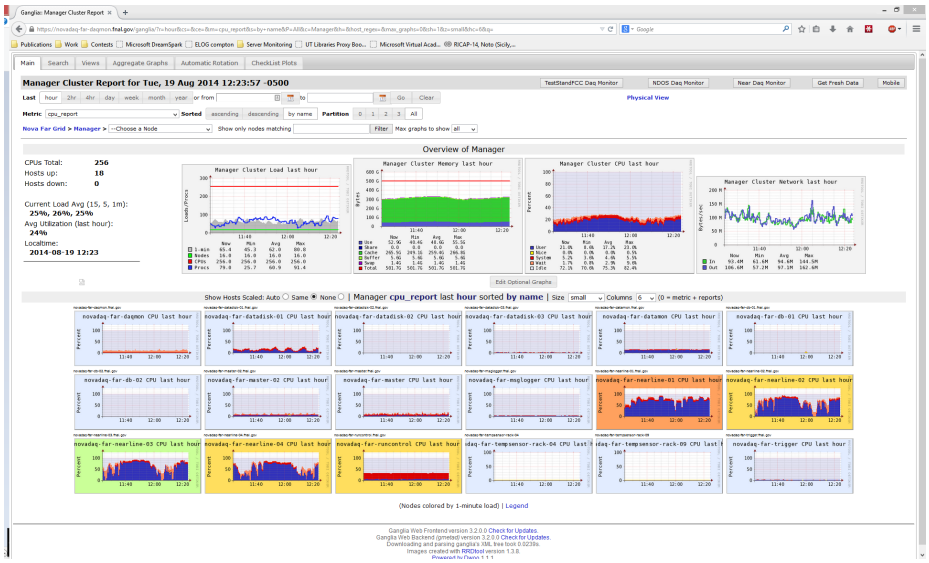

Figure 4.12: The Ganglia overview page for the Far Detector Manager nodes. Overall health statistics are shown, as well as one metric for each host in the group.

4.4 NOνA DAQ software Computing Clusters

The NOνADAQ software runs on a dedicated cluster for each detector. The Near Detector On Surface (NDOS) and ND detectors have their clusters at Fermi National Accelerator Laboratory (Fermilab), while the FD's cluster is in the ARCC, at the FD site. Each cluster is comprised of a number of buffer nodes and a set of manager nodes. Ganglia node monitoring is used to watch the health of all of the nodes in each cluster (Figure 4.12).

4.4.1 Near Detector On Surface Computing Cluster

The NDOS Computing Cluster (Figure 4.13) was the first full-scale installation of the NOνADAQ software. Created in 2010, it is now nearing end-of-life, meaning that the hardware components of the cluster are expected to start failing at a faster rate than it is practical to replace them. The NDOS cluster was originally comprised of 16 buffer nodes, two data disk hosts, and several manager nodes. One of the buffer nodes has been taken off-line on a semi-permanent basis due to a failing memory

module in the database master, deemed a more important resource. The NDOS cluster's primary node is called the master, which hosts all of the Virtual Network Computing (VNC) Control Room sessions, a DHCP server for the DCMs and Timing Distribution Units (TDUs) on the detector, NIS services to distribute user, group and host lookup information, NFS mounts of the DAQ software and user home directories, and a Trivial File Transfer Protocol (TFTP) server which the DCMs and TDUs use to retrieve their basic operating systems on startup. Other nodes in the cluster include runcontrol which runs the DAQ GUI applications (the GUIs are displayed on the master VNC sessions), trigger, hosting the Global Trigger and Spill Server, msgloggger, equipped with a large disk and handling all message logging traffic, and three nodes for the DCS group.

Working for the DAQ group as a computing specialist, I have taken over administration of the NDOS cluster. Part of this work has been performing maintenance on failing system disks and implementing protection strategies for the most important data on the cluster. To preserve the most critical configurations and DAQ software installations which are present on the master node, I have upgraded its system disk configuration to a software RAID-1. What this means is that there are two identical disks in the node, and the operating system keeps them synchronized so that they are exact mirrors of each other. If one disk fails, the OS will seamlessly begin reading from the other disk, and replacing the failed disk may be done without any data loss.

4.4.2 Far Detector Computing Cluster

Due to the large size of the FD, the Far Detector Computing Cluster (FDCC) is the largest cluster in the NOνADAQ system. It is comprised of 196 buffer nodes and a full suite of master nodes, eight DataLogger hosts, and eight DCS systems.

Due to the large size (1600 cores) of the NOνADAQ cluster at the FD, the NOνA Experiment has contracted with Fermilab Experiment Facilities, Scientific Server

Figure 4.13: The NDOS DAQ Cluster. The cluster takes up half of one computing rack. The ND cluster is similar in size, and the FD cluster is spread over 9 racks.

Support (FEF/SSS) to manage the computing environments. Their responsibility is to keep the FDCC in a stable configuration that supports the DAQ software. They manage all system-level updates, configuration, hardware maintenance, and are available for 24/7 troubleshooting. NOνA did the original configuration and installation of these nodes, and I was responsible for transitioning these unmanaged configurations to managed configurations under FEF/SSS's control.

The FD cluster represents Fermilab's first production use of Intelligent Platform Management Interface (IPMI) technology, and I have worked closely with FEF/SSS in devising stategies to fully take advantage of this technology. With IPMI, we no longer need separate console servers, as the interface supports Serial Over LAN (SOL) connections, even when the node is in a power-off state. We also use IPMI's ability to read out system sensor values and power cycle individual nodes. (See 4.5.)

4.4.3 Near Detector Computing Cluster

The ND cluster was the last commissioned cluster in the NOνADAQ system. I was primarily responsible for creating the DAQ installation for the ND, starting with a virtual partition of the NDOS cluster, and finally moving the then-established ND DAQ system from the NDOS cluster to the new ND cluster once it was installed in the Feynman Computing Center. I worked closely with FEF/SSS to get the ND cluster installed from a generic operating system installation, recording which operating system-level packages were necessary for the operation of the DAQ as we went. Because of this careful, iterative approach, FEF is confident that they can replace any given system in the ND DAQ cluster with a minimum of disruption to data-taking.

The ND computing cluster is comprised of 32 nodes, 8 chassis from the second FD computing purchase. It has two DataLogger hosts and 15 buffer nodes. Each node has 16 multi-threaded processor cores and 32 GB of RAM. There are also a standard set of manager nodes, as in the other DAQ clusters.

4.5 Load Shedding and Temperature Monitoring

4.5.1 Overview

Because the NOνA FD is at a remote location, there are moderately frequent power outages and cooling interruptions in the FDCC. On-call experts would take roughly 30 minutes to arrive on-site from International Falls, MN, but the computing load is such that the temperature can rise to a level where hardware starts shutting down well before then. To mitigate this, several temperature sensors have been installed which are monitored by scripts residing on the cluster. When these scripts detect a temperature rise, they cause a "load shed", shutting down computing resources to protect the hardware and reduce the load on the air handling in the FDCC.

4.5.2 Temperature Monitoring

We have installed two RoomAlert 4E environmental monitors in the FDCC, which monitor the current temperature inside two of the computing racks, as well as two sensors placed near the outlet and the inlet for the air handling system. These sensors can be read out with any granularity, but for monitoring purposes, they are checked every minute. Ganglia data archiving records the temperatures from these four sensors every time they are checked and adds them to the graphs which the collaborators serving in the control room are instructed to check on a regular basis for signs of emerging trouble (Figure 4.14). These sensors report the temperature in Fahrenheit multiplied by a factor of 100 in order to send four significant digits over Simple Network Management Protocol (SNMP) which, like the command-line shell itself, does not support decimal numbers. Their thresholds are set as "degrees over baseline", where the baselines are defined by the stable operating temperature of the sensors.

In addition to the dedicated environmental monitors, each node in the cluster has a temperature sensor on its Central Processing Unit (CPU). These are read

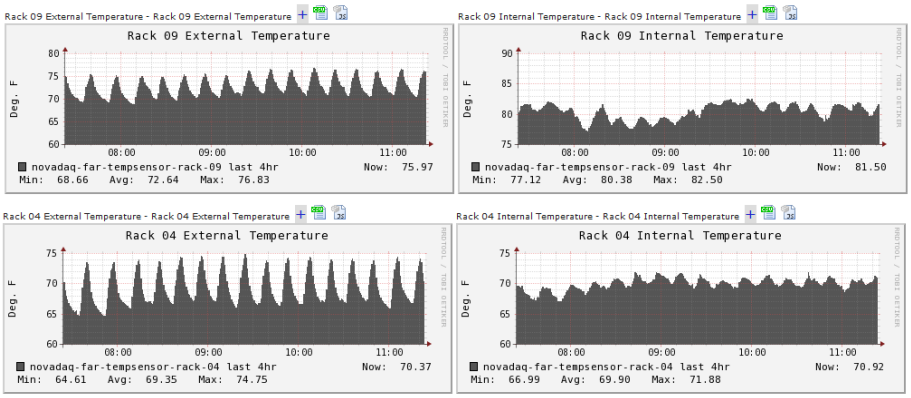

Figure 4.14: Ganglia plots displaying the temperature readout in the ARCC

out at 5 minute intervals, and archived in the Nagios monitoring tool every 10 minutes. Readout is effected by running the "sensors" command (from the lm_sensors UNIX package) over Secure Shell (SSH). All of the nodes in the cluster are read out simultaneously using a BASH Linux shell script. These sensors are read out in degrees Celsius, and have set thresholds based on a conservative estimate of hardware tolerance.

4.5.3 Load Shed Procedure

The main danger of over-temperature events rises from the fact that the first pieces of hardware to shut itself down are the routers and switches providing the network for the FDCC. Once this network is down, no further action can be taken to reduce the load on the air handling system, and the temperature will continue to rise until an expert arrives and intervenes manually. The load shed scripts have been set up in such a way that the entire DAQ cluster will have been shut down before the temperature reaches this critical threshold.

Because the FDCC nodes are equipped with IPMI interfaces, their power state can be controlled individually. This is a great advantage for our load-shedding scheme, as it means that we can shut down the cluster in stages, possibly keeping enough of the cluster active that the DAQ may still be run (though services such as DDT,

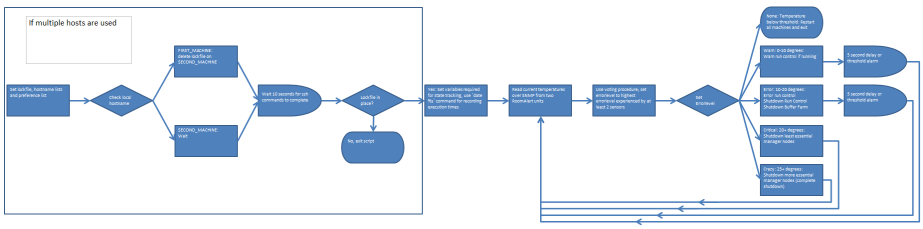

Figure 4.15: This flowchart details the logical path taken by the loadshed scripts. It first verifies which host it is running on and self-terminates if another instance is running elsewhere. It then enters a loop where it regularly checks the temperatures, and based on the pre-defined thresholds, it takes appropriate action.

which require the full cluster to be active, will be shut down). The first action of the load shed script it to warn the control room of an imminent temperature event, so that they can contact experts, the Ash River on-call expert first among them (Figure 4.15). It will then shut down half of the buffer nodes, which is usually enough to halt the temperature rise, unless the outside temperature is above roughly 70 degrees Fahrenheit. After waiting to see if this had the desired effect, the script will proceed to shut down the rest of the buffer nodes and finally it will start on the manager nodes.

When the temperature returns to normal levels, if the whole cluster was not shut down, then the script is able to turn on all of the machines that it turned off. Its final action is to declare an "all-clear" so that the detector's operators know that they can resume normal operation.

4.6 Other DAQ Expert Experience

4.6.1 DAQ Software Management

I was asked to help keep the version of the DAQ software operating on the detectors up-to-date. This meant establishing a "tag" or static version of the DAQ software, validating it on the NDOS detector, then installing this tag on the FD and ND. This is a very complex and time-consuming process as the software needs to be built

separately for the x86_64 Linux processors in the computing cluster and the ARM PowerPC processors in the DCMs and TDUs. Additionally, my status as a general expert allowed me to make sure that all of the DAQ applications' latest versions compiled and ran correctly before deploying a tagged version of the software.

Chapter 5

Compton Spectrometer Experiment

5.1 Introduction

Liquid Scintillators (LSs) such as those used in the NuMI Off-Axis ν_e Appearance (NOνA) Experiment [26] suffer from quenching of the signal and Cherenkov re-emission effects [28]. The quenching follows an empirical relationship first characterized by Birks (Equation 5.1 [19]), and is proportional to $\frac{dE}{dx}$. While Birks' quenching tends to reduce the light seen for a given particle in the detector, Cherenkov re-emission has the opposite effect, increasing it. The Cherenkov light is absorbed by the fluors in the scintillator and re-emitted in the absorption range of the wavelength-shifting (WLS) fibers used in the NOνA cells. A series of experiments have been performed in order to precisely measure the response versus energy curve for the NOνA LS and the Cherenkov re-emission properties of the NOνA LS. These measurements were then integrated into the NOνA calibration algorithms, allowing for the energy of electromagnetic showers to be properly estimated using the muonic in-situ energy calibration. NOνA does not use calibration sources, as it has large amounts of cosmic exposure, providing Minimum Ionizing Particle (MIP) hits in

every cell in relatively short amounts of time.

$$L = L_0 * \frac{\frac{dE}{dx}}{1 + k_B \frac{dE}{dx}} \tag{5.1}$$

5.2 Theory

Cherenkov light is produced by a particle traveling faster than the local speed of light. Cherenkov light is produced in a cone whose opening angle is determined by the particle's velocity and the optical properties of the medium (Equation 5.2). (For a detailed theoretical treatment, see [20].)

$$cos\theta_C = \frac{1}{n\beta} \tag{5.2}$$

We see from this equation that Cherenkov light emission only occurs for wavelengths where βn is greater than 1 (n itself is a function of λ). The number of Cherenkov photons produced is proportional to the velocity of the particle and the optical properties of the material, and is given by Equation 5.3.

$$dN = \int_0^{\lambda max} \left[\frac{2\pi\alpha z^2}{\lambda^2} \left(1 - \frac{1}{\beta^2 n^2(\lambda)} \right) d\lambda \right] dx \tag{5.3}$$

Where z is the charge of the particle and α is the fine structure constant, equal to $\frac{1}{137}$. As the number of photons is proportional to $1/\lambda^2$, Cherenkov photons are heavily weighted towards the UV end of the visible spectrum. Since most scintillators produce scintillation photons in the same range, light collectors for scintillators (Photo-Multiplier Tubes (PMTs) and Avalanche Photodiodes (APDs)) are also sensitive to Cherenkov light. In NOνA's case, Cherenkov photons, whether primary photons from the particle itself, or re-emitted photons (photons which are absorbed by the scintillator and subsequently re-emitted at the scintillator's wavelength) may be absorbed by the WLS fibers and transmitted to the APD.

The quenching of the signal is due to the molecules in the scintillator reaching maximum excitation. Additional ionizing radiation starts to break down the scintillating components at this point, and no additional light is produced [19]. These effects are significantly different for muons (which have much lower $\frac{dE}{dx}$, Figure 5.1), and the Compton spectrometer measurement allows for the translation of NOνA's in-situ calibration efforts to absolute scale compatible with precision measurements of electron neutrino energy with the NOνA detectors, through the reconstruction of electromagnetic showers. While Birks' constants have been measured for several different scintillators (for example, in [29]), NOνA's unique formulation combined with the need for precise determination of electromagnetic shower energies requires an independent measurement for the NOνA LS. The light output of the scintillator, given by Equation 5.4, is proportional to the Cherenkov light plus the scintillation light from the energy deposited in the scintillator, corrected by Birks' formula ($f(R, N_{Cherenkov})$ denotes the UV re-emission of the scintillator, and is an empirically-measured quantity).

$$L_{total} = L_{Birks} + f(R, N_{Cherenkov}) \tag{5.4}$$

5.3 Compton Measurement

5.3.1 Overview

The Compton dpectrometer is a device used to test the response of a detector to electrons of known energy [30], providing precision measurements of detector nonlinearity. This is accomplished using a highly collimated ^{22}Na source and a coincidence detector that can be rotated about the center of the test detector (Figure 5.2). Requiring coincidence "selects" an electron energy in the test detector determined by the initial gamma energy (for ^{22}Na, either 511 keV or 1275 keV) and

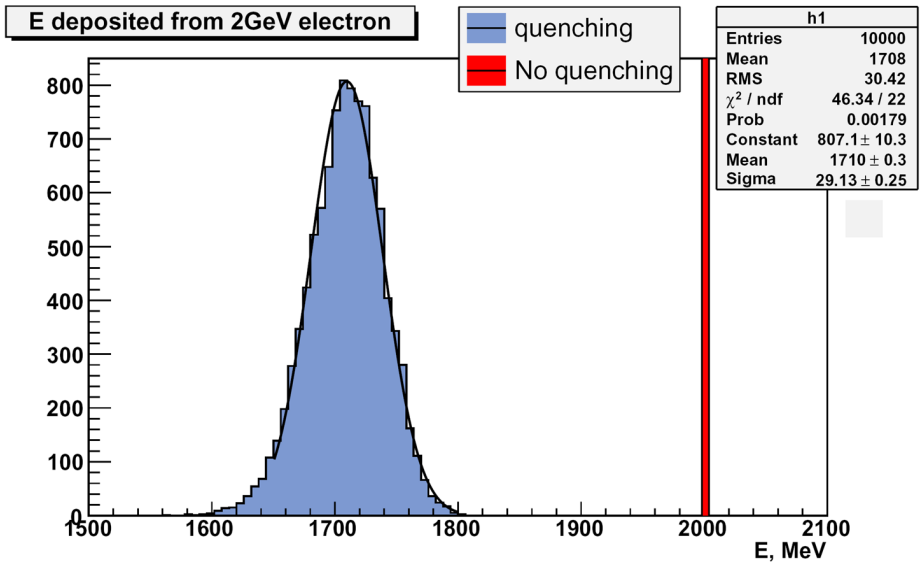

Figure 5.1: Effect of quenching in KamLAND scintillator. Muons have much lower $\frac{dE}{dx}$, and therefore do not cause the quenching effects in the same way that electrons do.

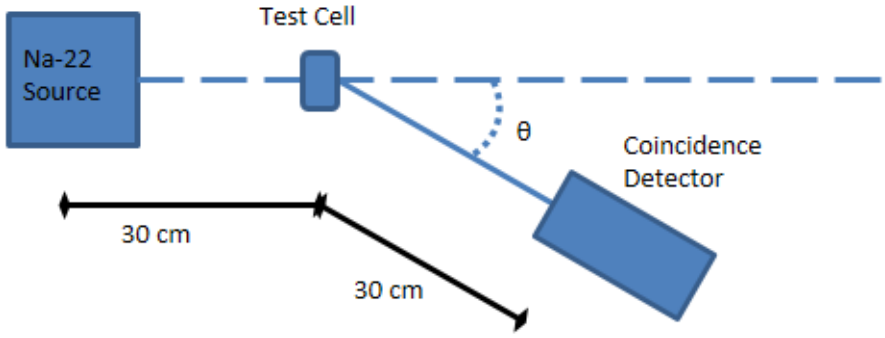

Figure 5.2: Schematic diagram of the Compton Spectrometer experiment

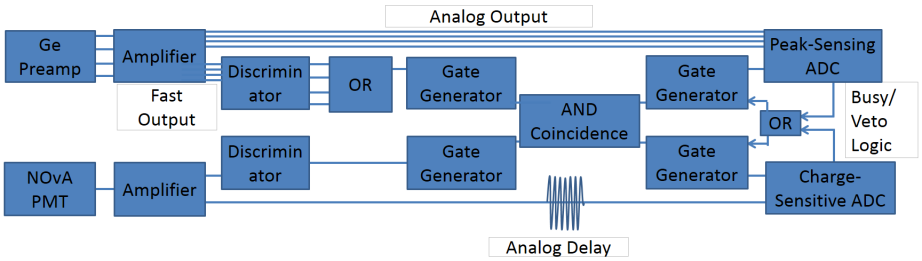

Figure 5.3: The Compton Spectrometer's hardware DAQ logic

the angle between the beam-line and the coincidence detector (Eqn. 5.5).

$$E_{e-}^{kinetic} = \frac{E_\gamma^2(1 - cos\,\theta)}{m_e c^2 + E_\gamma(1 - cos\,\theta)} \tag{5.5}$$

5.3.2 Upgrades

The Compton spectrometer was first run at University of Tennessee (UT) for the KamLAND experiment [28] and has since been upgraded with a High-Purity Germanium (HPGe) detector in place of a NaI scintillator as the coincidence detector. The much higher resolution of the HPGe detector allows for the experiment to be run without precise measurement of the scattering angle, allowing for runs to be taken more quickly and efficiently. Because of the different properties of semiconductor detectors, the Data Acquisition (DAQ) chain for the coincidence detector had to be separated from the test detector (Figure 5.3), and software logic put into place to synchronize the two Analog-to-Digital Converter (ADC) units.

As part of these upgrades, the LabVIEW-based DAQ system for the experiment was entirely re-written and multiple characterization measurements of the entire system were taken.

5.3.3 Compton DAQ Hardware Logic

The signal from the germanium coincidence detector passes through a spectroscopic amplifier, which has a fast timing output and an amplified signal output. The amplified signal output goes to a Peak-Sensing ADC (PADC), while the timing output

is run through a discriminator, OR coincidence (the germanium detector is made up of four crystals which each produce a separate signal), a gate generator, and finally the AND coincidence with the scintillator signal. The signal from the scintillator in the test cell, meanwhile, passes through a fixed-gain amplifier, the discriminator, another gate generator and the AND coincidence. The outputs from the AND coincidence are sent to another set of gate generators for ADC gate timing, and then the ADC units themselves. The scintillator signal from the amplifier is also passed through a long delay cable to a Charge-sensitive ADC (QDC). Both ADC units are read-out through VME and a VME to USB bridge.

In order to suppress high counting rates when the system is operated without the AND coincidence, a negative feedback loop was introduced. The BUSY output of both ADCs is put through OR coincidence and then passed to the inhibit input of the ADC gate generators. This ensures that no gates are produced while the units are busy, which in turn ensures that the gate counters on the PADC and QDC remain synchronized. This is important because the internal gate counters are used to pair the events in the LabVIEW DAQ system after being read asynchronously from the ADC units.

As a consequence of this dual DAQ chain, extreme care had to be taken to understand the relative timing of the two detectors, and several gate generators were introduced in order to delay the logic pulses so that they line up in a single coincidence gate, with cable delays for the actual signals from the detectors to maintain the ADC gates (Figure 5.4). This issue is compounded by the fact that the two signals occupy entirely different timing regimes, with the PADC signal occurring over several μs, and the QDC signal tens of nanoseconds.

5.3.4 LabVIEW DAQ

Each of the ADC units has a multi-event buffer on board, and this buffer can be read out asynchronously over the VME bus. The LabVIEW-based DAQ system was

(a) Histogram of the Ge gate locations relative to the scintillator gate (scale is 2 μs)

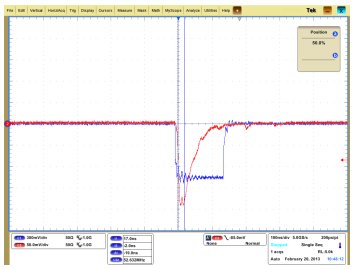

(b) Scintillator signal in the QDC gate (scale is 50 mV by 100 ns)

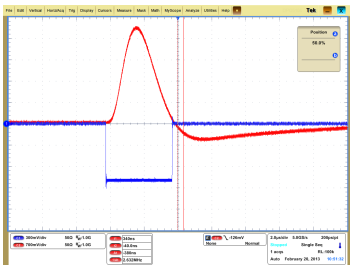

(c) Ge signal in the PADC gate (scale is 700 mV by 2 μs)

Figure 5.4: Oscilloscope traces showing the relative timing of the Compton DAQ system

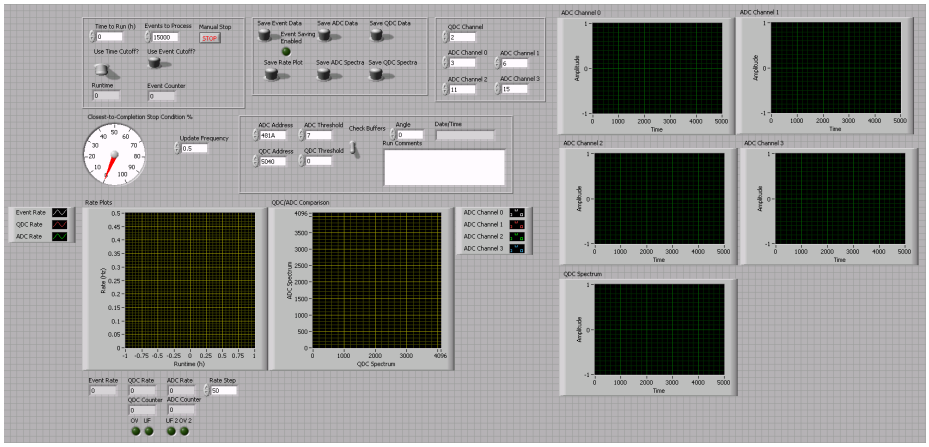

Figure 5.5: Compton LabVIEW DAQ Software Front Panel

designed to read out these buffers and pair together events based on the internal gate counter present in both ADC units. The Graphical User Interface (GUI) allows the user to select the duration of a run in either event count or time (or both), configure the thresholds for the ADCs, and monitor the progress of the run using several graphical displays of the current event rate and the PADC vs. QDC of each event (Figure 5.5).

Because VME communicates with LabVIEW through a serial connection, the LabVIEW software has to decode the data stream to obtain the actual ADC-converted values. Each unit reports all of the channels' values during the gate pulse, so for the

PADC each event consists of 32 ADC values, and the QDC has 16. Part of the user input to the software is the 4 PADC channels and one QDC channel that should be saved to disk, corresponding to the four Ge crystals and the one scintillator PMT. The software maintains an event buffer and builds events when both ADCs have reported them.

The LabVIEW package also serves as a run control interface and DAQ monitoring system. It creates histograms of the spectra from the Compton detectors and plots each QDC data point versus one of the PADC channels in the same manner as the offline analysis. It also makes plots of event rates, obtained by dividing the number of events received from the VME ADCs by the time elapsed since the last buffer read for that ADC.

5.3.5 Data Files and Analysis

The LabVIEW DAQ saves several text files for each run. An event summary file contains all the user parameters of the run, then separate text files are created for the PADC and the QDC's recorded events and their spectra. The event rate plots are also saved in their own text file. Finally, the combined events are saved, with event counters and all 48 channels of readout. A ROOT macro reads these files into TTrees for easy analysis, and creates several histograms that are of interest to the primary analysis. The Geant4 model has also been configured to write its data files in the same format, so that a single analysis package can be run over both data and Monte Carlo simulations.

Because Compton scattering can be approximated as an elastic scattering event, we know that the energy of the recoil electron in the scintillator is simply the initial gamma energy minus the final energy we measure in the coincidence detector. Because the germanium detector has a very high spectral resolution, we can determine the electron's "true" energy with very high precision. Therefore, for each energy level from the ^{22}Na source, a new histogram can be created relating "true" energy to "observed"

energy, based on a calibration of the scintillator performed with gamma sources. The nonlinear effects are then simply read off of this graph, as the full energy of the photon will create a "spot" on the output plot of expected electron energy versus measured electron energy (due to Compton scattering events in the germanium detector, there will be a "triangle" shape in the output spectrum, but only the full-energy spot is of interest). The Cherenkov re-emission effects cause a deviation to higher observed energy at low true energy.

5.4 Geant4 Model

The experiment was simulated using Geant4 (Figure 5.6). This simulation is used in conjunction with the results of a UV monochromator experiment that was performed by Philip Mason at UT, following a similar procedure as described in [28], to determine Birk's quenching constant and UV re-emission coefficient in the NOνA scintillator. The UV monochromator experiment sent UV photons with precisely-defined wavelengths to a miniature NOνA cell, complete with WLS fibers. The fibers were read out and the re-emission coefficient (integrated with the WLS absorption probability) was determined. The full experiment is simulated in the Monte Carlo code, and the Birks' coefficient in the simulation is adjusted to match the data. As in neutrino experiments like NOνA, the Monte Carlo simulation informs the data analysis, in this case explaining a feature present in the data. Early versions of the Geant4 simulation used the Cherenkov re-emission and Birks coefficients found for the KamLAND scintillator, as they have similar composition.

The model is primarily used to measure the Birks coefficient by combining the results of the UV-monochromator experiment with those of the Compton spectrometer experiment. The UV-monochromator constrains the "positive", or overestimating, nonlinearity effects, and Birks quenching accounts for the remainder.

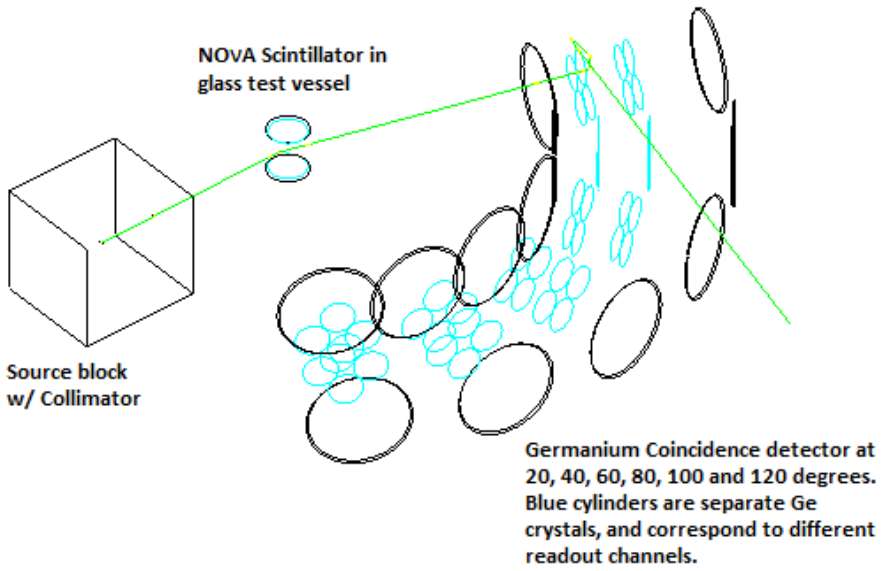

Figure 5.6: Geant4 Rendering of model geometery. The Ge detector is replicated to occupy all of the angular positions used in the experiment.

5.4.1 Implementation Details for Cherenkov Simulation in the Compton Spectrometer Geant4 Model

In order to properly simulate the Cherenkov re-emission in the detector, a custom "Sensitive Detector" class was created which records the energy deposition during some microscopic step through the scintillator. This energy is then converted into a scintillation photon count. Similarly, the average energy of the particle during the step, as well as the step length, are used as inputs to a Cherenkov simulation which uses the measured re-emission coefficients and the calculated index of refraction for the scintillator to estimate the number of Cherenkov photons created during the step. The two photon counts are combined and an efficiency applied to achieve the resultant signal pulse, which is then converted into an observed energy. The "true" energy of the step is also recorded. The energy reported by the detector for the event is the sum of all such steps occurring within the detector volume during that event.

The Cherenkov simulation performs a Riemann sum over ultraviolet wavelengths for which the refractive index, n, has been calculated and the re-emission coefficient

has been measured. The simulation provides the length and velocity of the track in the detector, allowing for the number of Cherenkov photons to be calculated via Equation 5.3.

5.4.2 Determining Ge Crystal Dimensions for Geant4 Model

One of the main difficulties encountered in creating the Geant4 model was the absence of an accurate drawing of the interior of the gfermanium detector used as the coincidence detector in the experiment. The detector has four separate crystals inside the single enclosure. When I contacted the manufacturer, Ortec, they stated that the detector in question was old enough that they no longer had the model drawings, and as each germanium crystal is unique, they could not give me precise measurements for the crystals.

To resolve this issue, I decided to try an "x-ray" procedure, but using a ^{137}Cs source at 162 keV instead of a traditional x-ray source. I had fabricated a 4 cm lead collimator to direct the radiation from the source into a tight, 1 mm diameter beam. The face of our detector was then equipped with a grid of points and a series of counting measurements were conducted to make a "heat map" corresponding to the physical dimensions of the crystals. This procedure was repeated along the side of the detector, giving a 3-d representation of the crystals inside the enclosure.

5.5 Results and Analysis

The Compton Spectrometer was run once through the full angular spectrum (20-120 degrees). The data from the LabVIEW DAQ were run through ROOT analysis scripts (Figure 5.8), and this result forms the initial sample for refining analysis techniques and as a sanity check of the Geant4 model. The primary features we expected to see are the triangle-shaped area denoting the full visible energy of the photon, and a deviation to high reconstructed energy for higher true energies, due to the Cherenkov

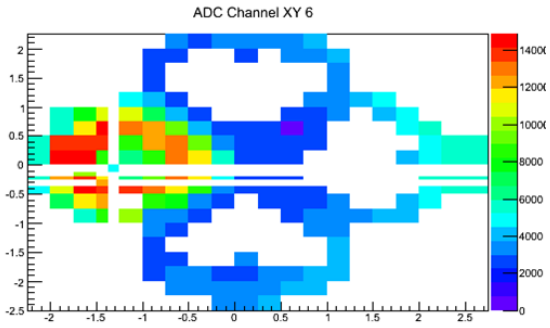

(a) Heat Map from measurements of the Ge detector, as seen by one crystal. Significant self-shielding effects are apparent in the center of the crystal. Scales are in inches.

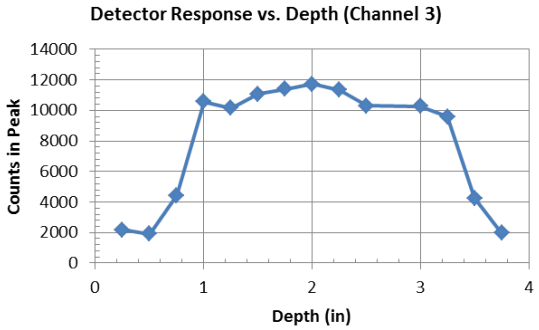

(b) Counts as a function of the distance from the face of the detector enclosure. The crystals start at a depth of 2.5 cm and are 5.5 cm deep.

Figure 5.7: Compton Coincidence Detector Maps

re-emission. After this initial run, the system was subjected to intense scrutiny, due to the absence of appreciable signal from the 511 keV line. Eventually, however, these issues were resolved through adding filters to the germanium outputs, adjusting the high voltage and thresholds for the scintillator, and verifying the timing of the system, and another run was performed over the full angular range.

For the second run, calibration runs for both the germanium coincidence detector and the NOνA liquid scintillator were taken before each data point to ensure there was no "drift" in either detector. The calibration-mode QDC spectrum (Figure 5.9) was examined for the presence of two Compton edges, and to make sure that the relative positions of these edges had not shifted. The germanium calibration spectra (Figure 5.10) were used to calibrate the detector at 0 degree angle (511 keV and 1275 keV peaks are clearly visible), and verify that the detector was performing adequately and that its response was linear.

Each of the three active germanium crystals was analyzed separately, as each is at a different angle relative to the collimated Na-22 beam. The model was set-up to mimic this behavior, and to produce results from a single angle at a time instead of the full angular spectrum. For example, Figure 5.11 shows both the model and real data output for the Compton spectrometer when the germanium detector is at 40

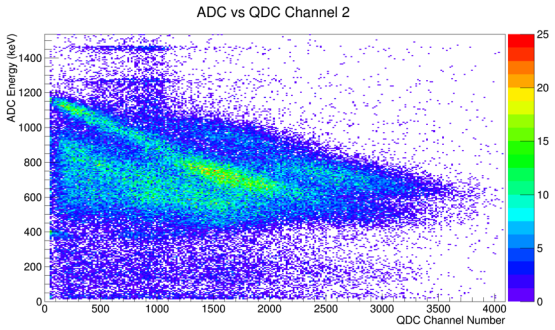

(a) Calibrated data, with the QDC on the horizontal axis and the PADC on the vertical.

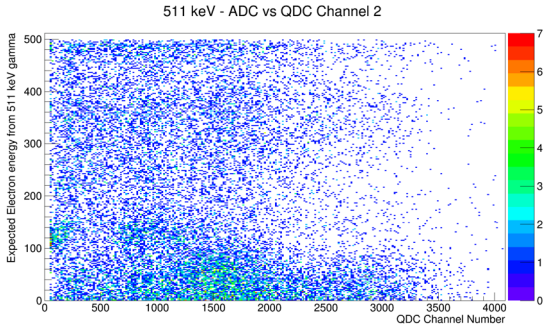

(b) Expected energy (from the PADC, assuming 511 keV line) versus reconstructed energy.

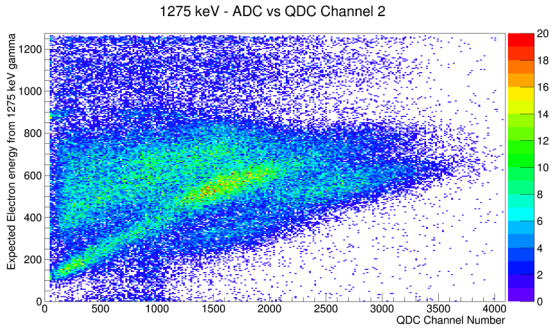

(c) Expected energy (from the PADC, assuming 1275 keV line) versus reconstructed energy.

Figure 5.8: Results from the integration run of the Compton Spectrometer. Features of note are the triangle shape from the full energy of the initial photons, and the area inside that shape is from multiple scattering. Note the lack of consistent data in the 511 keV case and the presence of data "outside" the triangle, which are indicative of the issues with the integration run.

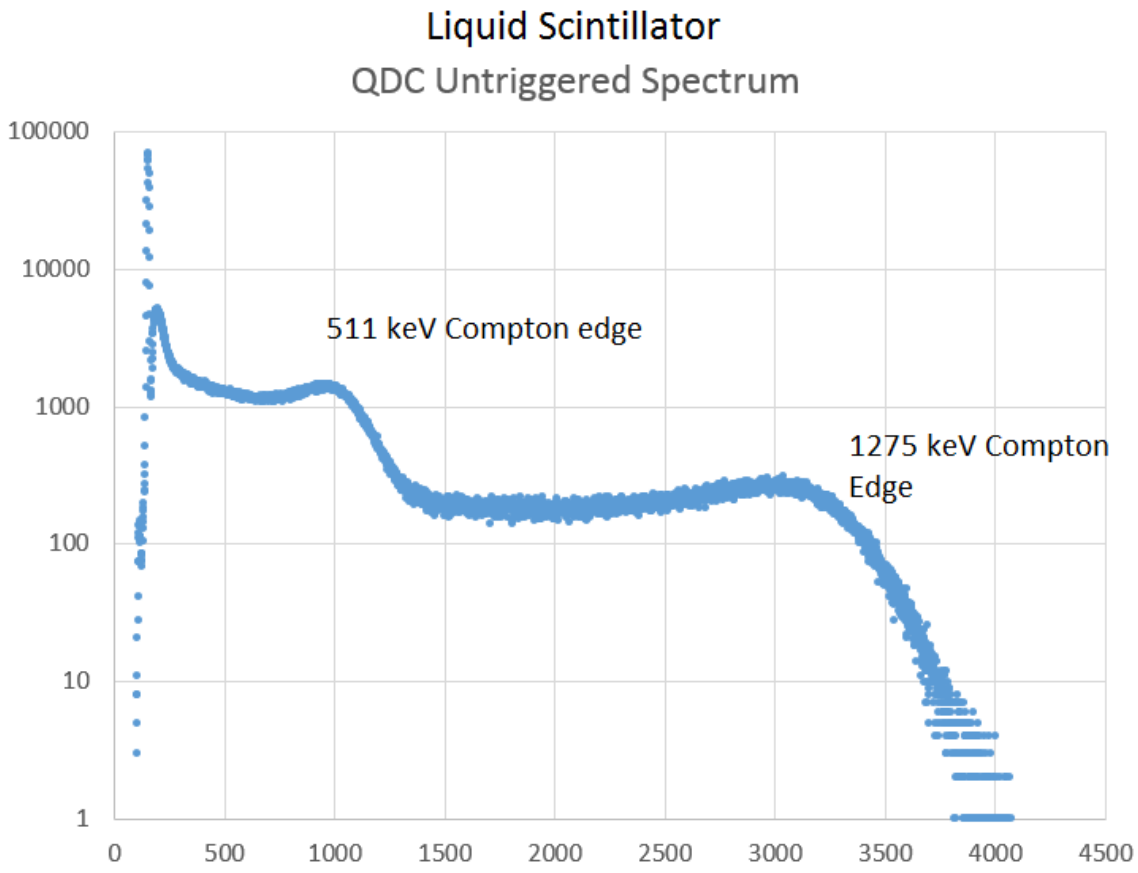

Figure 5.9: QDC Spectrum, untriggered calibration run. The detector's pedestal peak is visible at approximately channel 65, with two Compton edges at approximately channel 1000 and channel 3300. The scintillator is responding to both photons from the source, and the Compton spectrum is well-formed. As this is a small organic scintillator, there are no photo-absorption peaks.

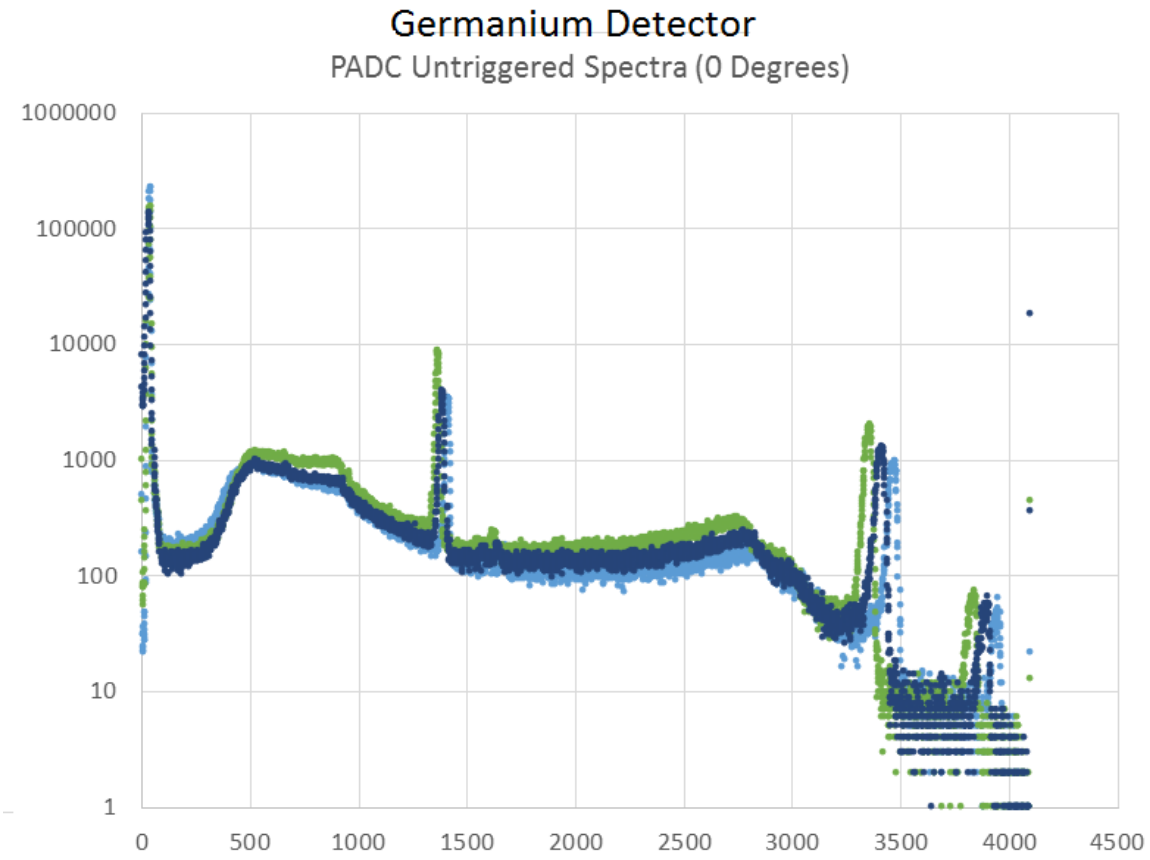

Figure 5.10: PADC Spectrum, untriggered calibration run, 0 degree angle. For each of the three crystals, it is possible to see the pedestal, the 511 keV peak, and the 1275 keV peak. The higher-energy peak is most likely K-40 background.

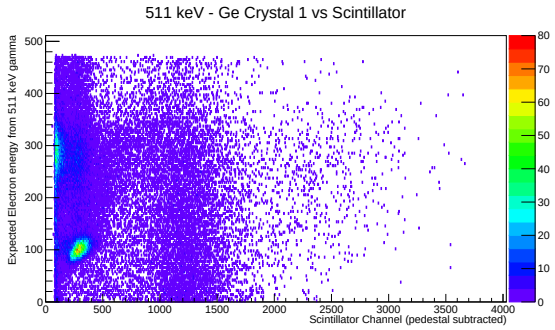

(a) Compton spectrometer, 40 Degrees, 511 keV plot (crystal 1)

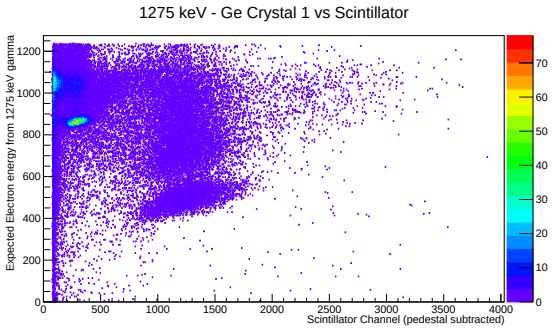

(b) Compton spectrometer, 40 Degrees, 1275 keV plot (crystal 1)

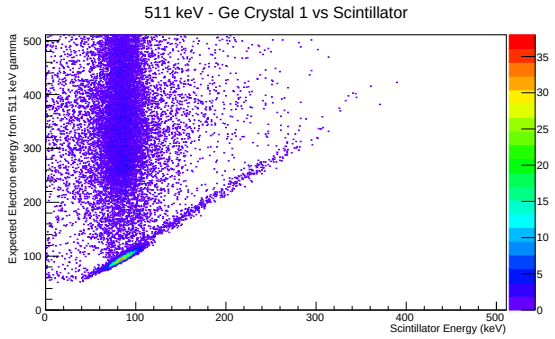

(c) Compton Geant4 Model, 40 Degrees, 511 keV plot (crystal 1)

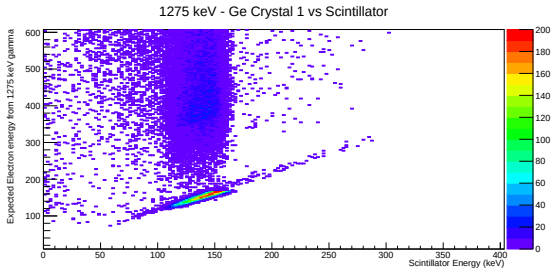

(d) Compton Geant4 Model, 40 Degrees, 1275 keV plot (crystal 1)

Figure 5.11: Data and Monte Carlo of the QDC versus germanium crystal 1 when the coincidence detector is at 40 degrees.

degrees. Similarly, Figure 5.12 shows what the QDC vs. PADC plot looks like when the germanium detector is at 100 degrees.

These results were analyzed by projecting horizontal "slices" representing predicted energy from the germanium detector onto the QDC axis and applying a Gaussian fit. The normal distribution allows for the determination of not only the mean value, but also the error of the mean. These results were then plotted as a function of germanium energy in Figure 5.13. This analysis was performed by undergraduate student Cameron Erickson.

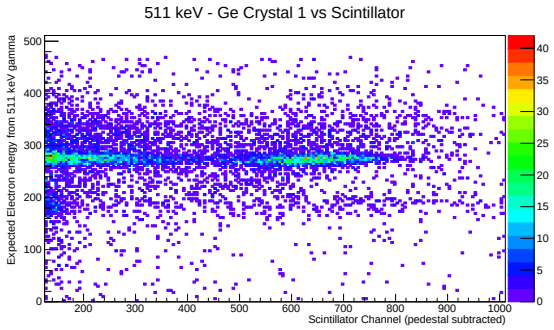

(a) Compton spectrometer, 100 Degrees, 511 keV plot (crystal 1)

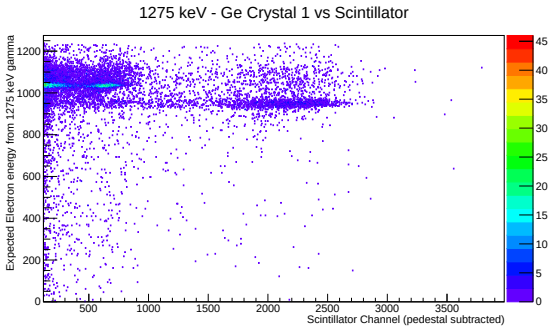

(b) Compton spectrometer, 100 Degrees, 1275 keV plot (crystal 1)

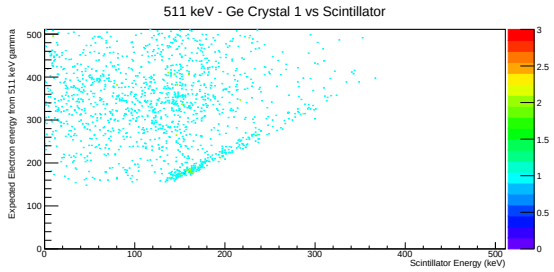

(c) Compton Geant4 Model, 100 Degrees, 511 keV plot (crystal 1)

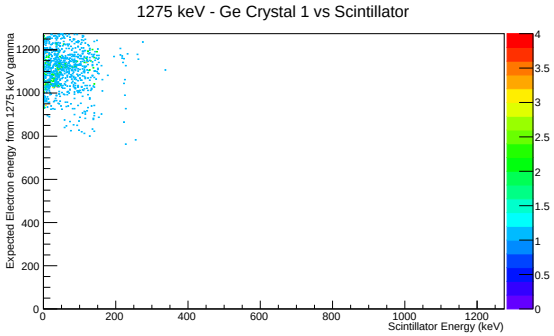

(d) Compton Geant4 Model, 100 Degrees, 1275 keV plot (crystal 1)

Figure 5.12: Data and Monte Carlo of the QDC versus germanium crystal 1 when the coincidence detector is at 100 degrees.

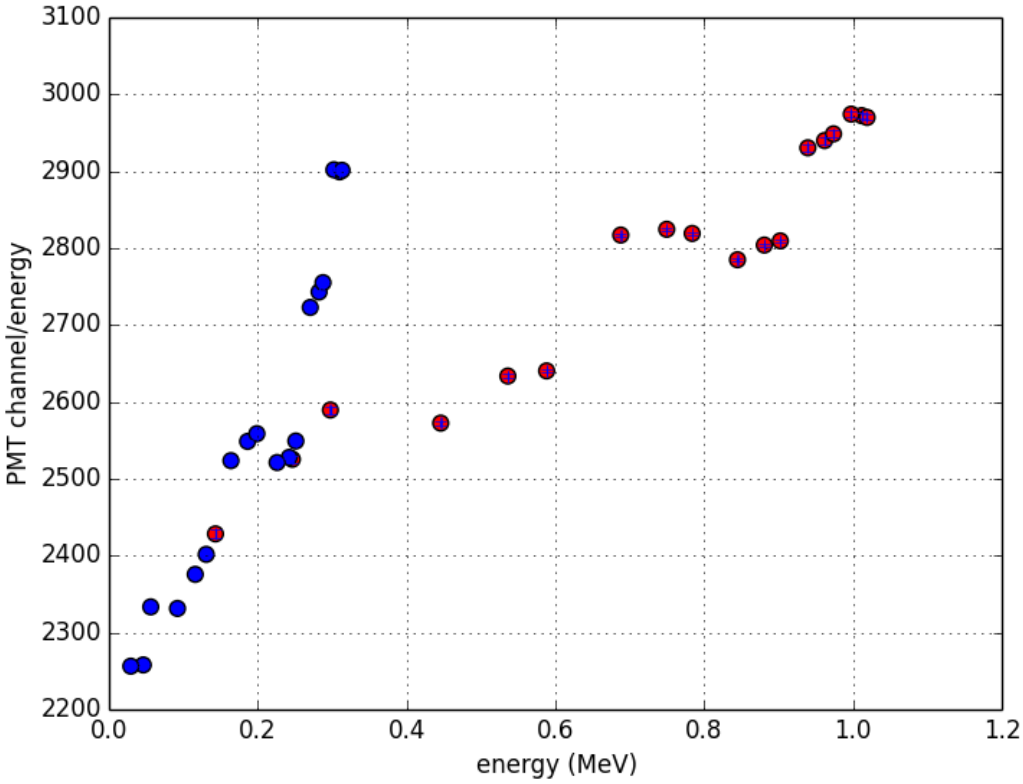

Figure 5.13: Result of the analysis of the Compton Spectrometer Error bars are the same size as the plot markers. Different colors correspond to different Germanium crystals. This plot may be used to calibrate the NOνA scintillator, and the model result will show what value of Birks' constant this calibration corresponds to.

Chapter 6

Background Evaluation

6.1 Introduction

As with every particle physics experiment, backgrounds from cosmic sources which could potentially be accepted as neutrino signals should be minimized. The most common method for neutrino experiments to minimize backgrounds is to locate the experiment under a large amount of shielding material, "overburden", and to incorporate active cosmic-ray veto systems into the detector design. NuMI Off-Axis ν_e Appearance (NOνA) has the advantage of being an accelerator neutrino experiment with a very well-defined beam pulse interval. NOνA does not use a cosmic-ray veto, due to both cost considerations and because the detector's segmentation allows for in-situ cosmic identification and rejection. Because the Far Detector (FD) has relatively low overburden (Table 6.1), however, there is a chance for backgrounds to become relevant in the experiment. The potential backgrounds include unwanted neutrinos from beam or non-beam sources interacting in the detector during a trigger window ("true" background), and any combination of events in the detector that mimics a neutrino signal ("accidental" background). The NOνA neutrino search tools were run over the "cosmic" dataset from the First Analysis run, using the tuned parameters used in the actual analysis. The cosmic dataset contains the periodic random triggers,

and a time-based filter ensured that no beam spills were anywhere near the triggers in the file. This work identifies both "true" non-beam backgrounds and any cosmic-induced "accidental" backgrounds. The same analysis was run over the Monte Carlo simulation files for electron neutrino (ν_e) and muon neutrino (ν_μ), and purity and efficiency metrics calculated for each of the ν_e and ν_μ analysis groups' search tools (Section 6.2).

Table 6.1: Overburdens of various neutrino detectors

Detector Name	**Overburden (m.w.e.)**
Sudbury Neutrino Observatory (SNO) [3]	6010
Homestake Detector [12]	4200
KamLAND [1]	∼2700
MINOS Far [23]	∼1900
Daya Bay [6] EH1	250
EH2	265
EH3	860
CHOOZ [8] (Double Chooz Far Site)	300
MINOS Near [23]	
NOνA Near	∼265
Cowan-Reines [7]	∼32
NOνA FD	**3.2**

6.2 Analysis Methodology

Primary data analysis for this study was accomplished through the use of an ART Filter process. This "CAFFilter" was based on NOνA Offline software (NOνASoft)'s "CAFMaker" data-reduction framework, but instead of producing ROOT files histogramming the outputs of various analysis modules, it uses those outputs to select events based on a given filter expression. This allows for the creation of files that contain only events that pass the defined criteria, but all of the event information is present so tools such as the Event Display may still be used (Users of the Common Analysis Framework (CAF) framework have to do significantly more work to look at actual event data). The module accepts expressions for four different

levels of cuts: "Cosmic Rejection" (CosRej), "Containment", "Quality", and "Selection" (Particle Identification (PID)). NOνA's ν_μ and ν_e groups have each defined their cuts in terms of analysis module outputs, and these cuts can be expressed in terms of the aforementioned levels.

The analysis module was run over both cosmic data files with events near beam spills removed by another filter module ($\sim$ 18M events, 9920 seconds of live-time) and Monte Carlo simulations of both ν_μ and ν_e interactions ($\sim$ 1.8M events each). The Monte Carlo files provided efficiency and purity metrics for both filter sets, where efficiency refers to the percentage of true events that pass the cuts, and purity refers to the ratio between the amount of neutrino events of the targeted flavor that pass to the total number of events that pass from both the target neutrino flavor and the other simulated neutrino interactions. Both of these metrics should be as high as possible while still maintaining good cosmic background rejection.

6.3 Results

Initial results were hard to interpret, as the first runs of the filter produced outputs that were far too high in background events with far too low efficiency metrics from the Monte Carlo datasets. After much tuning, the background rates were on a par with NOνA's calculations, but the efficiency metrics were still much lower than the NOνA prediction. Further analysis with refinements to the cuts developed by the ν_e and ν_μ analysis groups failed to increase the efficiency metrics, but did reduce the background to the point where the signal to noise ratio (SNR) was acceptable (Table 6.3).

This result was then analyzed using NOνA's event rate prediction for 750 kW Neutrinos from the Main Injector (NuMI) operation ($\sim$ 1 neutrino event (ν_eCC + ν_μCC + NC) per day). Using the best-fit oscillation parameters (see Section 2.4), the relative ν_e/ν_μ content of the NuMI beam was estimated and combined with the efficiency parameters to predict the CC daily event rate. Similarly, the background

Table 6.2: Summary Results of Background Analysis. Cosmic data is 18M events, or 9900 seconds of live-time. Monte Carlo are each 1.8M events. Purity metrics for each neutrino flavor Monte Carlo Simulation (MC) are shown in the opposing flavor column, and the efficiency metric for a flavor is shown in that flavor's result column.

Analysis	**ν_e Result**	**ν_μ Result**
Cosmic Data	29 Events Passed	140 Events Passed
ν_e Monte Carlo	Efficiency: 13.14%	Purity: 98.62%
ν_μ Monte Carlo	Purity: 98.94%	Efficiency: 6.70%

live-time was scaled using the NuMI daily live-time to make a prediction for background events observed per day based on the number of events passing the selection filters. These two predictions were used to estimate the SNR (Table 6.3).

Table 6.3: Background Analysis Results: Daily Event Prediction

Neutrino Flavor	**Background**	**Predicted Signal**	**SNR**
ν_e	0.00937	0.05737	5.7328
ν_μ	0.04605	0.10661	2.3152

The 169 events from the random cosmic trigger that passed the selection criteria were examined using the NOνA Event Display and the quantities related to the selection cuts were evaluated as well. Of special interest were the ν_e events that passed, as they have more bearing on the "First Analysis" result from NOνA.

Out of the events that passed the selection algorithms, most were clearly not ν_e events due to their location in the detector (most commonly observed were events near the rear of the detector Figures 6.1 and 6.2), structure (events that do not appear to be an electromagnetic shower, Figure 6.3), or failures of reconstruction (due to a gap in a muon track, the Slicer created two separate slices where it only should have made one, the tail of the track happened to look like a ν_e event, Figure 6.4). The simplest answer which would eliminate all of the observed background events is to increase the veto area at the edges of the detector. If this option is undesirable, better shower reconstruction in order to make a clear determination of directionality (Figures 6.5

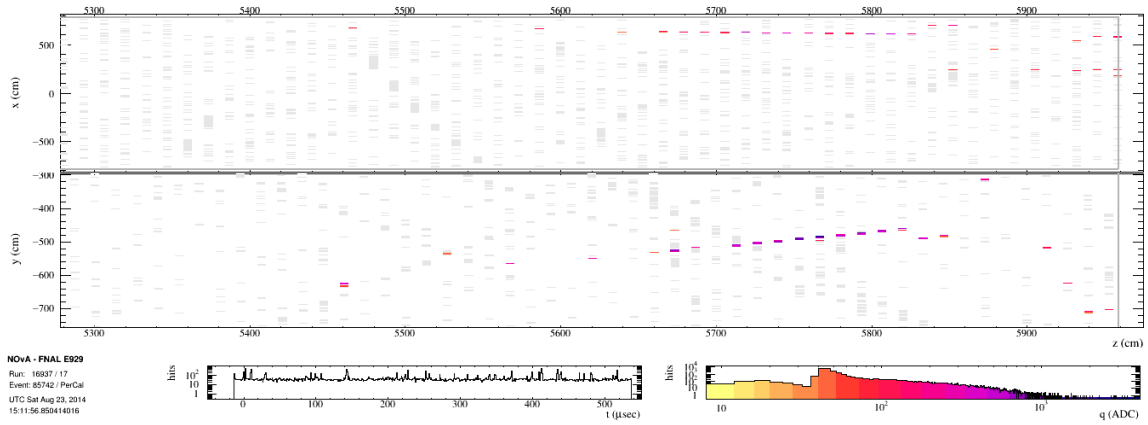

Figure 6.1: Event Display, Run 16937, Event 85742: This event looks like a ν_e event, and it passed ν_e selection. The hits, however, are all on the very edge of the detector and extend to the end of the detector, so fiducial cuts would have removed this event.

and 6.6) and shower "size" with respect to reconstructed energy may be capable of eliminating more background events.

Muon neutrino background had similar issues, with an increased fiducial cut and Slicer gap optimization (Figure 6.7) potentially reducing the background events observed. Also, as in the ν_e selection, event directionality did not appear to be taken into account (Figures 6.8 and 6.9). Finally, the muon event filters appear to accept some events with too few hits in one view or the other, which can cause the PID algorithms to see verticies in noise hit data. It is possible that some of the code created to correct for gaps in the Near Detector On Surface (NDOS) would also assist with the mis-Sliced events.

6.4 Other Backgrounds

This study was concerned with the cosmic-induced "accidental" background of the experiment, but of potentially more concern are beam-induced backgrounds. Beam-induced backgrounds occur in-time with the beam, nullifying NOνA's most powerful background discriminator. The largest contributor to background is ν_e contamination in the NuMI beam, and is the entire reason for the construction of the Near Detector

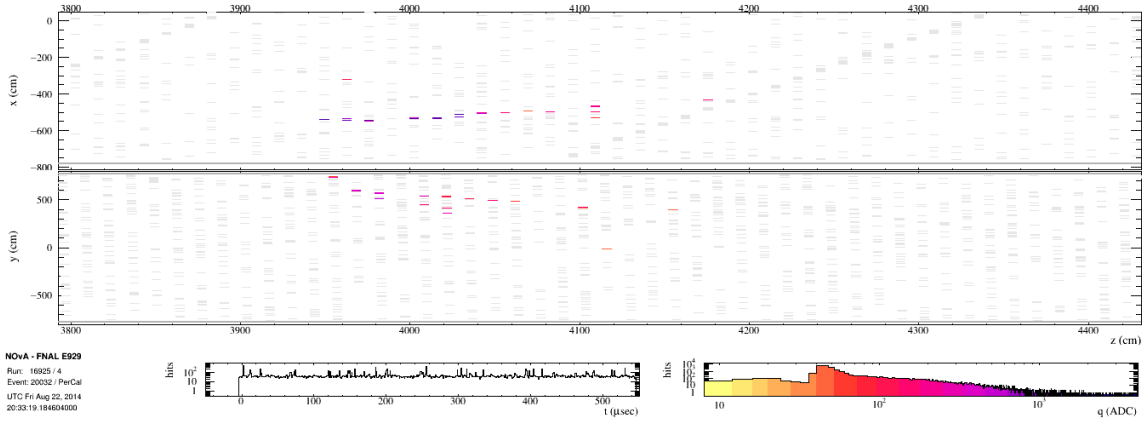

Figure 6.2: Event Display, Run 16925, Event 20032: This event appears to be an electromagnetic shower, but since the vertex of the event is very close to the top of the detector, it should have been cut through the fiducial cuts.

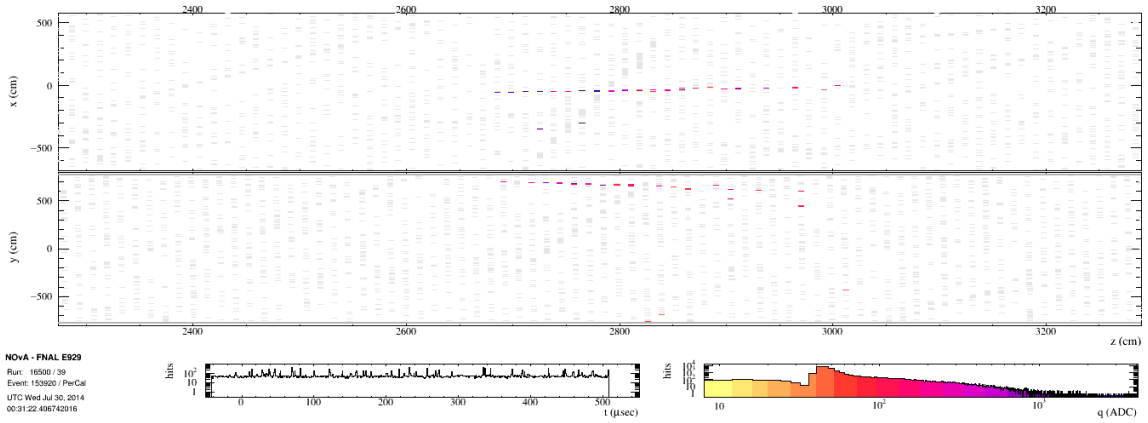

Figure 6.3: Event Display, Run 16500, Event 153920: This event does not appear to have much of a shower component, and its location suggests that the ν_e fiducial cuts are not large enough.

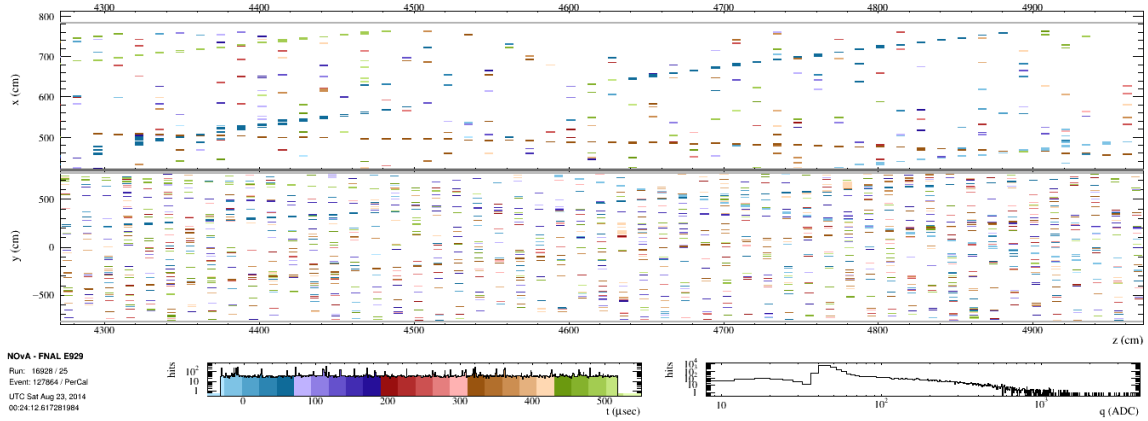

Figure 6.4: Event Display, Run 16928, Event 127864: The ν_e selection-identified event is on the left-hand side in blue. The Slicer module made an error due to the gap, and it should have also associated the muon to the right with it. Events in this plot are colored by time, so both events are the same color to distinguish them from other muon tracks in this region of the detector.

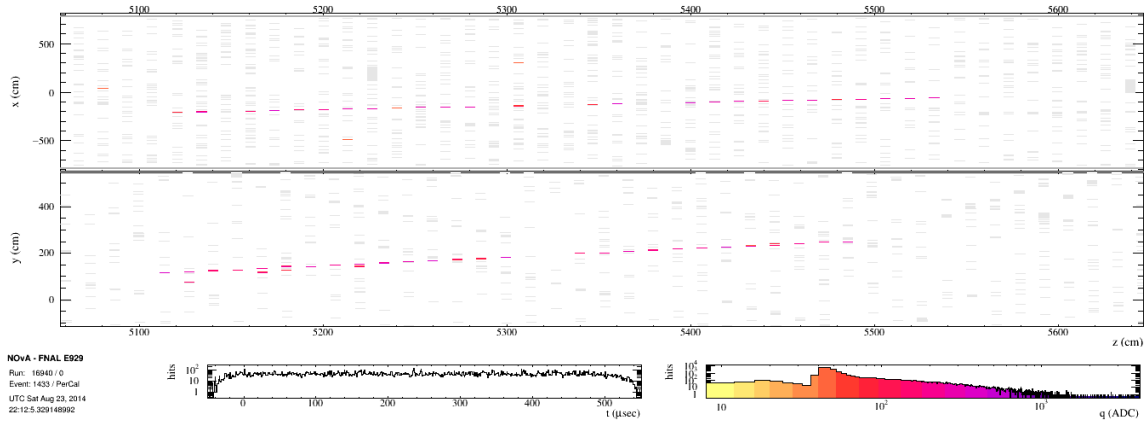

Figure 6.5: Event Display, Run 16940, Event 1433: This event passed ν_e selection criteria, but direct observation shows that the shower is forming in the wrong direction (right-to-left instead of left-to-right)

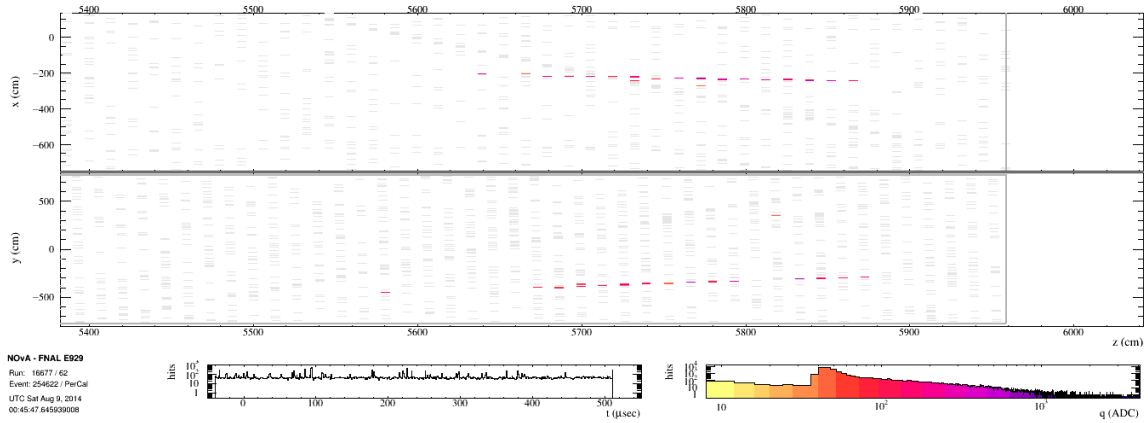

Figure 6.6: Event Display, Run 16677, Event 254622: This event passed ν_e selection, but the shower is clearly developing in the wrong direction (right-to-left instead of left-to-right).

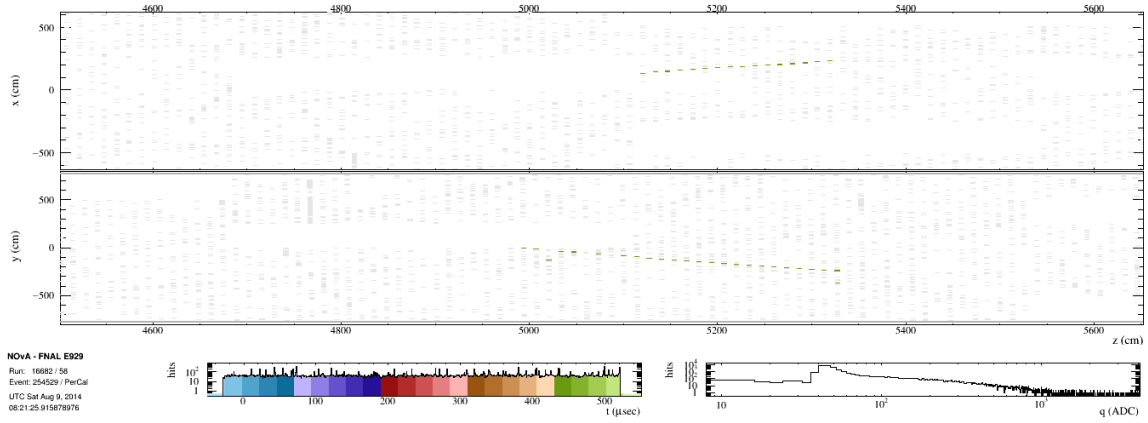

Figure 6.7: Event Display, Run 16682, Event 254529: This event suffered from DCM issues which caused gaps which tricked the ν_μ selection algorithms.

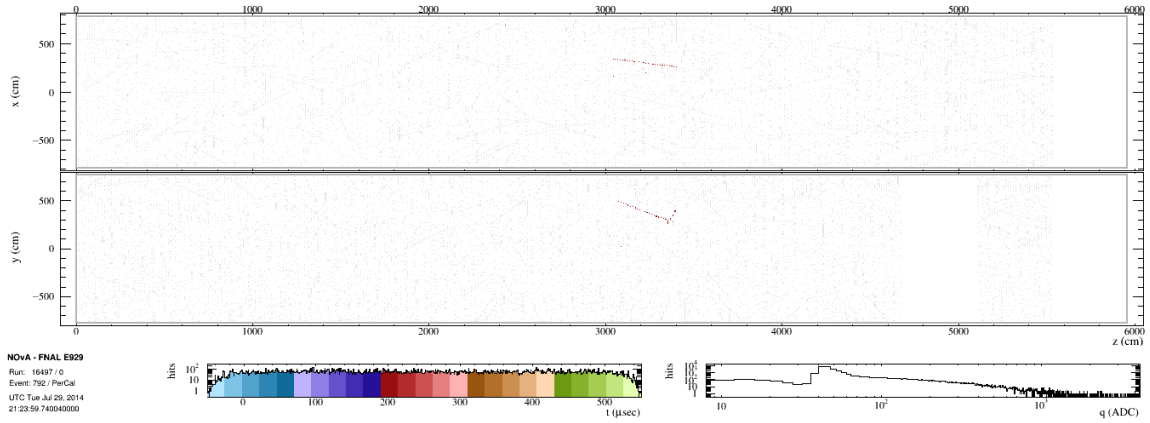

Figure 6.8: Event Display, Run 16497, Event 792: This event looks very much like a ν_μ event, and it passed ν_μ selection, however, it is clearly not from the beam direction (left-hand side of the detector).

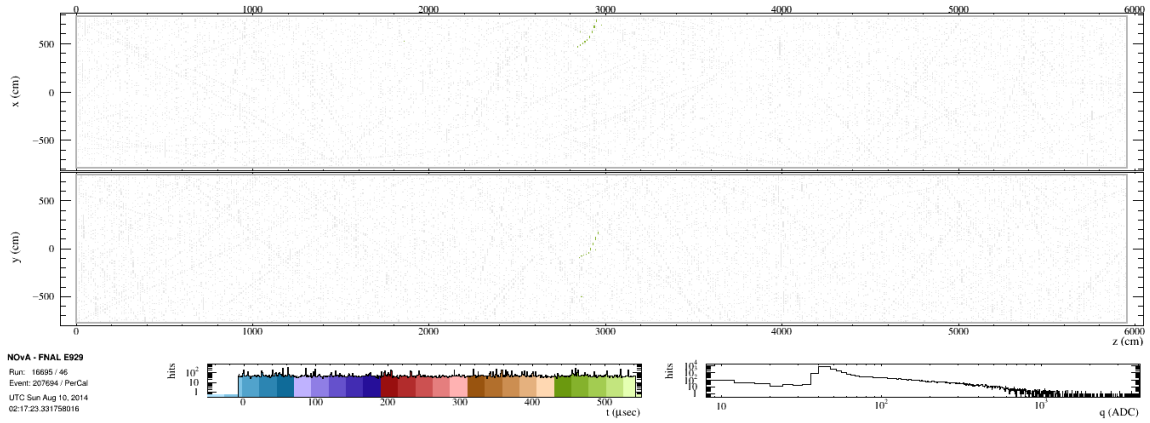

Figure 6.9: Event Display, Run 16695, Event 207694: This event passed ν_μ selection, and while it has the characteristic vertex, there does not appear to be a distinct muon track leaving the vertex. Also, the directionality of the event means that it cannot possibly be a beam event.

(ND); the main purpose of the ND is to characterize the beam before it has traveled (and oscillated) to Ash River. This includes both spectral information and flavor-content information. Less considered, however, is the possibility of tau neutrino (ν_τ) contamination in the beam, which can lead to events that look exactly like a ν_μ or ν_e event. The main difference between a ν_τ event and the other flavors is a higher range of possible transverse momenta of the daughter particles, as a ν_τ decay is a multi-body problem for the decays that produce an electron or muon in the final state (a τdecays to an electron or muon, a same-flavored anti-neutrino, and a ν_τ, with roughly 20 percent probability for both electrons and muons). Andrew Lopez of the University of Tennessee (UT) group has performed initial simulations and found that ν_τ contamination in the FD will be on the order of 1% of the ν_e event rate (Figure 6.10).

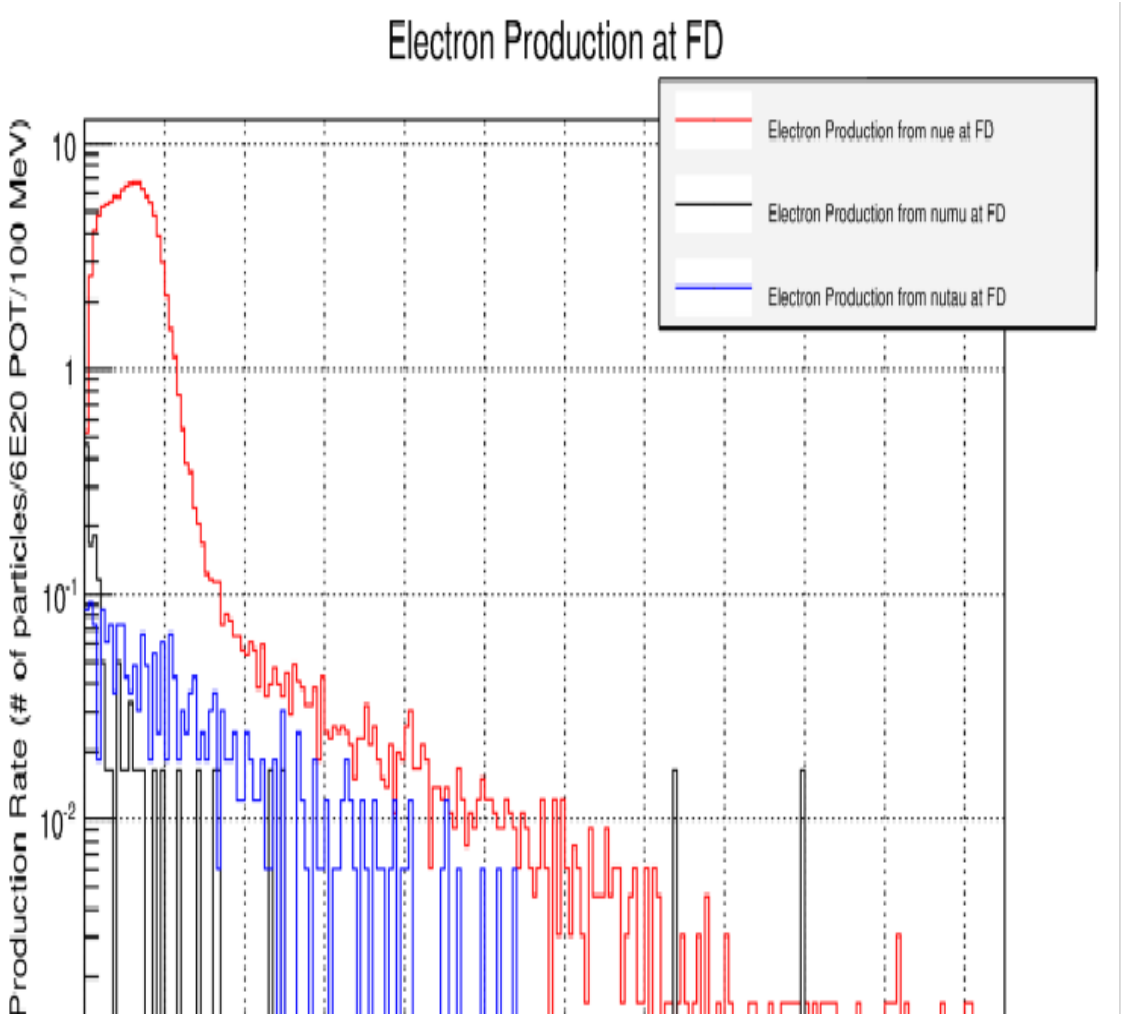

Figure 6.10: Resulting ν_τ Contamination in the NOνA FD. Figure from Andrew Lopez.

Chapter 7

Sterile Neutrinos in the NOνA Near Detector (Study)

7.1 Introduction and Sterile Neutrino Hypothesis

Reactor neutrino experiments have measured smaller neutrino rates in their detectors than models predict, and this has led to the "reactor neutrino anomaly", a roughly 5% effect ([22]). One possible source of this effect is the existence of a fourth neutrino mass state with a squared mass difference of approximately 1 eV^2. Because of this large mass splitting, the initial flux from any neutrino source would very quickly reach a stable equilibrium, with some fraction of the expected flux "disappearing" into the fourth, non-interacting mass state (the so-called "sterile" state, Figure 7.1). For this treatment, I have assumed a simple, "two neutrino" model, with one neutrino representing all of the "flavored" neutrinos, and the other representing the non-interacting, sterile neutrinos.

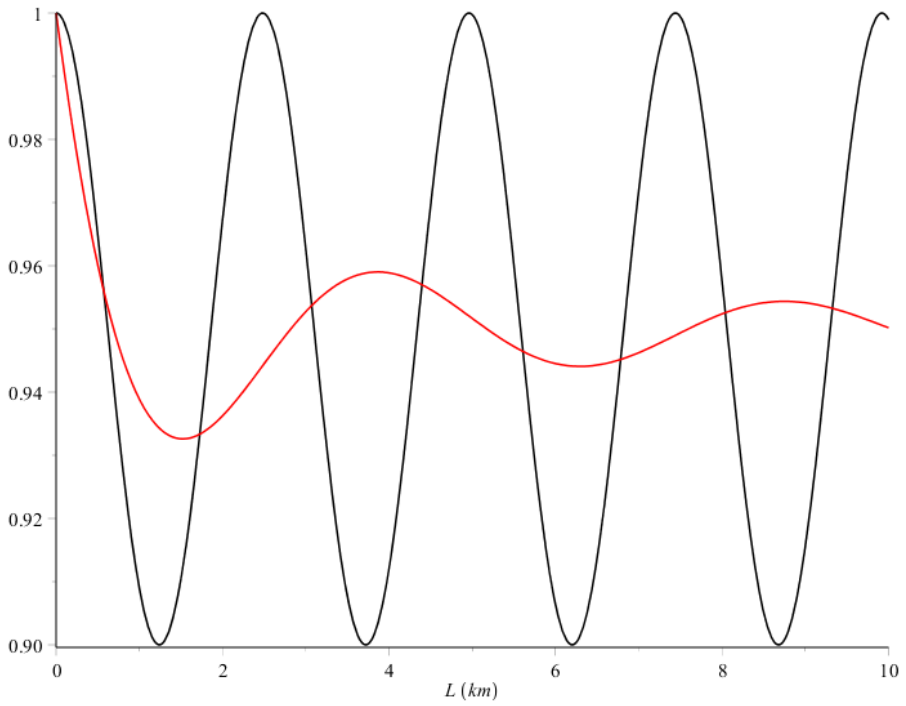

Figure 7.1: Example of the effect of the presence of sterile neutrinos. In black is the survival probability for 1 GeV neutrinos from 0-10 km. The red line shows the ensemble effect of sterile neutrino oscillations on a flat spectrum of neutrinos between 0 and 2 GeV. Observers at 10 km would therefore only observe 95% of the expected neutrino flux (the red line). Oscillation parameters used for this plot were $\Delta m^2 = 1\ eV^2$ and $sin^2(2\theta) = 0.1$.

7.2 NOνA Sensitivity: Disappearance Channel

The standard method for a neutrino experiment is to build two detectors at different baselines from the source and observe the difference in neutrino rate between them. The near detector in such a two-detector experiment serves to provide information about the absolute neutrino flux coming from the experiment's neutrino source. For a potential extension to NuMI Off-Axis ν_e Appearance (NOνA) looking at sterile neutrinos, the two detectors would be the existing Near Detector (ND) and Near Detector On Surface (NDOS). The operation of this two-detector experiment would be a little different than the standard, as both detectors are exposed to the effect under scrutiny. The ND, as it is exposed to higher total neutrino flux, would predict the number and spectrum of neutrinos observed at NDOS based on no sterile oscillations, and the result would be if NDOS observed a statistically significant excess or deficit of events based on the ND's prediction.

7.3 NOνA Sensitivity: Spectral Distortion Channel

An alternative measurement, possible because the Neutrinos from the Main Injector (NuMI) beam has both a very well-measured spectrum and well-defined off-axis characteristics, is to look for the spectrum distortion effect of sterile neutrino oscillations. Because oscillation probability is proportional to length divided by energy (L/E), it is theoretically possible to observe a relative deficit in low-energy neutrinos versus higher energy neutrinos. This can be run either as a one-detector experiment or as a two-detector one. In the one-detector case, the observed spectrum is normalized and compared with the expected spectrum from the beam models (Figures 7.2 and 7.3). In the more advanced two-detector experiment, the far detector spectrum is predicted based on the observed spectrum in the near detector, and differences analyzed.

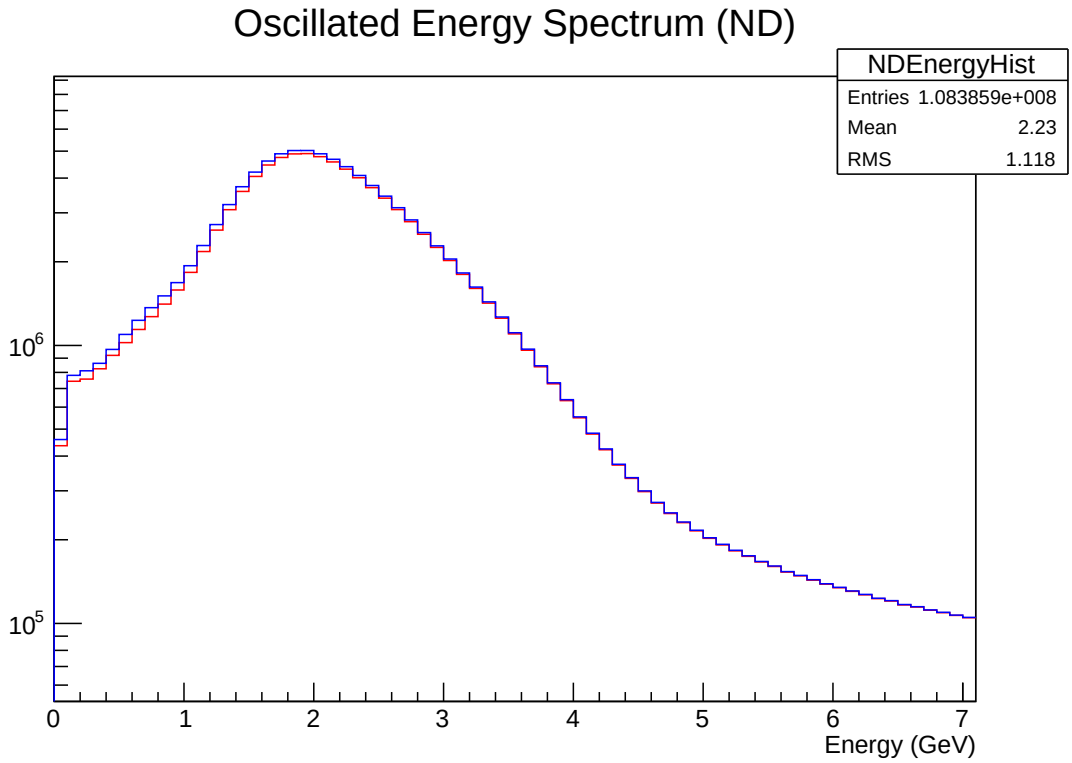

Figure 7.2: Near detector spectrum prediction with sterile neutrino oscillation. The predicted spectrum is in blue and an oscillated spectrum is in red. Oscillation parameters used for this plot were $\Delta m^2 = 1\ eV^2$ and $sin^2(2\theta) = 0.1$. At these parameter values, the NOνA counting experiment has close to 2-σresolution, after taking into account detector energy resolution.

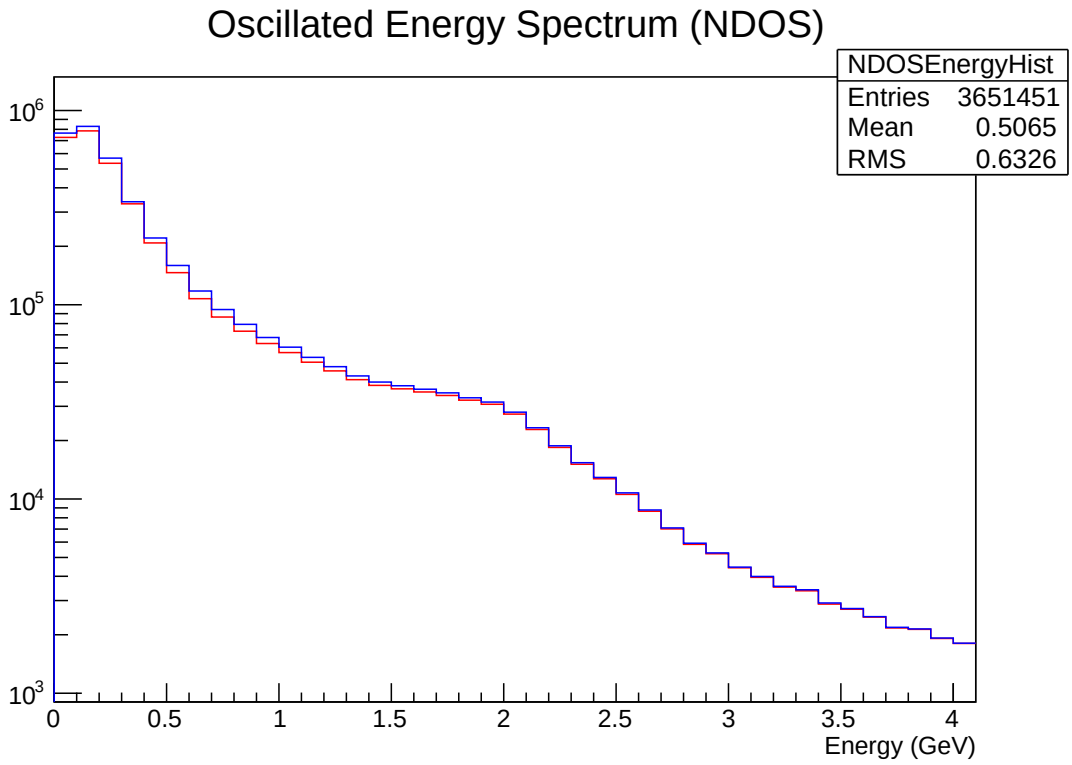

Figure 7.3: NDOS Spectrum Prediction with Sterile Neutrino Oscillation. The predicted spectrum is in blue and an oscillated spectrum is in red. Oscillation parameters used for this plot were $\Delta m^2 = 1\ eV^2$ and $sin^2(2\theta) = 0.1$.

7.4 Combined Measurements

Since the two methods are complementary, it is possible to combine the results with a simple probability addition ($P = P1 + P2 - P1 * P2$).

I have written a Monte Carlo grid simulation to evaluate NOνA's sensitivity to sterile neutrinos. For a given point in Δm^2 versus ϑ_S space, the simulation runs a year's worth of simulated beam neutrino propagation length and energy events picked randomly from the official NOνA flux files through both detectors. Each event has its oscillation probability calculated, and the simulation makes a weighted Monte Carlo decision based on that information. It then records the results of a disappearance experiment (a Poisson probability is calculated based on the number of events predicted versus the number of events which survive the oscillation simulation) and a spectral distortion experiment (the spectra from the two detectors are compared using a K-S test [14]) based on the simulated events which survive the oscillation simulation in each detector. The simulation code finally combines the two using the probability addition formula above and creates histograms of significance versus Δm^2 versus ϑ_S (Figure 7.4). The simulation "smears" the energy of the event by sampling a normal distribution in order to simulate the energy resolution of the detectors. "Truth" values are also kept with the energy smearing removed.

7.5 NOνA versus Reactor Experiments

In order to observe a sterile neutrino signal, a reactor-based experiment would have to get within 1 m of the reactor core with a near detector, leading to many obvious design challenges. NOνA's ND is at a similar L/E value to a 1 m reactor experiment (Figure 7.5). Knowing the flux from the NuMI beam precisely enough for this sort of measurement is extremely difficult, however, but NOνA has two detectors exposed to the same beam at short baseline. The two detectors are at radically different angles with respect to the beam's initial direction, but because characterizing the beam is a

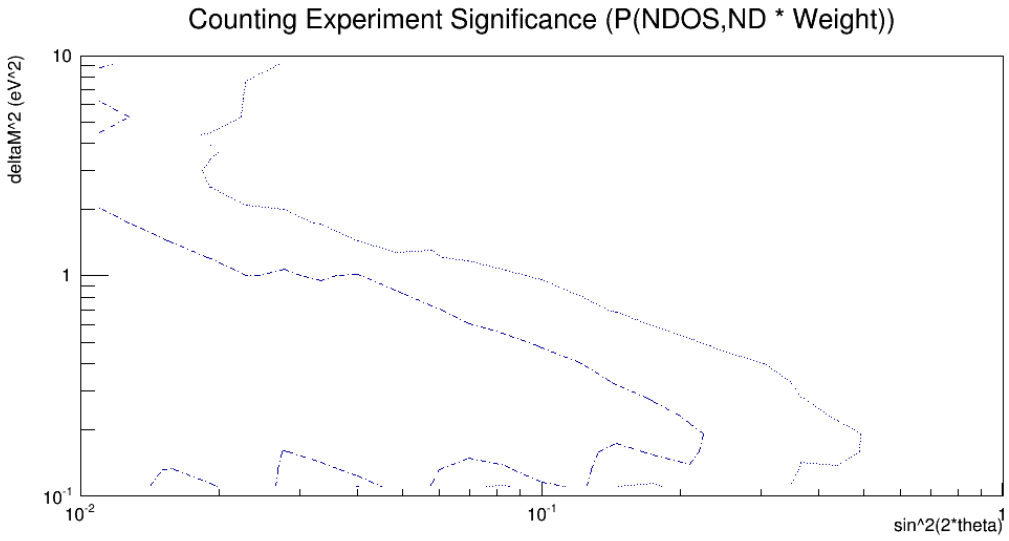

Figure 7.4: Result of the grid simulation for NOνA sterile neutrino sensitivity. Contours shown are for 1σ and 2σ.

simple kinematics problem, the flux at one detector can be accurately predicted by observing the flux at the other. The only issue, then, is that the two NOνA detectors are at very similar positions in L/E space, limiting the sensitivity to oscillations.

Also, NOνA is exposed to a muon neutrino (ν_μ) beam, as opposed to the electron neutrino (ν_e) flux that a reactor experiment experiences. The reactor anomaly has only been observed with ν_e sources, mainly because of the difficulties in obtaining reliable flux predictions from accelerator sources.

7.6 NOνA versus Accelerator Experiments

Several electron-neutrino accelerator experiments have been proposed, namely IsoDAR/Daedalus. NOνA is in the unique position of having access to a muon neutrino beam, two detectors at low L/E, and good optimization for separation of neutrino events and background.

Fermilab is executing a Short Baseline Neutrino (SBN) plan; three liquid argon detectors will be placed in the Booster Neutrino Beam (BNB): MiniBooNE, μBooNE, and the ICARUS detector from Gran Sasso. This three detector experiment will not

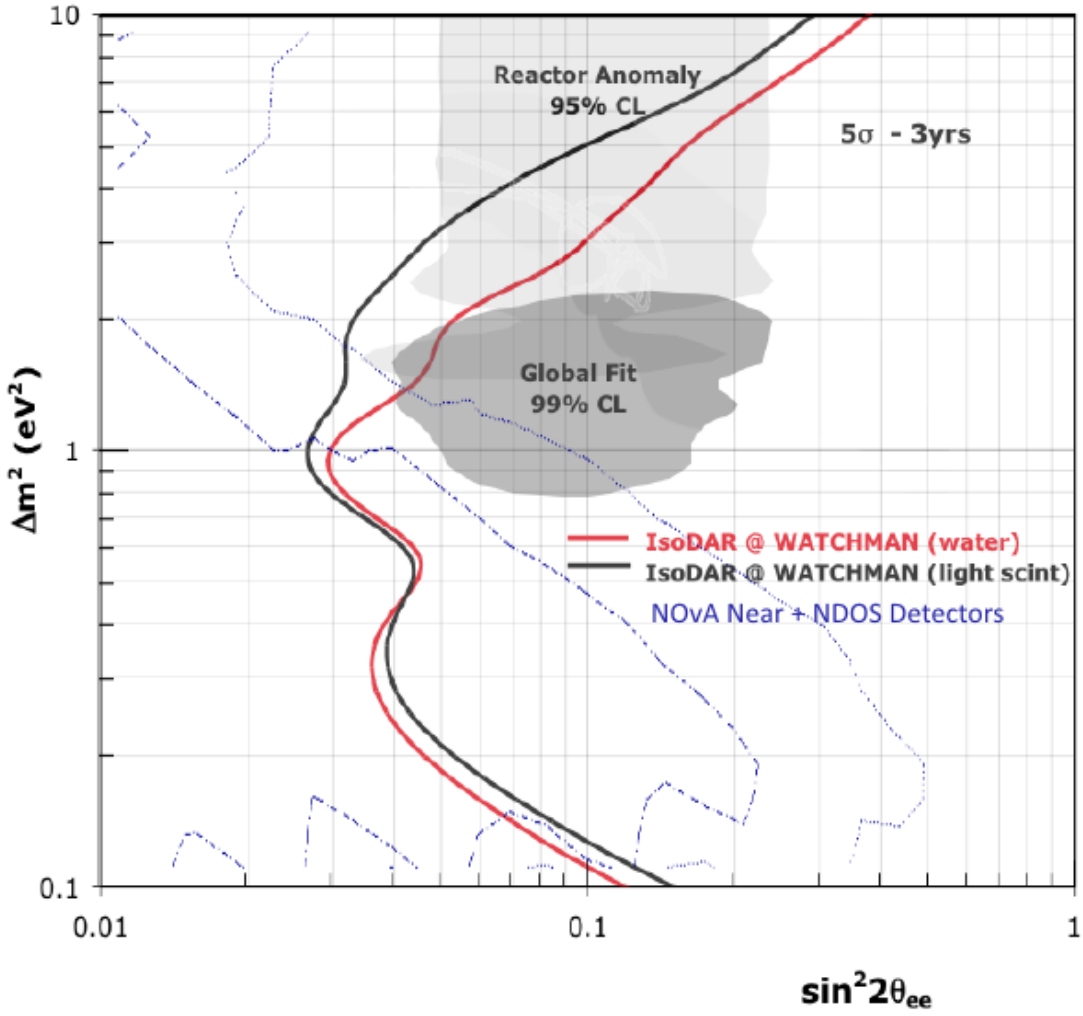

Figure 7.5: Result of the grid simulation for NOνA Sterile Neutrino sensitivity, plotted on the same scale as for the Watchman experiment's projected sensitivity. NOνA contours shown are for 1σand 2σ.

only constrain sterile neutrino parameters, but also provide excellent sensitivity on the observed "LSND effect", an excess of $\bar{\nu}_e$ appearance events in a $\bar{\nu}_\mu$ beam [10]. MiniBooNE and μBooNE are already in place, μBooNE has begun regular operations, with physics data-taking beginning in Fall 2015.

7.7 Conclusion

NOνA is capable of making a competitive measurement of sterile neutrino oscillation. However, the NDOS detector will soon be decommissioned, which will remove this possibility. Despite my efforts to maintain the NDOS Data Acquisition (DAQ) systems, there are no users of the detector and it has been allowed to sit in a power-off mode. In addition, if the NOνA Collaboration wanted to truly attempt this measurement, the NDOS detector would have to have its existing electronics refurbished and be fully instrumented, as well as re-filled with Liquid Scintillator (LS) and the leaks which have caused parts of the detector to drain located and repaired. With the SBN program at Fermi National Accelerator Laboratory (Fermilab) coming on-line in the near future, there is little interest in the NOνA collaboration in pushing NOνA into short-baseline science, despite the fact that this would be a relatively fast, low-cost result that could place initial limits on the phase space for future ν_μ beam experiments.

Chapter 8

Summary and Conclusion

8.1 DAQ Service Work

My work for the NOνA DAQ software (NOνADAQ) has the immediate effect of enabling all of the physics results that NuMI Off-Axis ν_e Appearance (NOνA) produces. Of special importance is the setup of the Near Detector (ND) Data Acquisition (DAQ), a task I performed essentially single-handedly. My work has also allowed the Data-Driven Triggers (DDT) group to broaden their horizons to include many more real-time analyses as I have both improved the performance of systems that are key to their software and installed, tested, and integrated the computing resources necessary to allow each DDT analysis enough decision time to perform the necessary reconstruction. As a direct result of my work with the NOνA DAQ systems, I have been offered employment at Fermi National Accelerator Laboratory (Fermilab), working on DAQ software for Fermilab's future experiments.

8.2 Scintillator Absolute Calibration

The Compton spectrometer experiment has measured the integrated nonlinearity effects in the NOνA Liquid Scintillator (LS). Along with the results of the UV monochromator experiment, the University of Tennessee (UT) group is prepared to

make a significant contribution to the NOνA calibration effort and ensure that NOνA is capable of accurately reconstructing the energy of the electromagnetic showers created by the electron neutrinos (ν_es) that are the primary subject of the experiment. Our result is independent of the accuracy of the NOνA Monte Carlo simulations and its integration into the NOνA analysis software should reduce an important systematic uncertainty.

8.3 Background Evaluation

NOνA's position on the surface makes it of vital importance to understand the background present in the Far Detector (FD). Not only do we have to understand any potential background signals that make their way into our readout, we have to show the HEP community at large that we have studied these signals and can clearly distinguish data from background. The goal of this study was to find and characterize the background signal of the NOνA FD, so that NOνA can indeed be confident in their ultimate results. I have found that NOνA's backgrounds are somewhat high relative to the selected signal efficiency, but there are definitely additional cuts which should reduce the background without affecting the signal.

8.4 Conclusion

My experience with NOνA has helped me to become an expert on all aspects of DAQ systems, my interest in NOνA backgrounds has led me to create ties with the astrophysics and dark-matter communities, and my sterile neutrino sensitivity study has given me insight into the plans of experiments such as μBooNE and the Short Baseline Neutrino (SBN) at Fermilab. NOνA will shortly release its first analysis results, and is continuing on its six-year neutrino program.

Bibliography

[1] S Abe et al. (KamLAND Collaboration). "Precision measurement of neutrino oscillation parameters with KamLAND." In: *Physical review letters* 100.22 (June 2008), p. 221803. ISSN: 0031-9007. DOI: 10.1103/PhysRevLett.100.221803. URL: http://link.aps.org/doi/10.1103/PhysRevLett.100.221803.

[2] B Aharmim et al. (SNO Collaboration). "Electron energy spectra, fluxes, and day-night asymmetries of B-8 solar neutrinos from measurements with NaCl dissolved in the heavy-water detector at the Sudbury Neutrino Observatory". In: *Phys.Rev.* C72.October (Feb. 2005), p. 55502. DOI: 10.1103/PhysRevC.72.055502. arXiv: nucl-ex/0502021 [nucl-ex]. URL: http://arxiv.org/abs/nucl-ex/0502021%20http://arxiv.org/abs/nuclex/0502021.

[3] QR Ahmad et al. (SNO Collaboration). "Measurement of the rate of $\nu_e + d \rightarrow p + p + e^-$ interactions produced by ^{8}B solar neutrinos at the Sudbury Neutrino Observatory". In: *Phys. Rev. Lett* 87.7 (July 2001), p. 071301. ISSN: 0031-9007. DOI: 10.1103/PhysRevLett.87.071301. URL: http://link.aps.org/doi/10.1103/PhysRevLett.87.071301%20http://scholar.google.com/scholar?hl=en%5C&btnG=Search%5C&q=intitle:Measurement+of+the+Rate+of+$%5Cnu$e+++d+?+p+++p+++e-+Interactions+Produced+by+B8+Solar+Neutrinos+at+the+Sudbury+Neutrino+Observatory%5C#0.

[4] M. H Ahn et al. (K2K Collaboration). "Measurement of neutrino oscillation by the K2K experiment". In: *Phys. Rev. D* 74.7 (Oct. 2006), p. 72003. ISSN: 1550-7998. DOI: 10.1103/PhysRevD.74.072003. URL: http://link.aps.org/doi/10.1103/PhysRevD.74.072003.

[5] Sergey Alekhin et al. "A facility to Search for Hidden Particles at the CERN SPS: the SHiP physics case". In: (2015). arXiv: 1504.04855 [hep-ph].

[6] FP An et al. (Daya Bay Collaboration). "Improved measurement of electron antineutrino disappearance at Daya Bay". In: *Chinese ...* 37.1 (2013), p. 11001.

URL: http://stacks.iop.org/1674-1137/37/i%20=%201/a%20011001%20http://iopscience.iop.org/1674-1137/37/1/011001.

[7] E C Anderson et al. "The Reines-Cowan Experiments: Detecting the Poltergeist". In: *Los Alamos Science* 25.25 (1997), pp. 4–27. URL: http://cat.inist.fr/?aModele=afficheN%5C&cpsidt=10450100.

[8] M Apollonio, A Baldini, and C Bemporad (CHOOZ Collaboration). "Search for neutrino oscillations on a long base-line at the CHOOZ nuclear power station". In: *The European Physical ...* 27 (Apr. 2003), pp. 331–374. DOI: 10.1140/epjc/s2002-01127-9. URL: http://link.springer.com/article/10.1140/epjc/s2002-01127-9.

[9] F. Ardellier et al. "Double Chooz, A Search for the Neutrino Mixing Angle θ13". Double Chooz Collaboration Description of planned reactor neutrino experiment. 162 pages, 106 figures, 113 authors from 24 institutions Revision fixes typos in simulation, electronics and photomultiplier chapters. 2006. URL: http://hal.in2p3.fr/in2p3-00087231.

[10] C. Athanassopoulos et al. (LSND). "Evidence for neutrino oscillations from muon decay at rest". In: *Phys. Rev.* C54 (1996), pp. 2685–2708. DOI: 10.1103/PhysRevC.54.2685. arXiv: nucl-ex/9605001 [nucl-ex].

[11] LM Brown. "The idea of the neutrino". In: *Physics Today* 31 (1978), pp. 23–28. URL: http://ddd.uab.cat/pub/ppascual/ppascualapu/ppascualapu%5C_41%5C_001@benasque.pdf.

[12] BT Cleveland and T Daily. "Measurement of the solar electron neutrino flux with the Homestake chlorine detector". In: *The Astrophysical ...* 20.1982 (1998). URL: http://iopscience.iop.org/0004-637X/496/1/505.

[13] Raymond Davis. "A review of the homestake solar neutrino experiment". In: *Progress in Particle and Nuclear Physics* 32 (1994), pp. 13–32. ISSN: 0146-6410.

DOI: http://dx.doi.org/10.1016/0146-6410(94)90004-3. URL: http://www.sciencedirect.com/science/article/pii/0146641094900043.

[14] W.T. Eadie. *Statistical methods in experimental physics*. North-Holland Pub. Co., 1971. URL: https://books.google.com/books?id=QKDvAAAAMAAJ.

[15] Justin Evans (MINOS). "The MINOS experiment: results and prospects". In: *Adv.High Energy Phys.* 2013 (2013), p. 182537. DOI: 10.1155/2013/182537. arXiv: 1307.0721 [hep-ex].

[16] J. Formaggio and G. Zeller. "From eV to EeV: Neutrino cross sections across energy scales". In: *Reviews of Modern Physics* 84.3 (Sept. 2012), pp. 1307–1341. ISSN: 0034-6861. DOI: 10.1103/RevModPhys.84.1307. URL: http://link.aps.org/doi/10.1103/RevModPhys.84.1307.

[17] Y. Fukuda, T. Hayakawa, and E. Ichihara (Super-Kamiokande Collaboration). "Evidence for oscillation of atmospheric neutrinos". In: *Physical Review Letters* 81.8 (1998), pp. 1562–1567. DOI: 10.1103/PhysRevLett.81.1562. URL: http://link.aps.org/doi/10.1103/PhysRevLett.81.1562%20http://prl.aps.org/abstract/PRL/v81/i8/p1562%5C_1.

[18] JL Hewett, H Weerts, and R Brock. "Fundamental physics at the intensity frontier". In: *arXiv preprint arXiv: ...* December (2012). arXiv: arXiv:1205.2671v1. URL: http://arxiv.org/abs/1205.2671.

[19] Glenn F Knoll. *Radiation detection and measurement*. 3rd ed. 2010. URL: http://books.google.com/books?hl=en%5C&lr=%5C&id=4vTJ7UDel5IC%5C&oi=fnd%5C&pg=PA1%5C&dq=Radiation+Detection+and+Measurement%5C&ots=VvyOzQBSdw%5C&sig=yRziOuoIwCsw8VIlnN9wFDmK238.

[20] L. D. Landau, L. P. Pitaevskii, and E. M. Lifshitz. *Electrodynamics of Continuous Media, Second Edition: Volume 8 (Course of Theoretical Physics)*. 2nd ed. Butterworth-Heinemann, Jan. 15, 1984. ISBN: 0750626348. URL: http:

//www.amazon.com/exec/obidos/redirect?tag=citeulike07-20%5C&path=ASIN/0750626348.

[21] Guillaume Mention, Thierry Lasserre, and Dario Motta. "A Unified analysis of the reactor neutrino program towards the measurement of the θ_{13} mixing angle". In: *J.Phys.Conf.Ser.* 110 (2008), p. 82013. DOI: 10.1088/1742-6596/110/8/082013. arXiv: 0704.0498 [hep-ex].

[22] G. Mention et al. "The Reactor Antineutrino Anomaly". In: *Phys.Rev.* D83 (2011), p. 073006. DOI: 10.1103/PhysRevD.83.073006. arXiv: 1101.2755 [hep-ex].

[23] D G Michael et al. (MINOS Collaboration). "Observation of Muon Neutrino Disappearance with the MINOS Detectors in the NuMI Neutrino Beam". In: *Phys. Rev. Lett.* 97.19 (Nov. 2006), p. 191801. ISSN: 0031-9007. DOI: 10.1103/PhysRevLett.97.191801. URL: http://link.aps.org/doi/10.1103/PhysRevLett.97.191801.

[24] K. Nakamura et al. "Review of Particle Physics". In: *Journal of Physics G: Nuclear and Particle Physics* 37 (2010), p. 075021. ISSN: 0954-3899. DOI: 10.1088/0954-3899/37/7A/075021. URL: http://iopscience.iop.org/0954-3899/37/7A/075021/fulltext/.

[25] NOνA Collaboration. *NOνA Plots and Figures*. URL: http://www-nova.fnal.gov/plots%5C_and%5C_figures/plot%5C_and%5C_figures.html.

[26] NOνA Collaboration. *Technical Design Report*.

[27] SJ Parke. "Determining the neutrino mass hierarchy". In: (2006), pp. 115–125. URL: http://lss.fnal.gov/archive/2006/conf/fermilab-conf-06-248-t.pdf%20http://lss.fnal.gov/cgi-bin/find%5C_paper.pl?conf-06-248.pdf.

[28] OV Perevozchikov. "Search for electron antineutrinos from the sun with KamLAND detector". In: *Doctoral Dissertations* (2009). URL: http://trace.tennessee.edu/cgi/viewcontent.cgi?article=1121%5C&context=utk%5C_graddiss.

[29] V. I. Tretyak. "Semi-empirical calculation of quenching factors for ions in scintillators". In: *Astropart. Phys.* 33 (2010), pp. 40–53. DOI: 10.1016/j.astropartphys.2009.11.002. arXiv: 0911.3041 [nucl-ex].

[30] John D Valentine and Brian D Rooney. "Design of a Compton spectrometer experiment for studying scintillator non-linearity and intrinsic energy resolution". In: *Nuclear Instruments and Methods in Physics Research Section A: Accelerators, Spectrometers, Detectors and Associated Equipment* 353.1-3 (1994), pp. 37–40. ISSN: 0168-9002. DOI: http://dx.doi.org/10.1016/0168-9002(94)91597-0. URL: http://www.sciencedirect.com/science/article/pii/0168900294915970.

[31] Joachim Wolf. "The {KATRIN} neutrino mass experiment". In: *Nuclear Instruments and Methods in Physics Research Section A: Accelerators, Spectrometers, Detectors and Associated Equipment* 623.1 (2010). 1st International Conference on Technology and Instrumentation in Particle Physics, pp. 442–444. ISSN: 0168-9002. DOI: http://dx.doi.org/10.1016/j.nima.2010.03.030. URL: http://www.sciencedirect.com/science/article/pii/S0168900210005942.

Vita

Eric Flumerfelt was born in Altoona, PA in December, 1987. After graduating high school in 2005, he attended Juniata College, where he earned a Bachelor of Science in Physics with Secondary Emphasis in Computer Programming and Peace and Conflict Studies in 2009. In August 2009, he was accepted to the Graduate School of the University of Tennessee, Knoxville, where he worked to earn a Doctor of Philosophy degree in Experimental High Energy Physics at the Department of Physics and Astronomy.